

Li-ion batteries monitoring for electrified vehicles applications

Original

Li-ion batteries monitoring for electrified vehicles applications / Vergori, Elena. - (2020 Jun 29), pp. 1-157.

Availability:

This version is available at: 11583/2839860 since: 2020-07-14T10:41:25Z

Publisher:

Politecnico di Torino

Published

DOI:

Terms of use:

Altro tipo di accesso

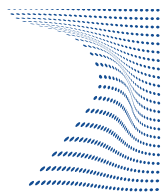
This article is made available under terms and conditions as specified in the corresponding bibliographic description in the repository

Publisher copyright

(Article begins on next page)



ScuDo
Scuola di Dottorato ~ Doctoral School
WHAT YOU ARE, TAKES YOU FAR



Doctoral Dissertation
Doctoral Program in Mechanical Engineering (XXXII Cycle)

Li-ion batteries monitoring for electrified vehicles applications

Elena Vergori

* * * * *

Supervisor
Prof. Aurelio Somà

Politecnico di Torino
May 16, 2020

Summary

The scenario of this work consists in the need for more information on the condition of Li-ion cells that are part of battery packs, used in electrified vehicles. A Li-ion cell consists in a complex system where electrochemical reactions happen, where heat is internally generated and where there are volumetric changes. With ageing a cell undergoes various damage mechanisms that influence the cell performance and safety, but that are very complex to be modelled. In order to have information on the cells state, quantities such as voltage, current and surface temperature of group of cells are monitored by the BMS. This information however results to be not enough to estimate with a good accuracy the cell state. Recent scientific trends show a growing interest in cells instrumentation, in order to acquire additional information in-situ and in-operando.

In this thesis, the main cells models used in electrified vehicles have been investigated together with the main state estimation algorithms. The attention has then been focused on cells instrumentation using innovative sensors for this application, such as distributed fibre optic sensors for thermo-mechanical monitoring of Li-ion cells. The selected sensors have been used for external and internal instrumentation of pouch format Li-ion cells. Thus, the cells manufacturing process has been studied and properly modified in order to allow the manufacturing of instrumented cells without compromising the cells and sensors functionality. These instrumented cells have then been tested and the distributed quantities have been acquired in operating conditions.

Contents

List of Figures	X
List of Tables	XI
List of Abbreviations	XVI
1 Introduction	1
1.1 Scenario	1
1.1.1 The road to Electrification	1
1.1.2 Emission Standards for Gasoline and Diesel vehicles .	1
1.1.3 Electric vehicles GHG emissions	5
1.1.4 Electrified vehicles powertrain	5
1.2 Energy storage	9
1.2.1 Energy storage systems classification	10
1.2.2 Battery energy storage	10
1.3 Li-ion batteries	11
1.3.1 Li-ion cells format	14
1.3.2 Li-ion batteries degradation mechanisms	18
Ageing mechanisms on negative electrode	19
Ageing mechanisms on positive electrode	20
Degradation modes	22
1.3.3 Li-ion batteries characterization techniques	22
Capacity test	24
Pseudo OCV test	25
Electrochemical Impedance Spectroscopy (EIS)	25
Incremental Capacity-Differential Voltage (IC-DV)	29
Hybrid pulse power characterization (HPPC) test	30
1.3.4 Second life	33
1.3.5 Recycling	35
1.3.6 Batteries roadmap	37
2 State of the Art on Li-ion cells monitoring	39
2.1 Batteries monitoring and diagnostics	39
2.1.1 Li-ion batteries modelling	39
2.1.2 Battery management system (BMS)	39
2.1.3 Thermal management system (TMS)	42
2.2 Why instrumenting cells?	44
2.3 External sensing	46
2.4 Internal sensing	49
2.5 Scientific research trend	52

3	Sensors	55
3.1	Sensors selection	55
3.1.1	Sensors type classification	55
3.1.2	Optical sensors classification	55
3.2	Rayleigh (OFDR) based distributed fibre optic sensors	59
3.2.1	Fibre optic history	59
3.2.2	Data acquisition system	60
3.2.3	Acquired signals	62
3.3	Sensors calibration	66
3.4	Fibre optic sensors manufacturing process	72
4	Pouch cells instrumentation	79
4.1	Pouch cells manufacturing process	79
4.2	External instrumentation procedure	85
4.3	Internal instrumentation procedure	85
4.3.1	Feasibility checks	85
	Fibre optic sensor survival test in electrolyte	85
	Fibre optic sensor survival test in the sealing region	87
	Partial sealing layout	90
	Fibre optic sensor bonding on anode	92
4.3.2	Instrumented cells manufacturing process	95
5	Cells characterization results	103
5.1	Manufacturing results	103
5.2	Characterization results comparison	104
5.3	Post-mortem analysis	111
6	Experimental tests	113
6.1	Data acquisition system	113
6.2	DFOS signals data analysis	113
6.3	External sensing testing	115
6.4	Internal sensing testing	116
7	Conclusions	123
7.1	Comparison of previous literature studies	123
7.2	Implications of the work	124
	Bibliography	127

List of Figures

1.1	European Union (EU) emission standards for positive ignition (PI) light-duty vehicles (g/km for CO, mg/km for HC, NO _x , PM, and p/km for SPN) [53].	4
1.2	Sensitivity analysis. Electric vehicle lifecycle emissions with use phase electricity based on (a) coal, (b) natural gas, (c) wind, and (d) the prospective green energy scenario where electricity in all lifecycle phases based on wind power [40].	6
1.3	Degree of electrification: typical fuel-efficiency improvement on the same vehicle platform for different electrification levels [129].	7
1.4	Classification of ESSs based on the form of stored energy [77].	11
1.5	General characteristics of different energy storage methods ESS [77].	12
1.6	Ragone plot of various battery technologies [18].	13
1.7	Safety operating window for lithium ion battery [89].	15
1.8	Cells typical format.	16
1.9	Full cell structure.	16
1.10	Overview of electric vehicles commercially available in 2016 [9, 59].	17
1.11	Illustration of ageing effects on battery negative electrode: the capacity fade and the SEI raise [7].	21
1.12	Degradation mechanisms in Li-ion cells [13].	22
1.13	Relationship of the battery ageing extrinsic factors with the affected component, ageing mechanism, potential ageing effects, most pertinent observed effects and most pertinent DM [33, 35, 112, 113, 148, 152].	23
1.14	Cause and effect of degradation mechanisms and associated degradation modes [13].	24
1.15	Constant current-constant voltage (CC-CV) charging protocol.	25
1.16	Time domain plots of the low amplitude AC modulation and response [99].	26
1.17	A typical Nyquist plot [99].	27
1.18	Relationship between the resistances of the AR-ECM with the most pertinent degradation mode (DM), potential ageing mechanisms and most pertinent observed effects [113].	28
1.19	EIS model elements [113].	28
1.20	Relationship between the changes in IC-DV curves with the most pertinent degradation modes, potential ageing mechanisms and most pertinent observed effects [113].	30

1.21	IC and DV discharge curves over cycle number. The changes of the IC and DV curves are related to the most pertinent degradation modes [113].	31
1.22	Applied current pulse to the battery and its voltage response for resistance extraction [48].	32
1.23	Hybrid Pulse Power Characterization Test [25].	34
1.24	Cells life path.	35
1.25	World mining industry production for materials used in LIB in 2017 (data source: USGS 2017 [83]).	36
1.26	Roadmap of Lithium-ion based batteries from present up to >10 years [9].	38
2.1	Battery cell models.	40
2.2	State estimation algorithms.	40
2.3	Main motivation supporting cells instrumentation.	47
2.4	Summary of topics studied in the literature.	53
3.1	Optical sensors classification.	57
3.2	History of optical fibre [1].	59
3.3	LUNA strain sensor scheme [134].	60
3.4	ODiSI-B measurement system. The ODiSI-B measures strain and temperature along the length of the fiber [90].	60
3.5	Rayleigh-based distributed optical fibre sensing working principle.	62
3.6	LabVIEW data acquisition program Block Diagram default functions [90].	63
3.7	The formatting of the Processed Data File [90].	64
3.8	Calibration Setup.	67
3.9	NI RTDs data acquisition system.	67
3.10	Climatic chamber temperature profile applied in the calibration procedure.	69
3.11	Temperature data fitting.	70
3.12	Calibration Signal Decoupling.	71
3.13	Fujikura 70S+ fusion splicer.	73
3.14	Fusion splicing using two identical fibres: A) - B) fibres before alignment; C) - D) fibres after alignment; E) - F) fibres after fusion splicing.	74
3.15	Fusion splicing using two different fibres: A) - B) fibres before alignment; C) - D) fibres after alignment; E) - F) fibres after fusion splicing.	75
3.16	Terminator Quality Comparison.	77
3.17	Splicing quality and frequency comparison.	78
4.1	Pouch Li-ion cell pilot assembly line [141].	80
4.2	Positive and negative electrodes substrate.	82
4.3	Separator (A) and pouch bag film (B) rolls.	83
4.4	External sensing instrumentation procedure.	86
4.5	ZEISS Sigma scanning electron microscope (SEM).	87

4.6	<i>Cressington</i> 208HR sputter coater.	88
4.7	SEM observation results after electrolyte exposure. Only small scratches on fibre coating surface are visible.	88
4.8	Melted PTFE tube in the sealing region.	89
4.9	Temperature sensor vs strain sensor slid into a PTCE sleeve tube in the sensing region of interest in the pouch cell.	90
4.10	Pouch bag damaged by the fusion protection sleeve.	91
4.11	Optical microscope observation of the fibre coating after sealing.	91
4.12	Damage on fibre coating after sealing at 160 °C and 9 bar.	91
4.13	Procedure for pouch bag sealing with sensor.	92
4.14	First attempt to bond the strain sensor on the anode surface using epoxy glue.	94
4.15	Second attempt to bond the strain sensor on the anode surface using SBR.	94
4.16	Comparison between anode original coating and new overcoating.	95
4.17	Comparison between fibre and overcoating before and after electrolyte exposure.	95
4.18	Slurry manufacturing procedure.	97
4.19	Instrumented anode scheme.	97
4.20	Procedure for sensor overcoating.	98
4.21	Procedure for conventional anode removal from the pouch stack.	98
4.22	Procedure for instrumented anode insertion in pouch stack.	99
4.23	Instrumented pouch stack tabs welding.	100
4.24	Manufactured instrumented cell with fibre optic sensor after assembly and sealing.	100
4.25	Instrumented cell electrolyte filling.	101
4.26	Instrumented cell with fibre optic sensor at the end of the manufacturing process.	101
4.27	Instrumented cells test rig.	102
5.1	Cells voltage comparison after electrolyte filling and before formation.	104
5.2	Cells voltage comparison during formation and stabilization.	105
5.3	Cell voltage during EIS.	105
5.4	Cells voltage comparison during EIS.	106
5.5	EIS output at various current amplitude.	107
5.6	EIS curve comparison between internally instrumented and not instrumented cells.	108
5.7	IC curve comparison between internally instrumented and not instrumented cells.	108
5.8	DV curve comparison between internally instrumented and not instrumented cells.	109
5.9	HPPC resistance comparison between internally instrumented and not instrumented cells.	110
6.1	Testing setup: climatic chamber, cells cycler, distributed fibre optic sensors interrogator, thermocouples.	114

6.2	Cells testing at various temperature and current rate test flow.	115
6.3	Cells ageing test flow.	115
6.4	Sensing sections on external instrumented cells.	116
6.5	Point versus distributed experimental temperature measurement: evolution in time.	117
6.6	Point versus distributed experimental temperature measurement: evolution in space.	117
6.7	Distributed experimental strain measurement: evolution in space.	118
6.8	Distributed experimental temperature and strain measurement: evolution in time.	118
6.9	Formation and stabilization cycles of one instrumented pouch cell.	119
6.10	Zoom on one stabilization cycle of one instrumented pouch cell.	120
6.11	Cycling at 1C, 3C, 5C @ 25, 40, 10 °C.	121
6.12	Tmax location during cycling.	122
7.1	Summary of conditions studied in the present work.	124

List of Tables

1.1	Anode materials - Overview including energy density, cost and lifetime [9].	18
1.2	Cathode materials - Overview including energy density, cost and lifetime [9].	18
2.1	Comparison of various battery cooling methods [88].	45
3.1	Comparison between electrical and optical sensors.	56
3.2	Fibre optic sensors monitoring [57].	58
3.3	LUNA Strain Sensor Specifications [134].	61
3.4	ODiSI-B modes of operation [90].	63
3.5	Coefficients and Units.	66
3.6	Calibration equipment operating temperature limits.	68
3.7	Calibration coefficients.	71
3.8	Fusion splicer output after fibre splicing.	76
3.9	Sliced sensors signal quality comparison.	76
4.1	Battery cell manufacturing process summary including material in- and outflow [9].	81
4.2	Anode slurry recipe components proportions.	96
4.3	Instrumented Cells Test Layout.	102

List of Abbreviations

BEV	Battery Electric Vehicle
BMS	Battery Management System
BOL	Beginning Of Life
BOTDA	Brillouin Optical Time Domain Analysis
C-rate	The rate of battery cycling
CAES	Compressed Air Energy Storage
CC	Constant Current
CCS	Carbon Capture and Storage
CF	Capacity Fade
CL	Conductivity Loss
CV	Constant Voltage
DEC	Diethyl Carbonate
DFOS	Distributed Fibre Optic Sensor
DM	Degradation Mode
DMC	Dimethyl Carbonate
DOD	Depth Of Discharge
DPF	Diesel Particulate Filter
DV	Differential Voltage
EC	European Commission
EC	Ethylene Carbonate
ECES	Electro-Chemical Energy Storage
EDC	European Driving Cycle
EDS	Energy Dispersive X-ray Spectroscopy
EEC	European Economic Community
EHT	Electron High Tension

EIS	Electrochemical Impedance Spectroscopy
EKF	Extended Kalman Filter
EMI	Electromagnetic Interference
EREV	Extended Range Electric Vehicle
ESS	Energy Storage System
EOL	End Of Life
EU	European Union
EV	Electric Vehicle
FBG	Fibre Bragg Gratings
FO	Fibre Optic
FOS	Fibre Optic Sensor
GDI	Gasoline Direct Injection
GHG	Greenhouse Gas
GPF	Gasoline Particulate Filter
GWP	Global Warming Potential
IC	Incremental Capacity
KF	Kalman Filter
LIB	Lithium-Ion Battery
HC	Hydrocarbons
HDPE	High Density Polyethylene
HEV	Hybrid Electric Vehicle
HF	Hydrofluoric acid
HPPC	Hybrid Pulse Power Characterization
ICE	Internal Combustion Engine
ICEV	Internal Combustion Engine Vehicle
IPA	Isopropyl Alcohol
LAM	Loss of Active Material
LCO	Lithium Cobalt Oxide
LFP	Lithium Iron (Fe) Phosphate (LiFePO₄)

LLI	Loss of Lithium Inventory
LMO	Lithium Manganese Oxide
LPG	Long Period Grating
LTO	Lithium Titanate Oxide
MHEV	Mild Hybrid Electric Vehicle
NCA	Lithium Nickel Cobalt Aluminium Oxide
NEDC	New European Driving Cycle
NMC	Lithium Nickel Manganese Cobalt Oxide
NMP	N-methyl-2-pyrrolidone
NO_x	Nitrogen Oxides
NTC	Negative Temperature Coefficient
OCV	Open Circuit Voltage
ODiSI	Optical Distributed Sensors Interrogator
OFDR	Optical Frequency Domain Reflectometry
OSI	Optical Sensor Interrogator
OTDR	Optical Time Domain Reflectometry
P2D	Pseudo 2 (two) Dimensional
PC	Propylene Carbonate
PCM	Phase Change Material
PE	Polyethylene
PHEV	Plug-in Hybrid Electric Vehicle
PF	Power Fade
PFI	Port Fuel Injection
PHS	Pumped Hydro Storage
PM	Particulate Matter
pOCV	pseudo Open Circuit Voltage
PP	Polypropylene
PTFE	Polytetrafluoroethylene
PV	Photovoltaics

PVDF	P oly v inylidene d ifluoride
REEV	R ange E xtended E lectric V ehicle
RTD	R esistance T emperature D etector
S-DFOS	S train- D istributed F ibre O ptic S ensor
SBR	S tyrene- b utadiene r ubber
SEI	S olid E lectrolyte I nterface
SEM	S canning E lectron M icroscope
SM	S ingle M ode
SMES	S uperconducting M agnetic E nergy S torage
SNR	S ignal to N oise R atio
SOC	S tate O f C harge
SOH	S tate O f H ealth
SOP	S tate O f P ower
SPN	S olid P article N umber
SWI	S wept W avelength I nterferometry
T-DFOS	T emperature- D istributed F ibre O ptic S ensor
TC	T hermocouple
TIR	T otal I nternal R eflection
TMS	T hermal M anagement S ystem
UHMWPE	U ltra- h igh m olecular w eight p oly e thylene
VC	V inylidene C arbonate
WLTC	W orldwide harmonized L ight vehicles T est C ycle
xEV	G eneric term for electric vehicles including all levels of electric drive

Chapter 1

Introduction

1.1 Scenario

1.1.1 The road to Electrification

Both European and Worldwide regulations proposed in the last decades are trying to push towards a more environmentally friendly way of transportation by supporting the introduction and the spread of more efficient and cleaner technologies.

In order to reduce the greenhouse gas emission and to keep the global temperature increase below 2 °C, the European Union (EU) goal is to reduce carbon dioxide (CO₂) emissions by 20% in 2020, and by 80–95% in 2050 compared to 1990 levels [43]. In the Transport White Paper [44], it is described a way to reduce the transport system emissions by 60% having by 2030 a 50% shift from conventionally fuelled cars and by completely removing them from cities by 2050. In order this shift to happen, cleaner cars with more sustainable fuels are required. This kind of policies are also followed globally [51, 71].

1.1.2 Emission Standards for Gasoline and Diesel vehicles

The first Emissions Directive was published in 1970, under the designation 70/220/EEC and it focused on hydrocarbons (HC) and carbon monoxide (CO) emissions only [10]. At that time, due to the lead content in the gasoline fuel, it was not possible to use after-treatment emission control technologies (catalysts) [135]. Then in 1984, the European Commission (EC) proposed that by 1998 unleaded gasoline must be made available at the gas stations. The availability of unleaded gasoline allowed the publication of the Emission Directive 91/441/EEC, known as Euro 1, for passenger cars only. This Emission Directive was the breakthrough for the catalyst technology in Europe. This Emission Directive was followed by the 93/59/EEC that extended this requirement to both passenger cars and light trucks. In order to have an efficient operation of exhaust after-treatment devices, it is fundamental to have fuel with a very low sulfur content [147]. Thus more stringent fuel regulations defining a maximum gasoline sulfur content of 150 ppm in 2000 and of 50 ppm in 2005 were introduced. Finally, “sulfur-free” diesel and gasoline fuels, with ≤ 10 ppm sulfur content had to be available by 2005 and became mandatory by 2009. Then the Euro 2 standard was introduced with

Directive 94/12/EEC, for passenger cars, and 96/69/EC, for light commercial vehicles. Euro 3 and Euro 4 standards were introduced with Directive 98/69/EC and Euro 5 and Euro 6 limits were introduced with Regulation 715/2007, amended by 692/2008. This regulation provided the automotive industry with a longer timeline to develop strategies for meeting these demanding emission limits.

Thus, HC and CO emissions were a focus since 1970s as emissions of gaseous pollutants from gasoline vehicles have been controlled since then and significant reductions were achieved with the introduction of three-way catalysts in the 1990s.

On the contrary, Particulate Matter (PM) mass emissions were first regulated in 1992 for diesel vehicles only [56]. For gasoline vehicles, PM emissions were not considered an issue, as they were orders of magnitude lower than from diesel vehicles and until the Euro 4 standard, gasoline vehicles had no limitation on PM levels.

The picture changed when in the early 2000s particulate filters (DPFs) were installed on diesel vehicles. At the same time, gasoline direct injection (GDI) vehicles were introduced in the market and started to become popular due to their engines improved efficiency and smaller size over port fuel injection (PFI) ones [4, 53].

In the conventional PFI engine, fuel is injected into the intake port so that both fuel and air simultaneously flow into the combustion chamber during the intake process, and a homogeneous air–fuel mixture is formed. On the contrary, in GDI engines fuel is sprayed directly into the combustion chamber, which leads to incomplete fuel evaporation due to the limited time available for fuel and air mixing, resulting in localized rich combustion and particulate matter (PM) formation [116, 150]. Thus the PM mass and number emissions of GDI vehicles were higher than their PFI counterparts and diesel ones equipped with DPFs. PM emissions reduction from GDI engines can be achieved through hardware or software improvements (including fuel injection timing, shaping and pressure) [21, 37]. Another solution to reduce PM emissions from GDI engines is the use of gasoline particulate filters (GPFs) [73].

GDI engines were firstly developed 100 years ago [97]. This engine was then used in boats applications in the 1930s, for aircrafts applications in the 1940s, and for serial passenger vehicles in 1950s [98]. In the 1990s, with the development of engine management systems, capable of supporting the additional fuel-metering complexity, research on GDIs increased [38] and the first modern GDI vehicle was introduced in 1996 [68]. A great boost towards this kind of technology was given by the European Commission Recommendation 1999/125/EC to reduce CO₂ emissions from passenger cars. In 2009, with Regulation (EC) No 443/2009, the EU introduced mandatory 2015 CO₂ standards for new passenger cars. As a consequence of this regulation, in 2017 GDI passenger cars for the first time exceeded sales of diesel cars in EU (51% vs. 44%) [66]. In 2011, the Euro 5b legislation for the first time included a Solid Particle Number (SPN) emission limit of 6.0×10^{11} p/km (“p” = particles) for diesel (compression ignition) vehicles, based on the findings of the

PMP (Particles Measurement Programme) [54, 55].

Stringent PM mass levels and the introduction of particle number limits for GDI vehicles in the European Union (EU) resulted in significant PM reductions. The EU requirement to fulfil the proposed limits on the road resulted to the introduction of gasoline particulate filters (GPFs) in EU GDI models. The SPN emission limit of 6×10^{11} p/km was introduced for GDIs with Euro 6 from September 2014 for new vehicle types and from September 2015 for all vehicle models with Regulation 459/2012. However, for up to three years after these dates, a particle number emission limit of 6×10^{12} p/km could be applied to Euro 6 GDI vehicles upon request of the manufacturer. This three-year phase-in was allowed in the EU to extend the period of research and development needed to meet the standard. The new additional legislation requirement of achieving the same levels also on the road under real driving conditions resulted in installation of particulate filters for GDIs in EU models. The introduction of a solid particle number limit for the GDIs resulted in a significant decrease of their particulate emissions in terms of mass, solid, and total particle number concentrations. The Euro standards for positive ignition (PI) vehicles are summarized in Table 1.1.

Vehicle classes, according to the Commission Directive 2001/116/EC:

- M1: passenger cars
- M2: small buses (< 5000 kg)
- N1: light commercial vehicles (< 3500 kg)
- N2: large commercial vehicles (3500 – 12500 kg)

For Euro 1 and Euro 2

- N1-I: ≤ 1250 kg
- N1-II: 1250-1700 kg
- N1-III: < 1700 kg

From Euro 3

- N1-I: ≤ 1305 kg
- N1-II: 1305-1760 kg
- N1-III: > 1760 kg

From Euro 5, adopted in 2009, standards are issued by Regulations, which are directly enforceable in all Member States, as opposed to Directives, which had to be transposed into each individual Member State.

Euro	Class	Cycle	NM	AM	CO	HC	NO _x	CF _{NO_x}	PM ¹	SPN ¹	CF _{SPN}
1	M1, M2	EDC	07/'92	01/'93	2.72	970	-	-	-	-	-
	N1-I		10/'93	10/'94	2.72	970	-	-	-	-	-
	N1-II		10/'93	10/'94	5.17	1400	-	-	-	-	-
	N1-III		10/'93	10/'94	6.90	1700	-	-	-	-	-
2	M1, M2		01/'96	01/'97	2.20	500	-	-	-	-	-
	N1-I		01/'97	10/'97	2.20	500	-	-	-	-	-
	N1-II		01/'98	10/'98	4.00	600	-	-	-	-	-
	N1-III		01/'98	10/'99	5.00	700	-	-	-	-	-
3	M1, M2	NEDC	01/'00	01/'01	2.30	200	150	-	-	-	-
	N1-I		01/'00	01/'01	2.30	200	150	-	-	-	-
	N1-II		01/'01	01/'02	4.17	250	180	-	-	-	-
	N1-III		01/'01	01/'02	5.22	290	210	-	-	-	-
4	M1, M2		01/'05	01/'06	1.00	100	80	-	-	-	-
	N1-I		01/'05	01/'06	1.00	100	80	-	-	-	-
	N1-II		01/'06	01/'07	1.81	130	100	-	-	-	-
	N1-III		01/'06	01/'07	2.27	160	110	-	-	-	-
5a	M1, M2		09/'09	09/'11	1.00	100	60	-	5.0	-	-
	N1-I		09/'09	09/'11	1.00	100	60	-	5.0	-	-
	N1-II		09/'10	01/'12	1.81	130	75	-	5.0	-	-
	N1-III, N2		09/'10	01/'12	2.27	160	82	-	5.0	-	-
5b	M1, M2		09/'11	01/'13	1.00	100	60	-	4.5	-	-
	N1-I		09/'11	01/'13	1.00	100	60	-	4.5	-	-
	N1-II		09/'11	01/'13	1.81	130	75	-	4.5	-	-
	N1-III, N2		09/'11	01/'13	2.27	160	82	-	4.5	-	-
6	M1, M2		09/'14	09/'15	1.00	100	60	-	4.5	6×10^{12}	-
	N1-I		09/'14	09/'15	1.00	100	60	-	4.5	6×10^{12}	-
	N1-II		09/'15	09/'16	1.81	130	75	-	4.5	6×10^{12}	-
	N1-III, N2		09/'15	09/'16	2.27	160	82	-	4.5	6×10^{12}	-
6c	M1, M2	WLTC	-	09/'18	1.00	100	60	-	4.5	6×10^{11}	-
	N1-I		-	09/'18	1.00	100	60	-	4.5	6×10^{11}	-
	N1-II		-	09/'19	1.81	130	75	-	4.5	6×10^{11}	-
	N1-III, N2		-	09/'19	2.27	160	82	-	4.5	6×10^{11}	-
6d-temp	M1, M2		09/'17	09/'19	1.00	100	60	2.1	4.5	6×10^{11}	1.5 ²
	N1-I		09/'17	09/'19	1.00	100	60	2.1	4.5	6×10^{11}	1.5 ²
	N1-II		09/'18	09/'20	1.81	130	75	2.1	4.5	6×10^{11}	1.5 ²
	N1-III, N2		09/'18	09/'20	2.27	160	82	2.1	4.5	6×10^{11}	1.5 ²
6d	M1, M2		01/'20	01/'21	1.00	100	60	1.43 ²	4.5	6×10^{11}	1.5 ²
	N1-I		01/'20	01/'21	1.00	100	60	1.43 ²	4.5	6×10^{11}	1.5 ²
	N1-II		01/'20	01/'22	1.81	130	75	1.43 ²	4.5	6×10^{11}	1.5 ²
	N1-III, N2		01/'20	01/'22	2.27	160	82	1.43 ²	4.5	6×10^{11}	1.5 ²

¹ Applies only to vehicles with direct injection engines. ² Kept under annual review to reflect technological progress. NM = New models (month/year); AM = All models (month/year); CF = Conformity factor; EDC = European driving cycle; NEDC = New European driving cycle; WLTC = Worldwide harmonized light vehicles test cycle.

FIGURE 1.1: European Union (EU) emission standards for positive ignition (PI) light-duty vehicles (g/km for CO, mg/km for HC, NO_x, PM, and p/km for SPN) [53].

1.1.3 Electric vehicles GHG emissions

In order to reduce combustion of fossil fuels and mitigate climate change, many governments have introduced policies to promote the spread on the market of electric vehicles (EVs). While conventional vehicles rely on the combustion of fossil fuels for propulsion, EVs use electricity, that is usually stored in Li-ion batteries. Thus EVs have no emission at the tailpipe, however, there are indirect emissions due to electricity production that vary according to the energy source and in some cases can be significant [46, 64]. Thus EVs have a great potential to reduce GHGs emissions, but it is important to consider a lifecycle prospective in order to be able to identify their actual footprint and to compare them with conventional vehicles in an environmental prospective [40]. In [40], four different size on EVs are compared with conventional cars and their GHG emissions are evaluated. The EV technology is still developing and there are both short and long term opportunities to reduce their lifecycle GHG emissions, such as technology and production improvement and the use of a cleaner electricity [40]. Only talking about EVs is not enough to state that this kind of vehicles is cleaner than conventional vehicles. For example, large EVs have higher lifecycle GHG emissions than smaller conventional vehicles. However, EVs with small battery packs suffer from shorter driving ranges and are more dependent on infrastructure in the form of fast charging stations. Thus, at the current state of the technology, finding the right compromise between battery size and charging infrastructure is an important element in maximising the climate change mitigation of EVs. As the technology develops, it is important to keep assessing the environmental impact of EVs so that potential opportunities can be identified in addition to providing directions for Research and Development (R&D) and policy-makers. Also comparing for the manufacturing phase and the End-of-Life (EOL) treatment, EV are more environmentally intensive than conventional vehicles. However, they become more sustainable considering the use phase emissions. In this evaluation it is of fundamental importance the energy source used for charging. In Fig. 1.2, four car segments are considered: mini car (A-segment), medium car (C-segment), large cars (D-segment), and luxury car (F-segment). As shown in Fig. 1.2, charging EVs with coal-based electricity made EV lifecycle emissions 12%-31% higher compared to conventional vehicles (Fig. 1.2a), while using electricity from natural gas made EV lifecycle emissions 12%-21% lower compared to conventional vehicles (Fig. 1.2b). Finally, when powered by wind-based electricity, all of the EVs were below the fossil envelope (Fig. 1.2c) and compared to the ICEVs, the EVs lifecycle emissions were reduced by 66%–70%. Because of the large impact of the electricity source, it becomes counterproductive to promote EVs in regions where electricity is produced from oil, coal, and lignite combustion [64].

1.1.4 Electrified vehicles powertrain

Nowadays vehicles contribute for almost 30% of the greenhouse gas (GHG) emissions worldwide. Today, the number of vehicles around the world is

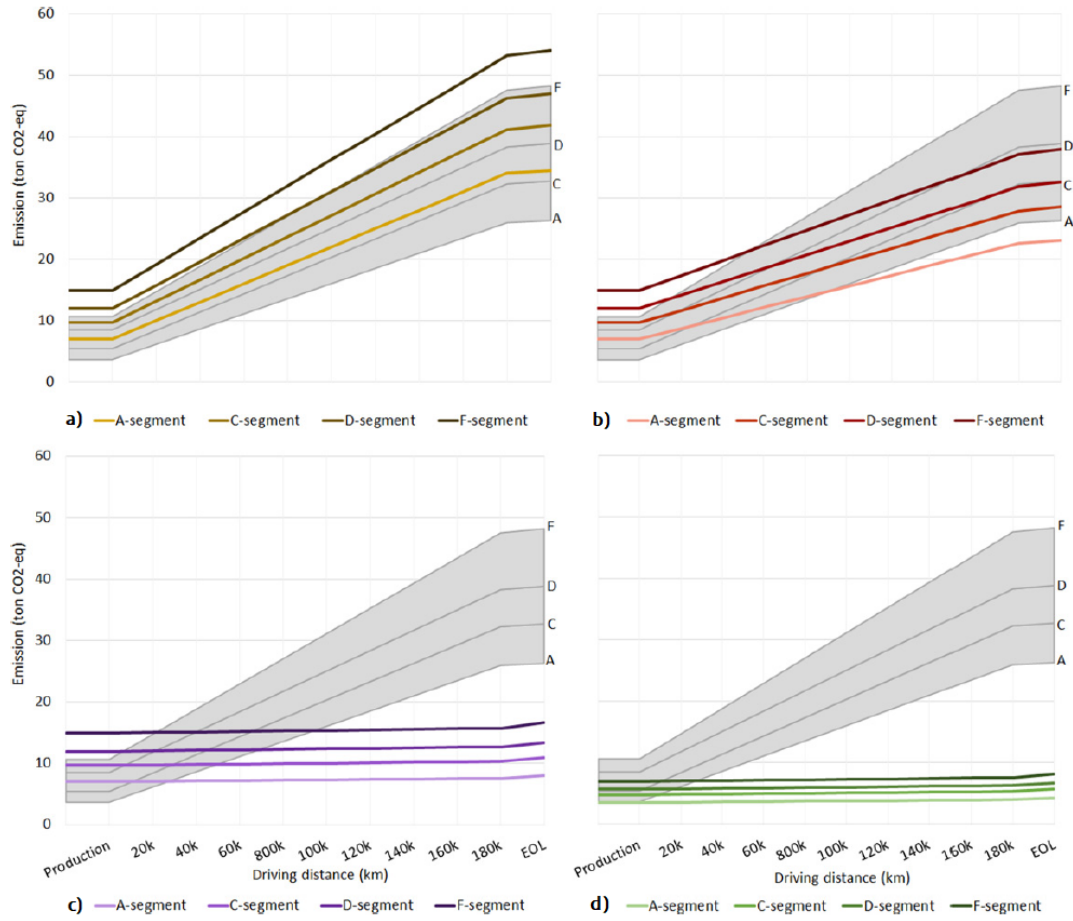


FIGURE 1.2: Sensitivity analysis. Electric vehicle lifecycle emissions with use phase electricity based on (a) coal, (b) natural gas, (c) wind, and (d) the prospective green energy scenario where electricity in all lifecycle phases based on wind power [40].

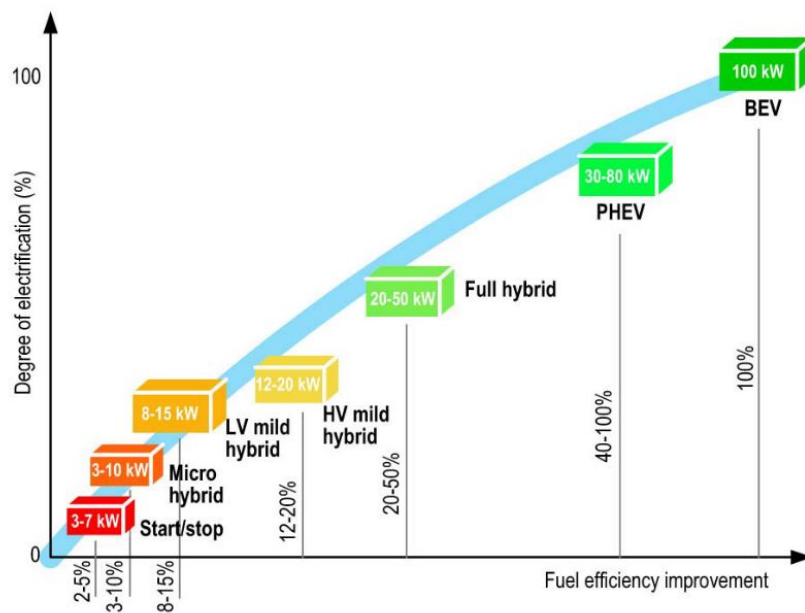


FIGURE 1.3: Degree of electrification: typical fuel-efficiency improvement on the same vehicle platform for different electrification levels [129].

over 900 million. Additionally, 80 million new vehicles are manufactured every year worldwide. These numbers are expected to grow in the next decades, especially in Asia. To reduce GHG emissions and create a more sustainable transportation system, more efficient vehicles with lower fuel consumption are required. Internal combustion engine (ICE) vehicles are characterized by an average efficiency less than 30%, and most vehicles today can achieve only 20-30% of overall efficiency. On the contrary, electric machines, with power electronic converters and energy storage systems (ESSs) are characterized by a much higher efficiency, they can be controlled easily and in a faster way with respect to mechanical systems [12]. Electric motors can operate with efficiency levels as high as 90% and more. Thus, the electrification of conventional ICE powertrains represents a promising solution to achieve these targets. As electrification only implies to power loads by electricity, and it can occur both in propulsion and non-propulsion loads, in vehicles various degrees of electrification are possible. Non-propulsion loads include electrically assisted power steering, electrically driven air conditioning, pumps, fans, and so on. The degree of electrification of a given vehicle is defined as the ratio between the electrical power available on the vehicle with respect to the total available power. As shown in Fig. 1.3, higher fuel efficiency can be gained by increasing the degree of electrification.

Today, most of the vehicles being manufactured have 10%– 20% of electrification. In micro hybrid electric vehicles there isn't an electric motor. It is a vehicle that offers the possibility of energy recovery with regenerative brake and the start and stop technology, that will switch the engine on and off when necessary. Thus the vehicle can be started by the battery pack, it can

capture energy while braking and store it into the battery, and finally it can support the electrical systems onboard when the internal combustion engine (ICE) is shut off [79]. Mild hybrid electric vehicles provide some additional features with respect to micro HEV. These features include the presence of an electric motor/generator that is in parallel with the ICE. The electric motor can assist the ICE when the vehicle is coasting, braking or stopped. Although in a mild HEV the electric motor can assist the ICE, there is no electric-only mode of driving [79]. The electric motor is only used to increase the vehicle performance. Mild HEV provide auto start/stop function, regenerative braking capability, and some use of electric power for propulsion. The engine can be smaller because it is assisted by the electric motor when accelerating. Depending on the system requirements, integration complexity and cost, mild hybrids can be designed as low- or high-voltage systems. This typically provides between 8% and 15% improvements in fuel efficiency [12]. Full hybrid EVs (HEVs) depending on the design of the powertrain can achieve 20%–50% and more reduction in fuel consumption. In a full hybrid electric vehicle, the electric motor can drive the vehicle on its own when needed. A hybrid electric powertrain configuration can be classified as parallel, series and series-parallel or power-split.

- In a parallel configuration, the engine and the electric motor are mechanically connected each other and drive the wheels at the same time. The batteries are recharged through motor/generator during coasting and braking. The parallel configuration has higher efficiency compared to series architecture due to lower losses in electric motor [79].
- The series configuration consists of generator and electric motor and the traction is only provided through the electric motor. The electric motor receives power either through the battery pack or the generator operated by ICE [26, 126]. Thus the engine doesn't have a direct connection to the drive axle, only the electric motor drives the wheels. The engine drives the generator thanks to a gear wheel. The generator produces electricity that is then stored in the battery pack and can be used by the electric motor. This is also known as range extender (extended-range EVs (EREVs) or range-extended EVs (REEVs)) because the range of the vehicle can be increased. The series configuration has higher efficiency in EV mode, but lower efficiency in hybrid mode due to losses in electric motor [12, 79].
- Finally the series-parallel or power-split hybrid configuration uses either a serial hybrid or a parallel hybrid configuration according to the situation. In power-split hybrids, two electric motors are coupled with an engine to create an electrically variable transmission.

Plug-in HEVs (PHEVs) allow to charge the battery both by the engine or by connecting the vehicle into the electrical grid. As HEVs, also PHEV powertrain architecture can be classified into parallel, series and series-parallel, and the vehicle performance is strongly influenced by the powertrain architecture. PHEVs have larger battery packs, therefore they can provide a longer

all-electric drive with plug-in charging [12].

In Battery EVs (BEVs), the traction power is supplied from an electric motor and an electric energy storage system (ESS). One of the main concerns in BEVs is the limited driving range [12].

The market of xEVs are being driven by several factors such as consumer interest, technology, cost, regulatory requirements and a variety of government incentives [79].

1.2 Energy storage

There is a wide agreement that greenhouse gas emissions from the energy sector must be reduced in order to limit to safe levels the climate change [67]. As a consequence, the electric power generation is changing across the world due to the environmental effects of GHG produced by fossil fuels [77]. By adding more renewable energy sources, such as wind and solar, to the power mix, there is greater potential for decreases in harmful emissions [15]. Renewable generation, in particular solar photovoltaics (PV) and wind, are ready to play a key role in this energy system transition. In fact their costs have fallen substantially so that they are now competitive with fossil-fired generation in many parts of the world [52]. The global wind and solar capacity has grown from 80 to 790 GW between 2006 and 2016 [123]. This is promising, as moving electricity generation to renewables, followed by electrification of other key sectors such as heat and transport, is thought to be the most feasible way to rapidly reduce energy sector emissions [22, 160]. Other options, such as nuclear, Carbon Capture and Storage (CCS) and bio-fuels were expected to play significant role, however they are either no longer cost-competitive [114, 123] or have failed to become market-ready [153].

However, renewable energy sources such as wind and solar power are dependent on weather and thus are variable (or intermittent), fluctuating at timescales ranging from minutes to hours to multiple days [58], as well as across years and decades [138, 158]. In order to properly plan and manage the transition to high shares of renewable generation, it is necessary to better understand this variability and its impacts on the power system including both the range of weather conditions that affect wind and solar power generation as well as electricity demand [142].

As the main challenge with renewable energy sources is their unpredictable daily and seasonal variation, energy storage systems (ESSs) play a key role as they can be used to tackle this variation [77]. Furthermore, energy storage could improve the reliability and dynamic stability of the power system, by providing energy reserves that require little ramp time and are less susceptible to varying fuel prices or shortages [15]. According to users energy demand, ESSs can be used to shift the higher peak load to off-peak hours in order to level the generation requirement, allowing generators to operate more efficiently at a stable power level and potentially decreasing the average cost of electricity. Additionally, increasing energy storage capacity can be used to avoid generation capacity increase, to decrease transmission congestion and thus transmission losses, and to help enable distributed generation

such as residential solar and wind systems. Thus the benefits deriving from ESSs are relevant, but it is important to select the best technology according to each application in order to successfully exploit them, as each technology is characterized by different strengths and weaknesses [15].

1.2.1 Energy storage systems classification

According to the form of stored energy, the ESSs can be broadly classified as: mechanical storage system, electro-chemical energy storage (ECES), chemical energy storage, and thermal energy storage. The detailed classification of ESSs is given in Fig. 1.4 [77].

- **Mechanical energy storage:** Energy is stored by doing some mechanical work. This kinetic or gravitational energy is exploited upon its requirement. The mechanical storage systems are further classified into three types based on the working principle of the Energy storage as Pumped Hydro Storage (PHS), Compressed Air Energy Storage (CAES), and flywheel storage.
- **Electro-chemical energy storage:** ECES systems are further classified as batteries energy storage, flow batteries, electrostatic energy storage, and Superconducting Magnetic Energy Storage (SMES).
- **Chemical energy storage:** Energy is stored in the form of chemical energy stored in different materials. It is further classified as hydrogen storage and biofuels.
- **Thermal energy storage:** Energy is stored by heating or cooling a medium and utilizing this stored energy when needed. This stored energy can be used for power generation by applying a Rankine cycle turbine with the system. Thermal energy storage can be further divided into three types: sensible heat, latent heat, and chemical reaction storage.

The main characteristics of the various energy storage methods are summarized in Table 1.5.

1.2.2 Battery energy storage

Today electrified vehicles are propelled by electric motors that are powered by rechargeable battery packs. The main battery systems characteristics include cell chemistry, energy density, power density, cycle life as well as operating conditions [79]. The cell chemistry is extremely important as it dictates inherent safety, shelf life, battery design and so on. Among the various existing automotive battery systems, Pb-acid batteries are relatively less expensive, but they use toxic materials and exhibit the lowest energy density [17]. Ni-Cd batteries show higher energy and power density values compared to Pb-acid batteries, but the electrode materials are toxic (Cd anode) and expensive. Ni-MH batteries are better than Ni-Cd batteries in terms of

Classification of Energy Storage Technologies			
Mechanical storage system	Electro-Chemical Energy Storage (ECES)	Chemical Energy Storage	Thermal Energy Storage
Pumped Hydro Storage (PHS)	Batteries Storage (Lead acid, Li-ion, NiCd, NaS and ZEBRA)	Hydrogen Storage H ₂ storage/ Fuel Cells (PAFC, AFC, PEMFC, MCFC, SOFC)	Sensible Heat Storage (Hot and cold water storage, aquifer storage and molten salt storage)
CAES (D-CAES and A-CAES)	Flow Batteries Redox flow/Hybrid flow		
Flywheel Storage (Low, intermediate and high speed)	Capacitor Storage	Biofuels	Latent Heat Storage (PCM materials)
	Electromagnetic Energy Storage (SMES)		

FIGURE 1.4: Classification of ESSs based on the form of stored energy [77].

energy and power densities with environmentally friendly MH anode, however the self-discharge is higher and they require complex charging protocols. LIBs are relatively more expensive than other cell chemistries, but they provide the highest energy and power densities as well as longer cycle life and can incorporate smart battery management systems [106]. Thus among various battery technologies, Li-ion battery system is the most preferable one for the automotive applications mainly due to their relatively higher energy density [106]. A typical plot used to compare the various battery technologies is the Ragone plot (Fig. 1.6).

1.3 Li-ion batteries

In 2019 Profs. Whittingham, Goodenough and Yoshino received the Nobel prize as they contributed to the invention and development of the Li-ion battery. In 1972 Whittingham discovered a way to make an electrode from a layered material, using it to store lithium ions within sheets. Whittingham used titanium sulphide (cathode) and lithium metal (anode) as the electrodes. The lithium ions could be shuttled from one electrode to the other, creating a rechargeable battery. Whittingham called this kind of storage intercalation. However, since titanium sulphide has to be synthesized under completely sealed conditions, it is quite expensive and when exposed to air it reacts to form hydrogen sulfide compounds, which have an unpleasant odour and are toxic to most animals, and for other reasons, this battery development was stopped [49, 81]. In 1980 Goodenough thought that metal oxides, a combination of oxygen and a variety of metal elements, could allow for charge and discharge at a higher voltage than Whittingham's battery and this would also result in more energy. He invented a rechargeable lithium cell with voltage in the 4 V range using lithium-cobalt-dioxide (LiCoO₂) (cathode) and lithium metal (anode) [100]. LiCoO₂ is a stable positive electrode material which acts as a donor of lithium ions, which means

ESS type	Capacity (MW) ²⁶	Technical maturity ⁸⁹	Efficiency range (%)	Power rating (MW/otherwise mentioned)	Energy rating (MWh/otherwise mentioned)	Storage duration
Mechanical energy storage						
PHS	169 557	Mature	65-85	100-5000	1000+	LTS
CAES	406.96					
D-CAES		Developed	40-60	5-300+	1000+	LTS
A-CAES		R&D Demonstration	75-95	0.1-10 MW small	1-10 MWh small	LTS
		Pre-commercial		100+ MW large	100+ mwh large	
Flywheel energy storage	931	Developed	75-95	0.1-10	0.01-5	STS
Electro-chemical energy storage (ECES)						
Batteries energy storage						
Lead-acid	68.173	Mature	70-90	1 kW up-to 50 MW	0.1-100	MTS, DES
Ni-Cd	30.385	Developed	60-73	10 kW up-to 40 MW	0.01-1500 kWh	MTS, DES
Li-ion	1629.367	Mature	85-95	0.1-50	0.01-500 kWh	MTS, DES
NaS	Na based 201.315	Developed	70-90	50 kW up-to 50 MW	0.01 kWh-100 MWh	STS, DES
ZEBRA		Developed	85-90	1-1000 kW	0.12-5 MWh	STS, DES
Metal Air	15.987	R&D Demonstration	~ 50	0-10 kW		LTS
		Commercial				
Flow batteries						
VRB	71.87	Developed	60-85	5-7000 kW	10-10 000 kWh	LTS
ZBB		R&D Demonstration	60-75	25-2000 kW	50-4000 kWh	LTS
		Commercial				
PSB		R&D Demonstration		1-15	0.01-10+	LTS
		Commercial				
Chemical energy storage						
Hydrogen storage	18	R&D Demonstration	30-50	0.1-1000+	100-1000+	LTS
		Commercial				
Fuel Cell (FC)		R&D Demonstration	~ 50	0-50		LTS
		Commercial				
SMES		R&D Demonstration	90-95	10-10 000 kW	0.1-100 kWh	STS
		Pre-commercial				
Capacitor storage	30.9	R&D Demonstration	90-95	1-10 000 kW	0.001-10 kWh	STS
		Pre-commercial				
Thermal energy storage						
Hot water storage	117	R&D Demonstration	50-90			STS
		Commercial				
Cold water storage	142	Developed	50-90			STS
Molten salt thermal storage	2452	R&D Demonstration	40-93	0-60		LTS
		Commercial				

FIGURE 1.5: General characteristics of different energy storage methods ESS [77].

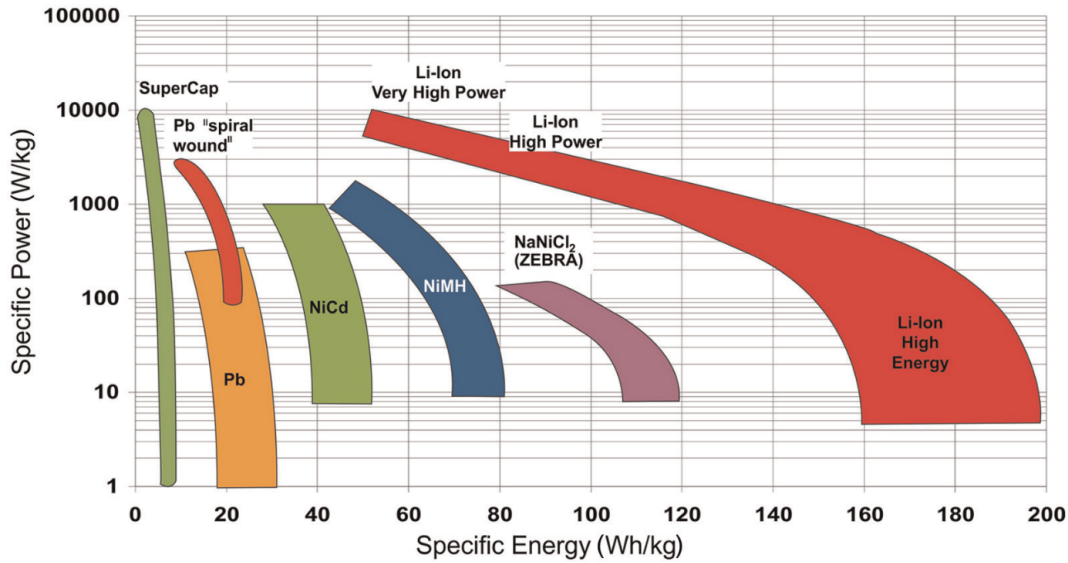


FIGURE 1.6: Ragone plot of various battery technologies [18].

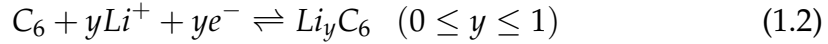
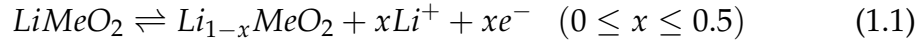
that it can be used with a negative electrode material other than lithium metal [117]. In 1985 Akira Yoshino assembled a prototype cell using as anode a carbonaceous material into which lithium ions could be inserted and as cathode lithium-cobalt-oxide (LiCoO_2) [3]. Using these electrodes together dramatically improved the battery safety. In 1991 Sony, led by Yoshio Nishi, combined Goodenough's cathode and a carbon anode into the world's first commercial rechargeable lithium-ion battery.

Thus, lithium-ion batteries (LIBs) have been commercialized since 1991. Initially, their main application was concerning mobile devices such as cell phones and laptops [145]. Then, the interest in this technology increased and research focused a lot on this topic in order to improve performances of these batteries [16]. Nowadays, thanks to the lithium high density and low weight, Li-ion batteries have penetrated the HEVs and EVs market, making them the most promising candidate for this field of application [7, 144].

Lithium Ion Batteries must be distinguished between primary batteries, or lithium metal batteries, and secondary batteries, or lithium metal and lithium polymer batteries. The working principle of primary lithium batteries consists in the conversion of chemical energy into electrical energy. This conversion process happens by means of electrochemical reduction and oxidation (redox) reactions and these reactions are irreversible. In secondary lithium batteries these reactions are reversible, which means that also the opposite reaction occurs, consisting in the conversion of electrical energy into chemical energy [120].

The basic structure of a Li-ion battery consists of anode current collector, anode electrode, cathode current collector, cathode electrode, separator and electrolyte. In commercial Li-ion batteries, the positive and the negative current collectors are typically made by aluminium and copper respectively [102]. The current collectors role is to conduct electrons for charge transfer

reactions and serve as a substrate for the electrochemically active electrode materials. The positive and negative electrode materials are intercalation materials, as their main function is to host lithium ions. Between the two electrodes there is a not conductive separator that prevents electrical contact but at the same time it is porous as it enables ions to pass through. The battery is then filled with a non-aqueous electrolyte containing lithium salt, such as LiPF_6 and LiClO_4 , which enables Li^+ ionic transfer. During charging Li^+ ions leave the positive electrode, enter the electrolyte, and intercalate into the negative electrode. At the same time, electrons leave the positive electrode and flow into the negative electrode through the outer electric circuit. During this process, oxidation takes place at the positive electrode and reduction occurs at the negative electrode. In order this process to happen, an external source of energy is needed, and the result is that the battery converts electrical energy into chemical energy that is stored inside both electrodes. During discharging the reverse process occurs. The partial electrochemical reactions for a $\text{C}_6/\text{LiMeO}_2$ battery happening respectively for the positive and negative electrode are represented in Eq. 1.1 and 1.2.



The abbreviation Me stands for a transition metal, which in commercial batteries normally is Cobalt (Co) combined with or without Nickel (Ni), Manganese (Mn), or Aluminium (Al) in different ratios [31, 63, 96]. For the case $\text{Me}=\text{Co}$, x is limited to 0.5 to reversibly cycle the positive electrode without causing rapid capacity losses, though x can decrease below 0.5 for modern NMC-type materials. Graphite (C_6) is a typical intercalation material that is generally used for negative electrodes in commercial Li-ion batteries [80, 111, 120].

In order to guarantee Li-ion cells to be safe, they must operate within the safety operating window (Fig. 1.7) that is defined by voltage and temperature limits.

1.3.1 Li-ion cells format

Li-ion cells are usually manufactured in three formats: cylindrical, pouch and prismatic (Fig. 1.8). The coin cell format is usually used for research purpose in chemistry and materials science as it allows to manufacture working cells using a low amount of material. Both cylindrical and prismatic formats present a winding structure where anode, separator and cathode are wrapped along one axis and one plane respectively for the cylindrical and the prismatic format. The pouch format is characterized by a different structure, known as z-folding where each anode and cathode are cut in small sheets and are kept together by the separator that is wrapped between them according to a “z” structure.

In order to have a working cell, it is sufficient to have one anode and one cathode with a separator among them, and this structure is called full cell.

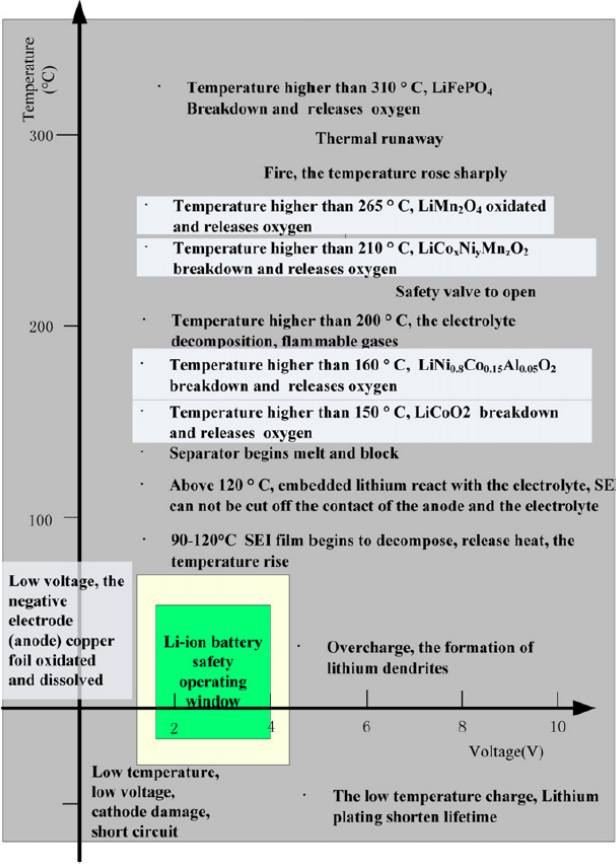


FIGURE 1.7: Safety operating window for lithium ion battery [89].

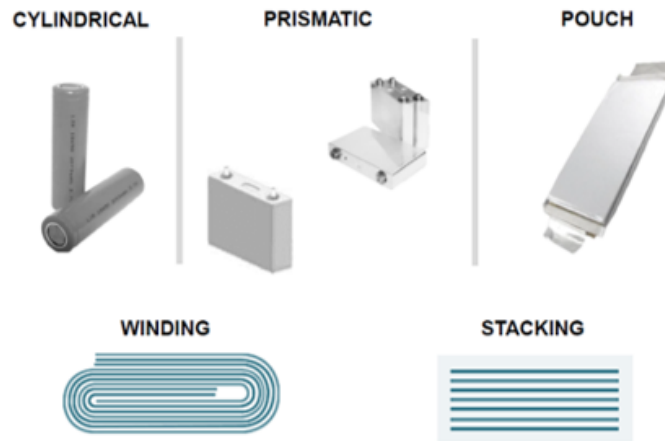


FIGURE 1.8: Cells typical format.

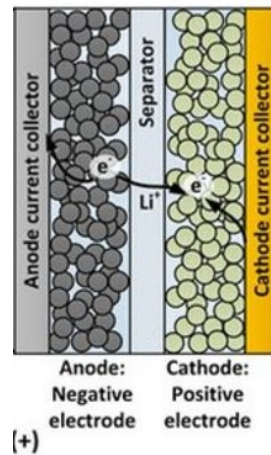


FIGURE 1.9: Full cell structure.

However in order to increase the cell capacity, usually an higher number of electrodes is used, thus the full cell structure is repeated. Full cell systems are usually designed with an anode with larger capacity compared to the cathode in order to prevent lithium plating [39]. This result is usually achieved by using the anode sheet surface that is slightly larger than the cathode sheet and a number of anodes that is equal to the number of cathodes plus one. All electrodes can either be single coated or double coated, in order to increase the cell capacity. An overview of the anode and cathode materials, including energy density, cost and lifetime, is given in Tables 1.1 and 1.2.

Vehicle battery systems are typically equipped with a high number of cells connected electrically in parallel and series to meet the requirements of energy and power [113], resulting in battery modules and battery packs. In Fig. 1.10, an overview of electric vehicles commercially available in 2016 is presented, including vehicles battery pack size and range.

Vehicle Segment	Brand	Model	Model Year	Battery Energy Content (kWh)	Range (km)
Small	Smart	Fortwo	2014	17,6	160
	Toyota	iQ EV	2012	12	85
	Fiat	500e	2015	24	135
	Citroen	C-Zero	2014	14,5	150
	Peugeot	iOn	2014	14,5	150
	Mitsubitshi	i-MiEV	2014	16	160
	VW	e-up!	2013	18,7	160
	Chevrolet	Spark Ev	2015	18,4	130
	Bollere	Bluecar	2015	30	250
	Mitsubitshi	MinicabMiEV	2014	16	150
Average				18.2	153
Median				16.8	150
Medium-Large	BMW	i3	2014	22	190
	Renault	Zoe	2015	22	240
	Volvo	C30 Electric	2015	24	145
	VW	e-Golf	2016	24,2	190
	Nissan	Leaf (2016)	2014	30	250
	Honda	FIT EV	2012	20	130
	Renault	Fluence Z.E.	2015	22	185
	Ford	Focus EV	2015	23	162
	Kia	Soul Electric	2015	27	212
	Mercedes	B-class EL.Dr.	2015	36	230
	BYD	e6	2015	61,4	205
	Nissan	e-NV200	2015	24	170
	Toyota	RAV 4 EV	2014	41,8	182
	Tesla	Model S	2015	75	480
	Tesla	Model X	2015	90	489
Average				36.2	231
Median				24.2	190

FIGURE 1.10: Overview of electric vehicles commercially available in 2016 [9, 59].

TABLE 1.1: Anode materials - Overview including energy density, cost and lifetime [9].

Anode material	Energy density (mAh/g)	Cost	Lifetime
Graphite	372	Medium	Medium
Li ₄ Ti ₅ O ₁₂ (LTO)	175	High	High

TABLE 1.2: Cathode materials - Overview including energy density, cost and lifetime [9].

Cathode material	Energy density (Wh/kg)	Cost	Lifetime
LiCoO ₂ (LCO)	546	Medium	Medium
LiMn ₂ O ₄ (LMO)	410-492	Low	Low
LiNiMnCoO ₂ (NMC)	610-650	High	High
LiFePO ₄ (LFP)	518-587	Medium	High
LiNiCoAlO ₂ (NCA)	680-760	High	Medium

1.3.2 Li-ion batteries degradation mechanisms

The first use of Li-ion battery technology, mainly mobile devices, had a low lifetime need. However, current applications such as HEVs and EVs, are facing some objectives that are clearly defined for service life, typically 10-15 years or 20,000-30,000 discharges [146]. Thus a growing interest is now focused on ageing phenomena considering manufacturers requirements [7]. Li-ion battery ageing phenomena refer to main consequences of both time and use on a battery. In fact, during battery life the available energy and power that can be extracted from the battery is reduced due to degradation. Lithium-ion batteries degradation is an extremely complex process that depends on a variety of ageing mechanisms caused by different factors, both intrinsic and extrinsic [33, 148]:

- **Intrinsic factors:** They include inconsistencies in the manufacturing processes and in the materials used. They can be mitigated by improving quality control, manufacturing processes and battery designs.
- **Extrinsic factors:** They include inhomogeneous operating conditions that a LIB may be subject to, e.g. non-uniform current or temperature distribution within the complete battery pack. They can be mitigated by setting in the BMS a number of variables that include the level of charge or discharge power, the temperature range that the battery operates over and the allowable depth of discharge (DOD) of the battery.

The depth of discharge (DOD) is defined according to Eq. 1.3.

$$DOD = \frac{C_{used}}{C_{nominal}} \quad (1.3)$$

where $C_{nominal}$ is the nominal cell capacity available in the current ageing condition and C_{used} is the portion of capacity that has been removed from the cell. The State of Charge (SOC), the most commonly used index in batteries, is the complement of the depth of discharge as defined in Eq. 1.4.

$$SOC = 1 - \frac{C_{used}}{C_{nominal}} = \frac{C_{residual}}{C_{nominal}} \quad (1.4)$$

The State of Health (SOH) is the battery index that can be used to quantify the battery degradation with respect to its initial nominal state. The SOH is often quantified based on two measures: capacity fade (CF) and power fade (PF) [112]. In Eq. 1.5 the SOH indicator is written in order to express the capacity fade

$$SOH = \frac{C_{nominal}}{C_{initial}} \quad (1.5)$$

where $C_{initial}$ is the capacity of a new cell. Both capacity fade and power fade are strongly related to the available driving range and power respectively. The current SOH definition, doesn't include a clear indication of the ageing mechanisms causing the degradation.

Thus, the main difference between a single cell and a module that has cells connected in parallel is the existence of uneven current distribution when cell properties change due to manufacturing tolerances or usage conditions [112]. For instance, the presence of temperature gradients or different resistance paths within an automotive battery pack will lead to uneven current distribution in the short-term and to cell-to-cell SOH differences in the long-term [113, 161].

In Li-ion cells there are many different ageing mechanisms happening. Ageing mechanisms due to time and use are associated to the various cell components degradation: electrolyte, anode and cathode [61]. The main ageing phenomena come from degradation of electrodes. Electrodes degradation origin can be chemical or mechanical, and electrodes ageing is strongly dependent on their composition. Electrodes degradation can induce modification of the structural properties, a variation of the electrolyte chemical composition, or a loss of active material by the dissolution of material in the electrolyte [152]. Thus, electrodes degradation also induces changes in the electrolyte chemical composition and thus electrolyte ageing.

Ageing mechanisms on negative electrode

Negative electrodes are typically composed of graphite, carbon, titanate or silicone [162]. The most popular anode material is graphite, as it is important in ageing and safety properties of a battery [45]. The main ageing factor of graphite electrode with time, is the development of a solid interface on

the electrolyte/electrode interface, that is named Solid Electrolyte Interphase (SEI) [108]. This solid interphase is naturally created during the first charge. Its role is to protect the anode from possible corrosions and to protect the electrolyte from reductions [60]. The SEI represents a natural barrier between the anode and the electrolyte and consequently provides a guarantee of security [109, 154]. However, as lithium-ion batteries operate in tension outside the electrolyte electrochemical stability range, the SEI is not stable [132]. Thus, the SEI develops over time and this induces continuous loss of lithium ions and electrolyte decomposition [28]. The loss of available lithium due to side reactions at the graphite negative electrode has been reported as the main source of ageing during storage periods [93]. Furthermore, the SEI is permeable to the lithium ions and to other charged elements (anion, electrons) or neutral elements (solvent) [2, 152]. Thereby, the solvent interacts with the graphite after diffusion through the SEI, which induces graphite exfoliation [50] and creates gas which can crack the SEI and therefore allow its expansion [60, 164]. Nevertheless, the gas formation is low and it seems to happen only during storage periods and with high voltage [128]. With time, there is a loss of active surface, increasing electrode impedance. Fig. 1.11 illustrates all these phenomena occurring at the SEI [152]. This phenomenon may take place during utilization of the battery as well as during storage. An high SOC (SOC >80%) should induce an acceleration of these phenomena as the potential difference between electrode interfaces and electrolyte is important [127]. Moreover, inadequate conditions such as high temperature, overcharge and short circuit can accelerate the process [124]. Thus, at high temperatures the SEI may dissolve and create lithium salts less permeable to the lithium ions therefore increasing the negative electrode impedance [82]. On the contrary, low temperatures lead to a decrease of the diffusion of lithium within the SEI and graphite [130, 131], which can overlay the electrode with lithium plating. Lithium plating is a process that consists in lithium-ion building a lithium metal deposit on the anode surface, that involves anode degradation. The SEI formation, its development, and the lithium plating are all responsible for the loss of cyclable lithium [35].

Ageing mechanisms on positive electrode

With battery use, there is no evident modification of the positive electrode morphology [110, 128]. However, with time, the positive electrode is subject to a low alteration, depending on the chosen cathode material [14]. There is also a SEI creation on the positive electrode/electrolyte interface, that is more difficult to detect [75, 94], due to high voltages on this electrode [76]. The principal consequences observed on an aged positive electrode are: wear of active mass, electrolyte degradation, electrolyte oxidation and formation of a SEI, interaction between positive electrode element dissolved within the electrolyte and the negative electrode [70, 74, 110]. These effects are not independent and their respective interaction differs according to the used positive electrode material [95]. As for the anode, ageing effects are strongly related with SOC and temperature.

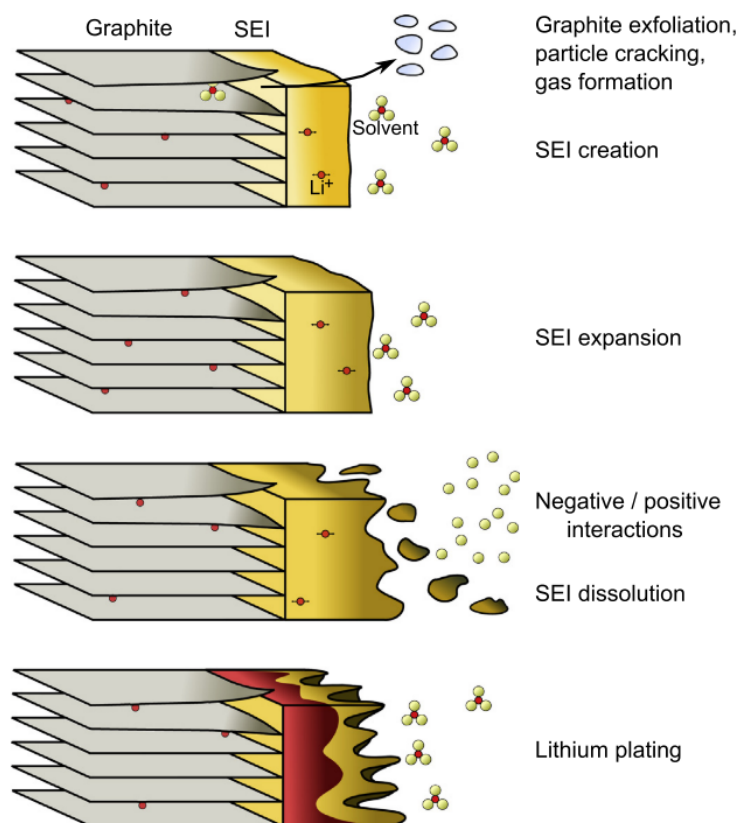


FIGURE 1.11: Illustration of ageing effects on battery negative electrode: the capacity fade and the SEI raise [7].

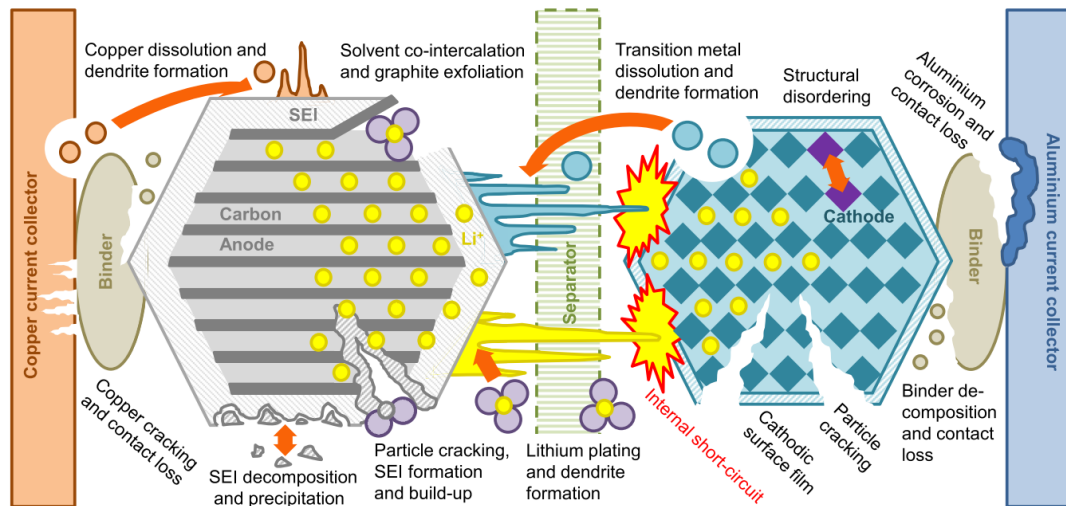


FIGURE 1.12: Degradation mechanisms in Li-ion cells [13].

Degradation modes

Ageing mechanisms happening in Li-ion cells are commonly grouped into three different degradation modes (DMs) [35]:

- **Conductivity Loss (CL):** It includes the degradation of the electronic parts of the battery such as current collector corrosion or binder decomposition [148, 152].
- **Loss of Active Material (LAM):** It is related to structural transformations in the active material and electrolyte decomposition [152]. It includes oxidation of the electrolyte, electrode decomposition, intercalation gradient strains in the active particles, and crystal structure disorder [148].
- **Loss of Lithium Inventory (LLI):** It is attributed to the variation of the number of lithium-ions that are available for intercalation and de-intercalation processes [152]. It includes electrolyte decomposition, lithium plating and formation of Li-ion grains [148].

The causes that lead to CL, LLI or LAM can be very diverse as illustrated in Fig. 1.12 [113]. Tab. 1.13 presents the most pertinent observed effects (capacity fade or/and power fade) and degradation modes (CL, LLI or LAM) for each potential ageing effect, also summarized in the schematic in Fig. 1.14.

1.3.3 Li-ion batteries characterization techniques

In order to characterize Li-ion cells, various techniques and methods have been defined. Each of them is able to determine different aspects of cell performance, requiring various equipment, time duration and computational effort. In this Section a description of these techniques is provided. Some of them have been used to characterize the cells manufactured in this work in

Extrinsic factor	Level	Affected component	Ageing mechanism	Potential ageing effects	Most pertinent observed effects	Most pertinent DM
T	High (>35 °C)	NE	Electrolyte decomposition. Transition metal dissolution.	SEI growth. Micro pore clogging. SEI dissolution. Precipitation of new phases. Formation of dendrites.	PF CF & PF CF & PF PF PF	LLI LLI LAM LAM LAM
		PE	Oxidation of electrolyte. Electrode decomposition.	SPI growth. Gas generation. Precipitation of new phases.	PF CF CF & PF	LLI LAM LAM
T	Low (<5 °C)	NE	Lithium plating. Intercalation gradient strains in the active particles (with cycling).	Dendrite growth. SEI formation. Interstitial site loss.	CF & PF CF & PF CF & PF	LLI LLI LAM
		NE	Lithium plating. Intercalation gradient strains in the active particles (with cycling). Formation of Li grains.	SEI formation. Interstitial site loss. Graphite exfoliation. Isolation of active material. SEI formation and growth.	CF & PF CF CF CF PF	LLI LAM LAM LAM LLI
SoC	Low (<0%)	NE (high potential)	Current collector corrosion.	Loss of conductivity.	PF	CL
		PE (low potential)	Crystal structure disordering. Binder decomposition.	Phase change. Loss of conductivity.	CF & PF PF	LAM CL
SoC	High (>95%)	NE (low potential)	Binder decomposition. Transition metal dissolution. Solvent co-intercalation.	Loss of conductivity. Precipitation of new phases. Formation of dendrites. Phase change. SEI growth.	CF PF PF CF & PF CF & PF	CL LAM LAM LAM LLI
		PE (high potential)	Electrode decomposition. Transition metal dissolution.	Precipitation of new phases. Exfoliation of active material. Gas generation. Phase change.	PF CF CF CF & PF	LAM LAM LAM LAM
ΔDoD	Large (>70%)	PE & NE	Intercalation gradient strains in the active particles.	Volume change.	CF	LAM
			Crystal structural disordering.	Particle cracking.	PF	LAM
			Solvent co-intercalation.	Phase change. SEI growth.	CF & PF CF & PF	LAM LLI
Cycle number	High ^a	NE & PE	Intercalation gradient strains in the active particles.	Volume change.	CF	LAM
			Crystal structure disordering.	Phase change. Particle cracking.	CF & PF PF	LAM LAM

FIGURE 1.13: Relationship of the battery ageing extrinsic factors with the affected component, ageing mechanism, potential ageing effects, most pertinent observed effects and most pertinent DM [33, 35, 112, 113, 148, 152].

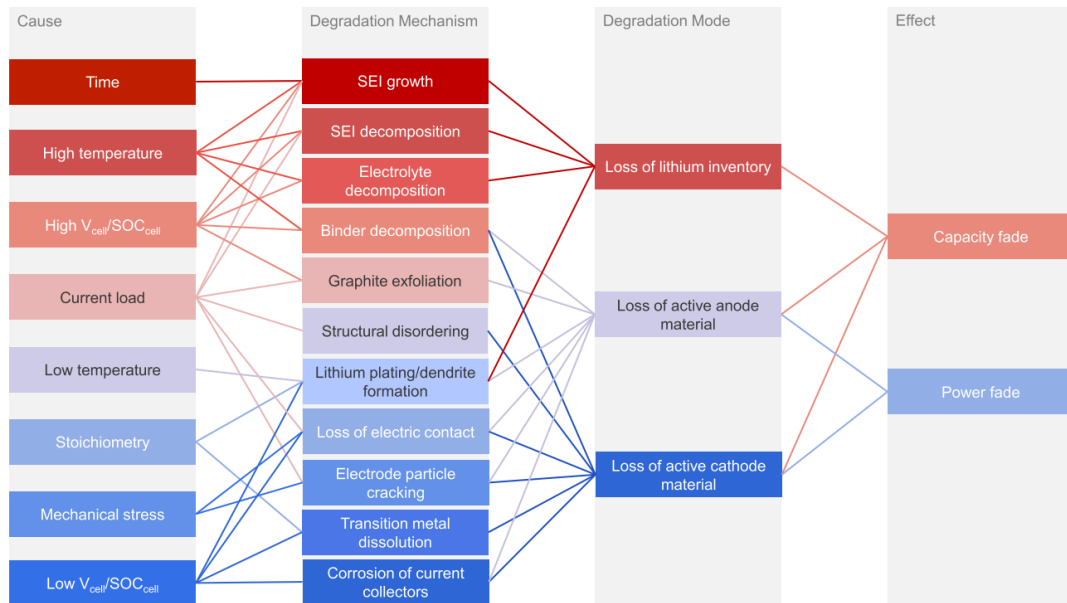


FIGURE 1.14: Cause and effect of degradation mechanisms and associated degradation modes [13].

Section 5.2. These techniques are mainly implemented off-board as they often require long testing time, special testing equipment and boundary conditions. Currently a great effort is involved in modifying these characterization testing procedures to let them be applicable also in on-board applications.

Capacity test

The capacity test determines the quantity of electric charge that a battery can deliver under specified discharge conditions. Firstly each cell is charged to 100% SOC according to constant current - constant voltage (CC-CV) protocol (Fig 1.15). This protocol consists in applying a constant current value in the first stage of the charging profile, limiting voltage to the maximum value V_{max} . In this first stage (CC) the battery voltage will increase as a consequence of the current input. Once the cell voltage reaches this voltage limit value, the current input starts to decrease in order not to overcome the voltage upper limit. Thus in the second stage (CV), voltage will be constant and equal to the voltage upper limit and current will be decreasing. The constant voltage stage is completed when current reaches a certain target value, also called cutoff current.

In order to evaluate the cell capacity, the cell is discharged at 1C to the voltage lower limit. The current rate 1C indicates the current that is necessary to discharge the cell in 1 hour. The voltage lower limit, also called cutoff voltage, is a voltage limitation needed to avoid cell degradation and it is typically set to 2-2.5 V. The cell capacity is defined as the charge dissipated over this discharge event [113].

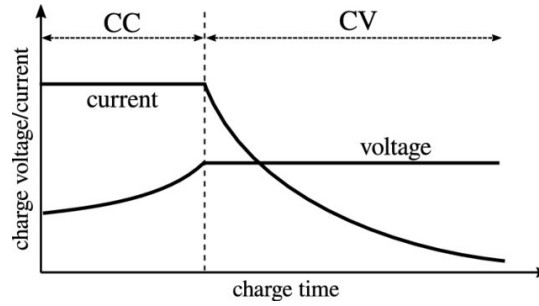


FIGURE 1.15: Constant current-constant voltage (CC-CV) charging protocol.

Pseudo OCV test

The pseudo-OCV test can be performed by discharging from the upper cell voltage threshold (4.2 V) to the lower cell voltage threshold (2.5 V) at low current. The corresponding pseudo-OCV curve is related to the SoC and can be obtained at various ageing stages of the cell (various total number of cycles performed) [113]. This approach allows to define the pseudo-OCV versus SOC curve.

The current amplitude influences the test duration and the results accuracy. Testing at C/25 is the best compromise between time and accuracy. In this conditions, the result allows to obtain a practical capacity close to the maximum attainable, thus this capacity can be used to derive the SOC versus Ah relationship with minimal polarization effects. The pseudo-OCV is the mean of the voltages on C/25 charge and discharge curves. Although this approach is an approximation to the correspondence of the staging phase transformations in the anode, it is accurate enough in the high and low SOC regions to obtain a close-to-equilibrium OCV versus SOC curve [34].

Electrochemical Impedance Spectroscopy (EIS)

The Electrochemical Impedance Spectroscopy (EIS) is a powerful technique for the characterization of electrochemical systems. With a single experimental procedure encompassing a sufficiently broad range of frequencies, the EIS allows to isolate and distinguish the influence of the governing physical and chemical phenomena at a given applied potential [99]. In batteries, this translates in the possibility to decouple the resistance contributions given by various phenomena taking place in the cell such as: SEI, charge transfer and diffusion.

The fundamental approach of all impedance methods is to apply a small amplitude sinusoidal excitation signal to the system under investigation and to measure the response (current or voltage or another signal of interest). A low amplitude sinewave $\Delta E * \sin(\omega t)$, of a particular frequency ω , is superimposed on the DC polarization voltage E_0 . This results in a current response of a sine wave superimposed on the DC current $\Delta i * \sin(\omega t + \phi)$. The current response is shifted with respect to the applied potential (see Fig. 1.16).

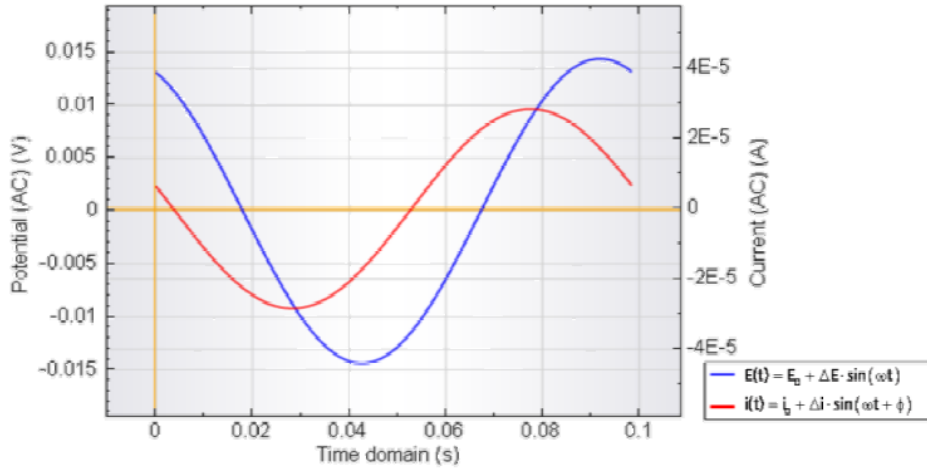


FIGURE 1.16: Time domain plots of the low amplitude AC modulation and response [99].

The Taylor series expansion for the current is given by Eq. 1.6.

$$\Delta i = \left(\frac{di}{dE} \right)_{E_0, i_0} * \Delta E + \frac{1}{2} \left(\frac{d^2 i}{dE^2} \right)_{E_0, i_0} * \Delta E^2 + \dots \quad (1.6)$$

If the magnitude of the perturbing signal ΔE is small, then the response can be considered linear in first approximation. The higher order terms in the Taylor series can be assumed to negligible. The impedance of the system can then be calculated using Ohm's law as in Eq. 1.7.

$$Z(\omega) = \frac{E(\omega)}{i(\omega)} \quad (1.7)$$

This ratio $Z(\omega)$ is called impedance of the system and is a complex quantity with a magnitude and a phase shift which depends on the frequency of the signal. Therefore by varying the frequency of the applied signal one can get the impedance of the system as a function of frequency. The complex impedance $Z(\omega)$ can be represented in polar coordinates, as in Eq. 1.8, where $|Z(\omega)|$ is the magnitude of the impedance and ϕ is the phase shift, as well as in Cartesian coordinates, as in Eq. 1.9, where $Z'(\omega)$ is the real part of the impedance, $Z''(\omega)$ is the imaginary part and $j = \sqrt{-1}$.

$$Z(\omega) = |Z(\omega)|e^{j\phi\omega} \quad (1.8)$$

$$Z(\omega) = Z'(\omega) - j * Z''(\omega) \quad (1.9)$$

The plot of the real part of impedance against the imaginary part gives a Nyquist Plot, as shown in Fig. 1.17. The advantage of Nyquist representation is that it gives a quick overview of the data and makes it possible to do some qualitative interpretations. While plotting data in the Nyquist format the real

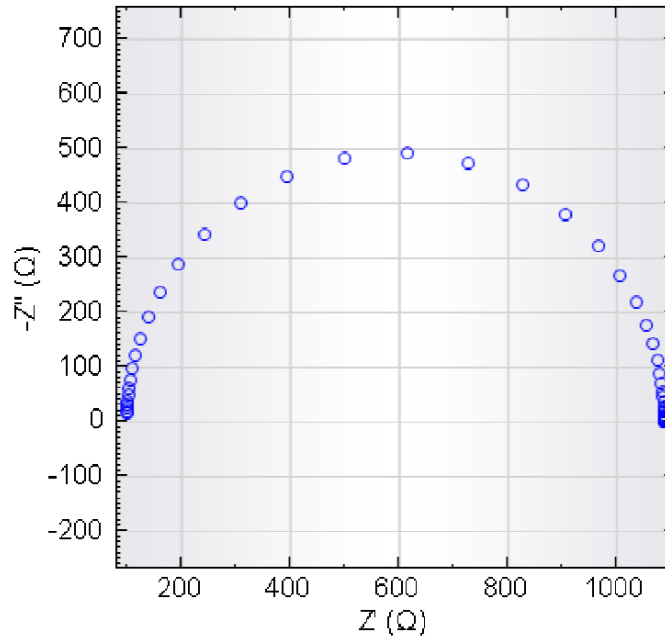


FIGURE 1.17: A typical Nyquist plot [99].

axis must be equal to the imaginary axis so as not to distort the shape of the curve. The shape of the curve is important in making qualitative interpretations of the data. The disadvantage of the Nyquist representation is that one loses the frequency dimension of the data. One way of overcoming this problem is by labeling the frequencies on the curve.

By fitting the EIS spectrum, R_{ohm} is quantified as the horizontal distance between the zero and the point where the EIS spectrum crosses the real axis (high frequencies); and R_{SEI} , R_{ct} and R_W are calculated as the horizontal distances of the each depressed semicircle, respectively [113]. Here it follows a brief explanation of each model element (Fig. 1.19):

- R_{ohm} is used to model the resistance in the current collectors, the connectors and the electrolyte [32].
- R_{SEI} is used to model the loss of lithium inventory (LLI) due to the growth of the SEI layer.
- R_{ct} is used to model the reduction of the charge-transfer Li-ion intercalation and de-intercalation reactions [152], that affect the dynamics of the cell voltage response. It is related to SEI, dendrite growth or micro pore clogging (refer to Tab. 1.13) that are mainly attributable to LLI.
- R_W , defining the Warburg impedance Z_W , is used to model diffusion process happening when the concentration level within a Li-ion particle is different, and this leads to structural transformations in the Li-ion particle and between different Li-ion particles [7, 92, 152].

AR-ECM component	Unit	Most pertinent DM	Potential ageing mechanisms	Most pertinent observed effects
Increase in R_{ohm}	[Ω]	CL	Current collector corrosion. Binder decomposition.	PF CF
Increase in R_{SEI} & R_{ct}	[Ω]	LLI	Electrolyte decomposition. Oxidation of electrolyte. Lithium plating. Formation of Li grains. Solvent co-intercalation.	CF & PF PF CF & PF CF & PF CF & PF
Increase in R_W	[Ω]	LAM	Electrode decomposition. Oxidation of the electrolyte. Intercalation gradient strains in the active particles. Formation of Li grains. Crystal structure disordering. Transition metal dissolution. Solvent co-intercalation.	CF & PF CF & PF CF & PF CF CF & PF PF CF & PF

FIGURE 1.18: Relationship between the resistances of the AR-ECM with the most pertinent degradation mode (DM), potential ageing mechanisms and most pertinent observed effects [113].

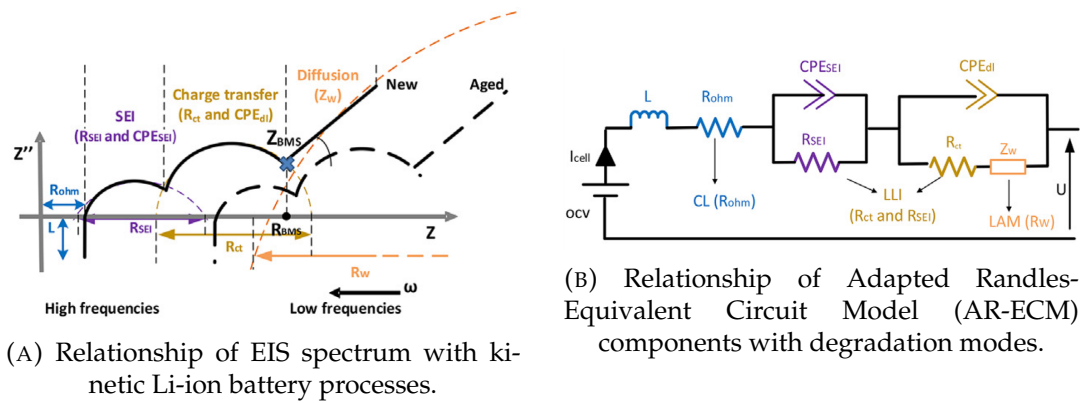


FIGURE 1.19: EIS model elements [113].

Incremental Capacity-Differential Voltage (IC-DV)

The Incremental Capacity (IC)-Differential Voltage (DV) is a method used to identify and quantify changes in the electrochemical properties of the cell based on differences in the cell capacity Q , and in the cell pseudo-OCV (pOCV) curve, when the cell is assumed to be at equilibrium [113]. An approximate equilibrium state is achieved if the cell is typically charged or discharged at very low currents, such as $C/25$, while measuring the Q and the pOCV [35]. However, charging and discharging the cell at such low currents is difficult to perform in a real application since the time required would be prohibitive [91]. Therefore, usually a current of $C/10$ can also be used to generate the required pOCV curves [36].

The IC and DV curves are obtained differentiating Q and pOCV measurements. Even though IC and DV curves are determined from the Q and pOCV relationship, both curves offer different insights into the rate and nature of the degradation within the cell. Mathematically, the IC curve is computed as the gradient of Q with respect to pOCV using Eq. 1.10, performed in MATLAB using the gradient function.

$$\frac{dQ}{d(pOCV)} \approx \frac{\Delta Q}{\Delta(pOCV)} \quad (1.10)$$

The inverse of the IC curve yields the DV curve. Mathematically, the DV curve is derived as the gradient of pOCV with respect to Q using Eq. 1.11.

$$\frac{d(pOCV)}{dQ} \approx \frac{\Delta(pOCV)}{\Delta Q} \quad (1.11)$$

The measurements of the capacity and the pOCV curves are affected by noise. To filter the amount of noise in the measurements, the IC and DV curves are smoothed before computing the derivatives. The filtering procedure firstly consists of averaging pOCV values which are related to any repeated charge measurements, and secondly linear interpolating the remaining data points so that pOCV values exist at equally spaced Q values. To generate the pOCV measurements, both discharge and charge measurement can be used. IC and DV curves allow to identify cells degradation mechanisms such as [113] (Fig. 1.20):

- Conductivity loss (CL): identified by a shifting toward lower voltages in the IC curve and constant capacity in the DV curve.
- Loss of lithium inventory (LLI): identified by a decrease of the height of the peaks and shift toward lower or higher voltages in the IC curve and shifting toward lower capacities in the DV curve.
- Loss of active material (LAM): identified by a decrease of the height of the peaks at approximately constant voltage in the IC curve and by a decrease of the depth of the valleys at approximately constant capacity in the DV curve.

Change in IC curve	Unit	Change in DV curve	Unit	Most pertinent DM	Potential ageing mechanisms	Most pertinent observed effects
Shifting toward lower voltages.	[V]	Lack of change.	[Ah]	CL	Current collector corrosion. Binder decomposition.	PF CF
Decrease of the height of the peaks and shift toward lower or higher voltages.	[Ah V ⁻¹] and [V]	Shifting toward lower capacities.	[Ah]	LLI	Electrolyte decomposition. Oxidation of electrolyte Lithium plating. Formation of Li grains. Solvent co-intercalation.	CF & PF PF CF & PF CF & PF CF & PF
Decrease of the height of the peaks at approximately constant voltage.	[Ah V ⁻¹]	Decrease of the depth of valleys at approximately constant capacity.	[V Ah ⁻¹]	LAM	Electrode decomposition. Oxidation of the electrolyte. Intercalation gradient strains in the active particles. Formation of Li grains. Crystal structure disordering. Transition metal dissolution. Solvent co-intercalation.	CF & PF CF & PF CF & PF CF CF & PF PF CF & PF

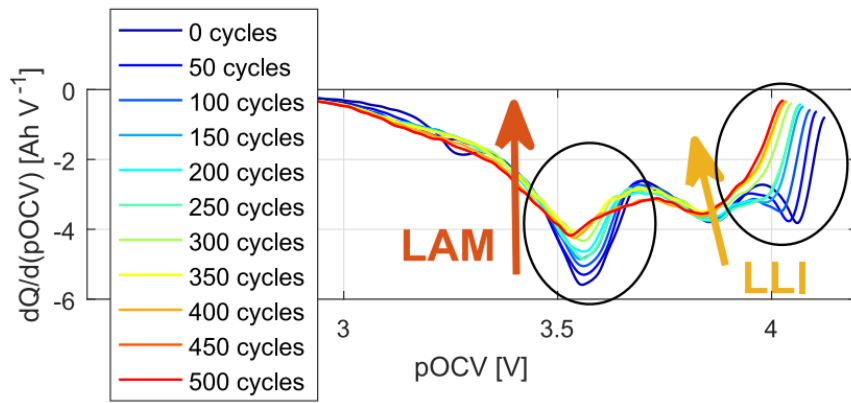
FIGURE 1.20: Relationship between the changes in IC-DV curves with the most pertinent degradation modes, potential ageing mechanisms and most pertinent observed effects [113].

An example of IC and DV curves changing over cycling is shown in Fig. 1.21, where curves modifications due to LAM and LLI are visible.

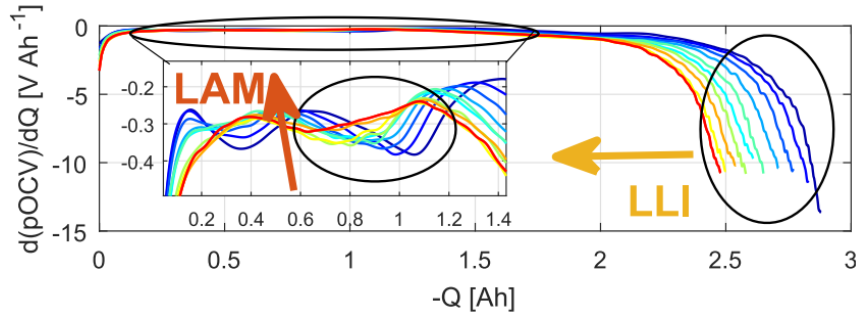
Hybrid pulse power characterization (HPPC) test

The Hybrid Pulse Power Characterization (HPPC) test is used to determine the cell dynamic power capability over the voltage range. It consists in applying a test profile that is made by both discharge and charge pulses [25]. The HPPC test also provides information on the cell ohmic resistance and the cell polarization resistance as a function of capacity. When a current input is applied, the ohmic resistance is responsible for the instantaneous voltage drop and polarization resistance is responsible for the voltage transient (Fig. 1.22). When the HPPC profile is applied, the output voltage response curves are measured. Knowing the value of the applied current pulse, the voltage drops measured can be used to compute the resistance value and the time constants during charge and discharge. If HPPC test is performed at various stages of cell ageing, it is useful to evaluate resistance degradation during subsequent life testing. The base profile consists in 30 s discharge pulse at 100% C-rate, 40 s rest step and 10 s charge pulse at 75% C-rate, as shown in Fig. 1.23a.

This base profile is performed at various depths of discharge, which means at various SOC levels. In order to do, once the base profile has been applied at a certain SOC level, it is necessary to discharge the cell to move to the next SOC level. Typically the base profile is performed every 10% SOC, thus the base profile is followed by a discharge step performed applying a C/3 current, that brings the cell into the next SOC level. After the discharge step, typically a rest period is applied in order to allow the cell to return to an electrochemical and thermal equilibrium condition before applying the next base profile. The full HPPC test is made up of single repetitions of this profile.



(A) IC curve.



(B) DV curve.

FIGURE 1.21: IC and DV discharge curves over cycle number. The changes of the IC and DV curves are related to the most pertinent degradation modes [113].

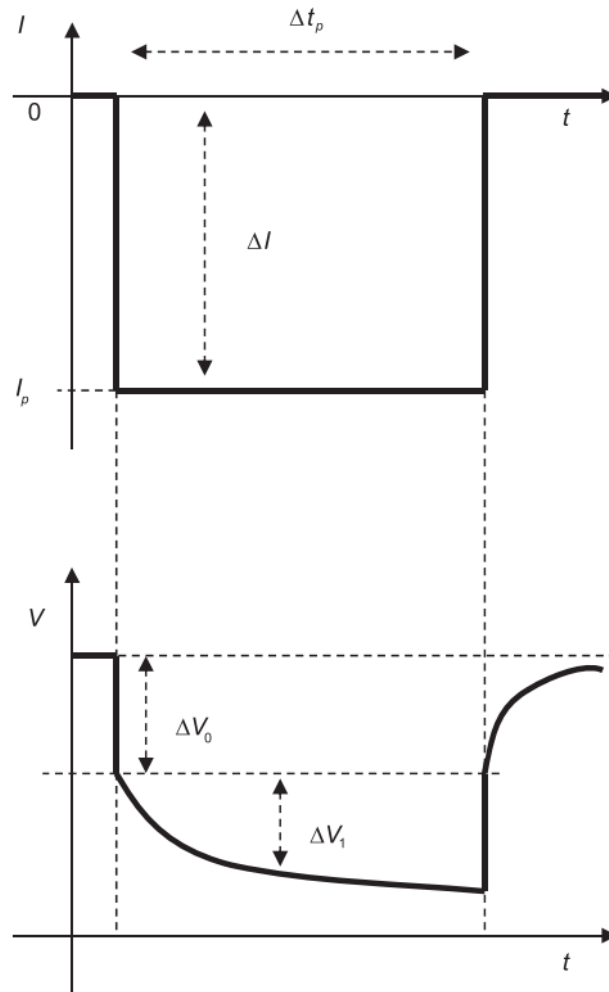


FIGURE 1.22: Applied current pulse to the battery and its voltage response for resistance extraction [48].

The HPPC test begins with a charged device up to V_{max} using the manufacturer recommended procedure. Following a default rest period (nominally a 1-hour rest), an HPPC profile is performed immediately followed by a discharge to the next 10% increment of the rated capacity at the C/3 rate and a default rest. This sequence is repeated until the final profile at or near 90% of the operating capacity removed (or the maximum discharge specified by the manufacturer). The test terminates with a discharge of the device at the C/3 rate to V_{min} and a final default rest. If at any point V_{min} is reached during an HPPC pulse then decrease the current to finish the pulse. If V_{min} is reached in the C/3 discharge portion, stop the test. The voltages during each rest period are recorded to establish the cell OCV behaviour. The sequence of rest periods, pulse profiles, and discharge segments is illustrated in Fig. 1.23b and 1.23c. These figures also illustrate the C/3 discharge to be executed just prior to each HPPC test.

The HPPC test may be performed at the low-current level, the high-current level, or both. Each HPPC test sequence is performed using peak currents scaled to one of the levels. Scaling of the levels is determined by the following criteria. In low current HPPC test, the pulse profile discharge current is at least a C/1 rate; in high current HPPC test, the pulse profile discharge current is selected as 75% of I_{max} (the manufacturer's absolute maximum allowable pulse discharge current for 30 s at some state-of-charge).

It is not possible to compare the value of the resistance obtained from the HPPC with the resistance obtained from the EIS because the resistance obtained from the HPPC takes into account both the ohmic resistance (instantaneous voltage drop) and the polarization resistance. Furthermore, the polarization resistance depends on the duration of the considered pulse (the longer is the pulse duration, the higher is the resistance). Thus, the resistance values obtained from the HPPC can only be compared with themselves (resistance output from other HPPC) to evaluate cells ageing with cycling.

1.3.4 Second life

After Li-ion cells have been employed in the main application, where full performance are required, before recycling they can be given a "second life". Second life can be any application where cells are required to be able to store electro-chemical energy but energy density and power density are not the main focus. This implies that even if a cell, because of ageing during the main application, lost some capacity, the remaining capacity can still be used in a secondary application. On the contrary, it is no more interesting for the main application as, due to ageing, of the overall cell volume and weight, only part of it is useful to store energy, and the remaining part is only adding volume and weight without producing any advantage. A typical second life application is stationary storage.

In this scenario, it becomes fundamental to be able to identify which is the cell state, in order to be able to build battery packs with cells in similar conditions, and to understand if each cell is hazardous or not.

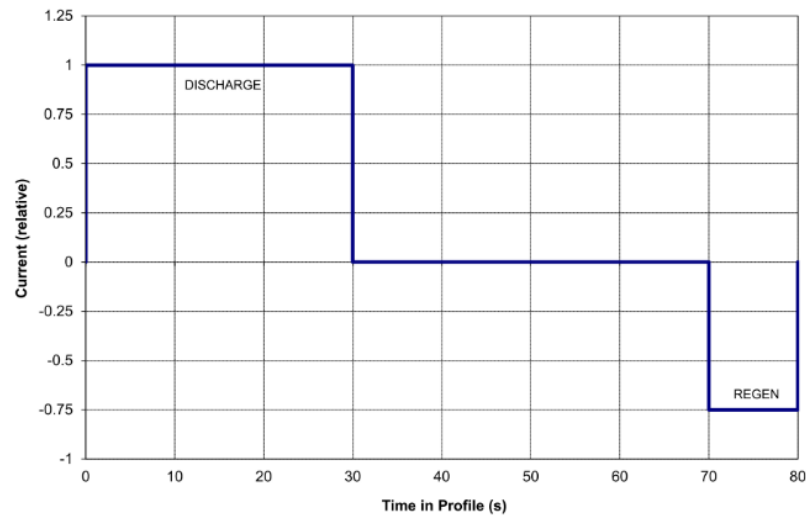
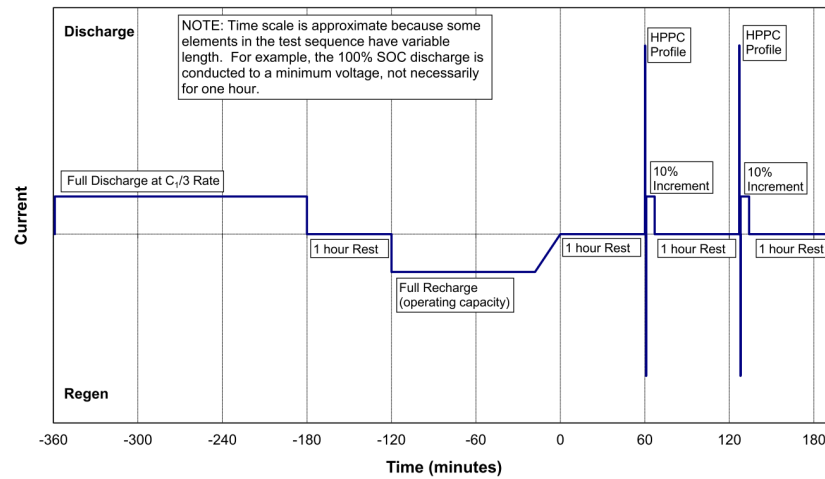
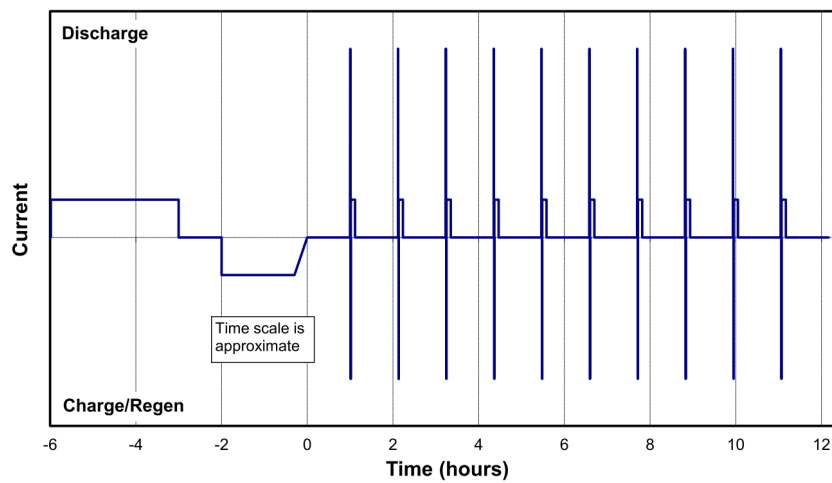


Figure 1. Hybrid Pulse Power Characterization Test Profile.

(A) HPPC test base profile.



(B) Start of the HPPC test sequence.



(C) Complete HPPC test sequence.

FIGURE 1.23: Hybrid Pulse Power Characterization Test [25].

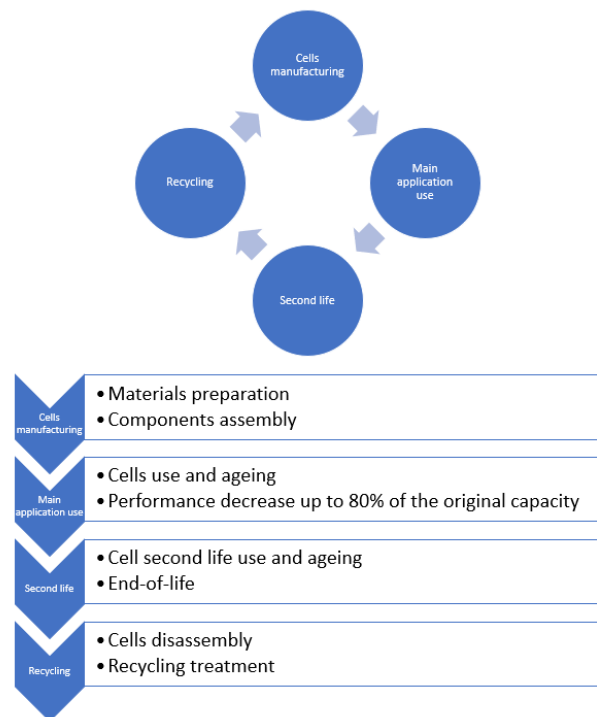


FIGURE 1.24: Cells life path.

1.3.5 Recycling

Lead acid batteries have almost a 99% recycling [42]. On the contrary, the majority of Li-ion batteries are landfilled. With the wide adoption of hybrid and pure electric vehicles, this situation will become even worse. This creates environmental concerns. For example, when left unattended, Li-ion batteries in landfills may catch fire or, if the electrolyte is exposed to water, hydrogen fluoride formation can occur [137]. Additionally, lithium may enter the ground water [125]. All of these are non-options for a sustainable future. The two major mechanisms for Li-ion battery recycling are pyrometallurgical and hydrometallurgical processes. Pyrometallurgical treatment uses high temperature smelting procedures to recover cobalt and nickel as alloys. Hydrometallurgical techniques use chemical leaching to facilitate materials recovery. Li-ion battery recycling has not become more prevalent for three reasons.

1. Current commercialized technologies are limited and do not draw a large enough profit margin to substantiate growth. For the most part, the products of recycling processes are less valuable than the batteries being processed and not all valuable components of the battery are being recovered. The business model for current recycling technologies is not robust.
2. The cathode chemistry of Li-ion batteries is constantly evolving, making it difficult for recycling companies to adapt.

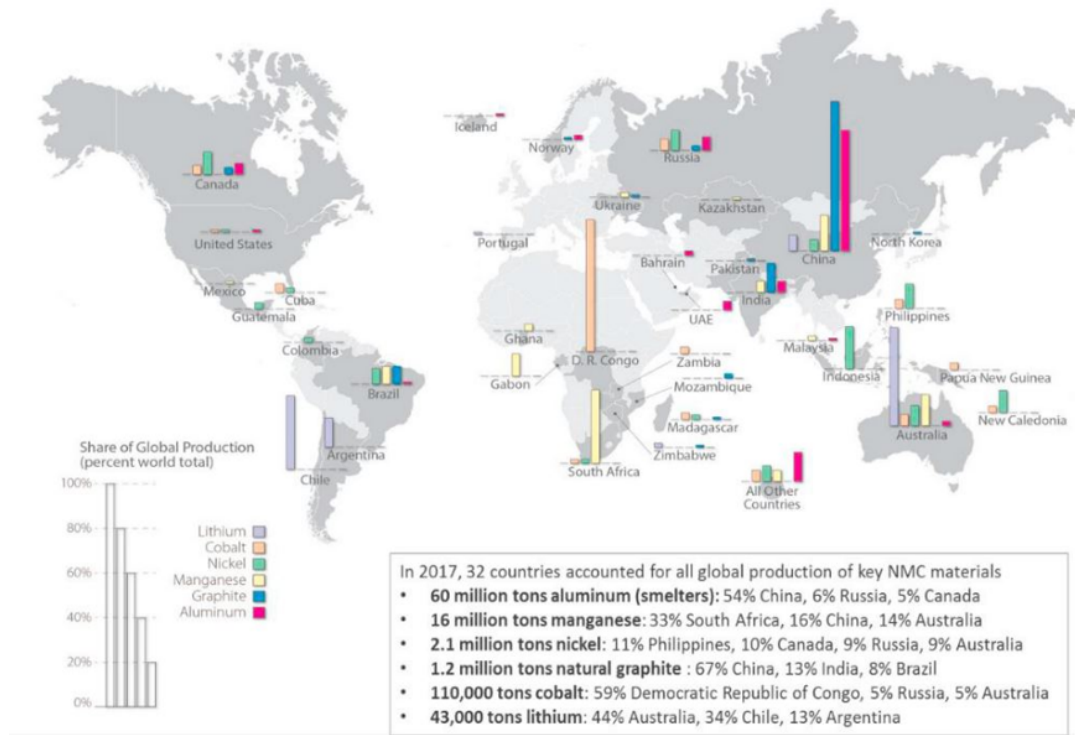


FIGURE 1.25: World mining industry production for materials used in LIB in 2017 (data source: USGS 2017 [83]).

3. And, although end-of-life Li-ion batteries are characterized as hazardous, in many countries government mandates do not exist that would force recycling.

Consumer electronics are currently the largest LIB application. However, LIB have emerged as the battery of choice for electric vehicles because of their high energy and power density and long life [105]. Current mine production of materials for LIB is limited to a few regions around the world potentially creating availability and price issues. The increased demand represented by the widespread adoption of electric vehicles and large-scale stationary storage combined with limited supply could put upward pressure on prices for these materials and potentially interrupt manufacturers' plans and the projected growth of electric vehicle markets [143]. According to data from U.S. Geological Survey (USGS) [149], in 2017, 110000 tons of cobalt were produced globally, with about 60% coming from the Democratic Republic of Congo. China accounted for 67% of the 1.2 million tons of natural graphite produced globally. Lithium extraction was concentrated in Australia (44%) and Chile (34%), with global production totaling 43000 tons. Sixteen thousand tons of Manganese were extracted primarily in South Africa (33%), China (16%) and Australia (14%). Global nickel production totaled 2.1 million tons, with the Philippines accounting for 11%, Canada 10%, while Russia, and Australia each accounted for 9% of the total. In 2017, 32 countries accounted for all global production of these elements (Fig. 1.25).

1.3.6 Batteries roadmap

Improving Li-ion battery performance and reducing cost have become increasingly active areas of R&D as Li-ion battery technology has become the leading technology for vehicle batteries. Research efforts are concentrated around six primary areas [105]:

- reducing the dimensions of active materials to improve ion transport and increase mechanical stability;
- improving the mechanical properties of conductive media;
- adjusting battery chemistry to improve electron transport;
- increasing chemical and thermal stability;
- tuning particle morphology;
- developing coatings to reduce decomposition of active materials, and modifications of electrolyte solutions.

Battery types currently under investigation include lithium metal (lithium metal anodes), solid state batteries that employ solid inorganic or polymer electrolyte, and lithium sulphur with high capacity sulphur-containing cathodes, among others [83]. Whatever path battery technology takes, battery chemistry will likely change significantly over the next decade. Potential changes in battery chemistry, such as developing low-cobalt and cobalt-free cathodes, are important to the supply chain because they may have a significant impact on the demand for critical battery materials and cost.

NMC and NCA are the main cathodes in automotive LIB—are centered on developing nickel-rich, cobalt-free cathodes [8]. According to Avicenne Energy [8], lithium-ion NMC cathode chemistry is shifting from high cobalt content (e.g. NMC 333) to lower cobalt and higher nickel content (e.g. NMC 622 and NMC 811). NCA, the main cathode chemistry used in Tesla cars, is also shifting toward higher nickel contents (and lesser cobalt content). Unlike NMC and NCA, both LMO and LFP have zero cobalt; therefore, most R&D efforts are directed toward improving their performance (e.g. specific capacity, volumetric energy density, and lifetime). Graphite is still the dominant anode material in most LIB, but recently some researchers have introduced silicon as a cheaper alternative to graphite. Silicon has higher energy capacity and relative abundance in the earth's crust.

Fig. 1.26 shows a roadmap of Lithium-ion based batteries from present up to more than 10 years.

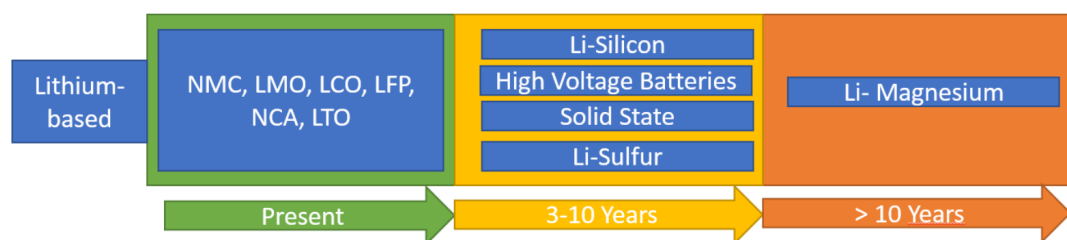


FIGURE 1.26: Roadmap of Lithium-ion based batteries from present up to >10 years [9].

Chapter 2

State of the Art on Li-ion cells monitoring

2.1 Batteries monitoring and diagnostics

2.1.1 Li-ion batteries modelling

It is very important to know which is the state of the battery in terms of operating temperature, residual capacity and residual number of cycles. This becomes particularly important when dealing with multiple cells, as the cell in the worst condition will limit performance of the whole battery pack. In order to estimate the state of a cell, many different algorithms have been developed, based on various models. They are mainly based on voltage, current and surface temperature measurement.

Battery models can be mainly classified in electrochemical models and empirical models (Fig. 2.1a). In electric vehicles applications, equivalent circuit models are the most commonly used as they represent a compromise between accuracy and computational effort. Fig. 2.1b shows an example of equivalent circuit model. Based on these models, state estimation algorithms such as Coulomb counting (Fig. 2.2a), or observers such as Kalman Filter (KF) (Fig. 2.2b) or more complex models are implemented. However, Li-ion batteries are very complex systems and it is hard to model all the various degradation mechanisms occurring in cells over time in order to be able to provide accurate details on cells state.

2.1.2 Battery management system (BMS)

Battery models and algorithms are implemented on-board vehicles in the Battery Management System (BMS). The BMS is fundamental in a Li-ion battery pack, as it performs key functions such as cells balancing, state of charge (SOC), state of health (SOH) and state of power (SOP) estimation, failure prevention and battery protection [119]. A BMS today typically monitors parameters such as voltage, current and external temperature, and it uses this information to estimate the cell state. Common methods implemented on a BMS include Coulomb counting, open circuit voltage (OCV)-based approaches and dynamical model-based approaches [119]. Coulomb counting is a very simple technique used to compute SOC. It consists in integrating current over time in order to compute the used capacity and dividing it by the

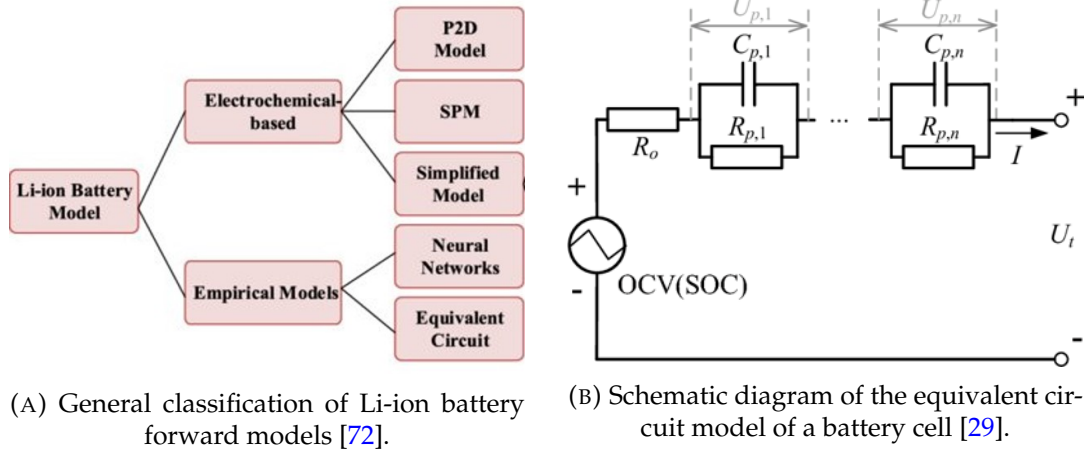


FIGURE 2.1: Battery cell models.

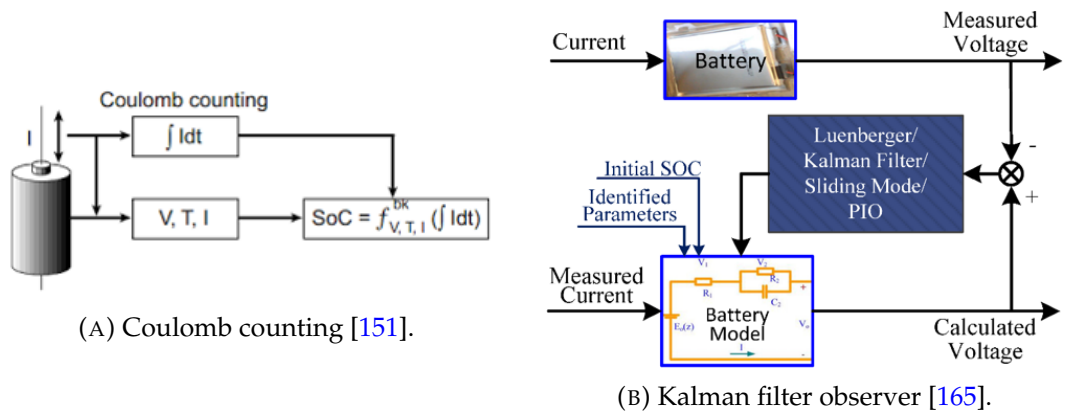


FIGURE 2.2: State estimation algorithms.

battery maximum capacity. Thus, in this technique, an accurate current measurement results to be fundamental as it strongly influences the estimated SOC. This can be a challenge in fielded battery packs, where low-cost current sensors are typically used and they are characterized by measurement drift errors that accumulate over time. A further limitation of this technique is the uncertainty on the initial SOC and the variability of the maximum cell capacity mainly due to cell ageing or environmental temperature variation. To overcome these limitations and improve the SOC estimation, [104] presents an enhanced Coulomb counting method, that uses derived empirical relationships between initial SOC, voltage and current and that dynamically recalibrates the battery maximum capacity. These modifications allow to have an SOC maximum estimation error of 3%, even if it is not explained it that maximum estimation error also holds when different and more aggressive xEV-relevant battery loading profiles are applied [119]. Open circuit voltage (OCV)-based approaches allow to compute an estimation of the battery OCV by applying a certain charge-discharge profile and letting the battery rest for a sufficient duration of time [24, 86, 115]. Once obtained the SOC-OCV relationship, it is possible to estimate the SOC. However, this method is not suitable for real applications when it is not possible to wait for long relaxation time as a real-time estimation is required. Dynamical model-based approaches can be classified into equivalent electrical circuit modelling and electrochemical modelling. The equivalent electrical circuit modelling is very popular in xEV applications and lots of research is carried out in this area. Many different models of various degrees of complexity and involving a different number of parameters have been developed over time. In [19] a non-linear electric circuit model based on impedance spectroscopy approach has been developed to model an absorbent glass mat lead-acid battery. In [65] a comparison among different electric circuit equivalent models of lithium-ion cells is presented. According to this comparison, the dual-polarization model, that consists in modelling separately the concentration polarization and the electrochemical polarization, results to be the most accurate model to estimate SOC. In [85] a reduced order model of a Li-ion cell in conjunction with an Extended Kalman Filter (EKF) is used to estimate SOC. In order to account for model errors, this approach consists in computing the measurement noise covariance in the EKF and in modifying it based on the estimated SOC, the current, and the dynamic of diffusion, charge transfer and double layer. In [86] the authors underline that the OCV versus SOC relationship is not only dependent on the cell chemistry, but also among cells with the same chemistry there is a variation from one Li-ion cell to the other. In order to minimize the variation across different cells, a new definition of capacity is proposed. This implies that different cells are characterized by different capacities. Thus, it is necessary to simultaneously estimate not only the SOC but also the capacity of each cell and this is performed by implementing a dual EKF. Furthermore, as in [85], the measurement noise covariance is adaptively updated in order to account for model errors. In contrast to equivalent electrical circuit models, that pretend to represent the cells behaviour using equivalent circuit elements, electrochemical models attempt to build a cell

model that is based on first principles. In [133] a review of these models, including the pseudo two-dimensional model and the porous electrode model is presented. These models represent a trade-off between model realism and solution time. In [101] a partial differential equation-based observed was developed by using the back-stepping control approach.

2.1.3 Thermal management system (TMS)

The Battery Management System (BMS) is in charge of estimating the battery relevant states, such as State-of-Charge and State-of-Health. Temperature measurements are essential for the right estimation of these states. Temperature measurements are also fundamental to ensure the battery is working in safe conditions, in order to prevent dangerous situations, but also to maximize the performance and cycle life of batteries [120]. In fact, the performance, lifespan and safety of Li-ion battery are strongly associated with their operating temperature. Improper temperature will lead to the power/capacity degradation, shorten the cycle life and may even cause the thermal runaway thus results in fatal disasters [88]. Thermal runaway is a process where elevated temperatures trigger heat-generating exothermic reactions, raising the temperature further and potentially triggering more deleterious side reactions. The onset temperature for thermal runaways tends to occur in the 100 °C e 150 °C range [6].

Large temperature imbalance among cells or within each cell may also cause the failure of battery. Therefore, it is suggested that Li-ion batteries should be maintained in a temperature range of 20–60 °C with the temperature difference no more than 5 °C [88].

During operation, quick thermal gradients occur. A fast and accurate temperature monitoring thus results to be challenging. When selecting the proper measurement method, aspects such as measurement range, accuracy, resolution, and costs of the method need to be considered. At present, the most used methods include traditional temperature measurement methods, such as thermistors and thermocouples. However, several recently introduced methods, such as impedance-based temperature indication and fibre Bragg-grating techniques, are under investigation in order to determine if those are suitable for large-scale introduction in more sophisticated battery-powered applications [120].

Thus, an effective thermal management system is of critical importance to control the batteries within a desired temperature range and address the corresponding problems. To have a better understanding of the battery thermal behaviour and give insights to the thermal effects of TMSs, it is essential to develop an accurate thermal model for Li-ion batteries to conduct numerical simulations [88]. A battery thermal model is based on formulations such as energy conservation, heat generation and boundary conditions. However, a thermal model alone is normally not precise enough to predict the battery thermal behaviour. Therefore, the thermal model is always coupled with an electro-chemical or equivalent circuit model. The most prevalent electro-chemical model is the pseudo two dimensional (P2D) model and a variety

of simplification methods have been proposed to reduce the computation complexity, while the most popular equivalent circuit model is the Thevenin model which utilizes RC networks [88].

TMSs which could effectively control the battery temperature are of great significance in ensuring the performance and safety of Li-ion batteries. The cooling strategies are categorized into air, liquid, phase change (liquid-vapor) and phase change materials (PCM) based systems according to their cooling media. Among these approaches, the air and liquid cooling are conventional methods which have been widely adopted in commercial electrical vehicles. The main advantages of active air cooling include the low cost, simplicity and easy availability of coolant materials. In recent years, developments of air cooling have been focused on the optimization of geometric layouts and operating parameters. The efficiency of thermal management can be enhanced by introducing forced liquid systems, that are characterized by a heat removal coefficient higher compared to air cooling. Studies on indirect liquid cooling were focusing on about how to improve the channel geometry, system structures and coolant heat transfer coefficient. The mutual problem of the forced air and liquid thermal management is that the addition of extra components such as valves, blowers/pumps and cooling ducts/channels will raise the weight and space utilization of TMSs [88]. To address this issue, it is possible to use passive thermal management techniques that take advantages of latent heat during the phase change process. Boiling cooling is able to remove a large amount of heat in a short time but its feasibility remains to be validated. Similarly, heat pipes have been extensively used in many fields such as electronics thermal management but have not been put into practice in TMSs. In order to develop a heat pipe based TMS with good thermal performance it is fundamental the selection of proper working fluids, a good contact between heat pipe and batteries and an effective cooling method [88]. The phase change (solid-liquid) cooling, referred to as PCM cooling, is a promising alternative for conventional thermal management strategies that has an excellent performance of temperature reduction and uniformity although the application of them still faces some challenges. One of the main problems is the poor thermal conductivity of PCMs. Another problem is the potential failure caused by the complete melting of phase change substances. To address this problem, the forced air and liquid cooling as well as heat pipe techniques are integrated into the PCM systems to recover the latent heat but this has the drawback of compromising the simplicity and compactness of the system. Also the increase of weight and cost still represent a limitation to its commercialization. Tab. 2.1 summarizes the comparison of various battery cooling methods including forced air cooling, liquid cooling, heat pipe cooling and PCM cooling.

Compared to the great attention paid on battery cooling, battery heating techniques are comparatively neglected, however this limits the application of Li-ion batteries in cold climates. Each of the existing battery heating methods has their own advantages and deficiencies. Therefore, an effective system to warm up the batteries quickly in an economical and simple way is still needed to be developed [88]. Due to their fundamental importance, the

improvement of the existing TMSs is supposed to be paid more attention to enhance the performance and safety of Li-ion batteries [88].

2.2 Why instrumenting cells?

In order to guarantee effective control of the battery pack by the battery management systems (BMS), it is necessary to have a better understanding of real-time monitoring of internal cells state with accurate sensors [23, 139]. Batteries are complex systems as they involve multidisciplinary knowledge and phenomena. Batteries research involves the development of means to cost-effectively monitor, predict and management cells key performance such as capacity, life, safety limits as all these aspects still represent a technological challenge to be solved [41].

As batteries are complex systems, and because in practical applications high performance are required to them including aggressive operational demand and severe cost constraints, the battery management results to be very challenging [30]. During charging and discharging of a cell, a wide range of processes happen including chemical and electro-chemical reactions, phase change reactions, electronic and ionic transport through the various cell components such as liquids/gel electrolyte, porous separators, composite electrode materials, etc. All there process are coupled and depend on the cell operating parameters [69].

Because of cells complexity and because of many processes coupled and influenced by the operating parameters, to capture and predict many of the degradation and failure mechanisms happening in cells results to be very hard. Even the best theoretical models cannot do so, as unpredictable operating and environmental stresses, defects, manufacturing imperfections and other physical realities also need to be taken into account [121].

Because of the high degree of complexity of cells, considering both physical and electro-chemical phenomena, and because of the lack of a real-time information on degradation mechanisms, physical models cannot provide a great utility to fielded BMS. In fact, today BMS usually monitor quantities such as voltage, current and surface temperature and use these information to estimate important index such as the battery state of charge (SOC), state of health (SOH) and state of power (SOP), to balance cells within a battery pack and to assure the battery works within its safety operating limits. However, none of these quantities provides a direct information on the actual physical and chemical internal state of the cell. The voltage signal provides a measure of the overall measure of changes in potentials, but it doesn't provide critical information on the state of each electrode. Furthermore, the potential drop across the whole cell depends on the cell's variable internal resistance and this aspect becomes critical at high operational currents, that is a common scenario for xEVs applications [23].

Recent studies are focusing their attention on battery strain signals as input parameters for the BMS to provide further information about the battery state and safety. The Li-ion cells working principle is based on Lithium ions intercalation. The Lithium ions insertion/release into/from the electrodes active

TABLE 2.1: Comparison of various battery cooling methods [88].

	Advantages	Disadvantages
Forced air cooling	<ul style="list-style-type: none"> - Low cost - Simplicity of appliance - Highly commercialized - High lifespan - Applicability for different cell types - Can be used for battery heating - Easy accessibility for cooling media 	<ul style="list-style-type: none"> - Large space need - Noise problem - Low efficiency - Poor thermal performance - Low temperature uniformity
Liquid cooling	<ul style="list-style-type: none"> - Large temperature drop - Highly commercialized - High efficiency - Can be used for battery heating - Applicability for different cell types - High temperature uniformity 	<ul style="list-style-type: none"> - Potential leakage - High cost - Extra weight - Increased complexity - Maintenance difficulty
Heat pipe cooling	<ul style="list-style-type: none"> - High compactness - High efficiency - High lifespan - Relatively high thermal performance 	<ul style="list-style-type: none"> - Relatively high cost - Contact resistance - Not commercialized - More suitable for prismatic cells
PCM cooling	<ul style="list-style-type: none"> - Low cost - High compactness - Large temperature drop - High efficiency - Energy storage ability - Relatively uniform temperature distribution - High lifespan 	<ul style="list-style-type: none"> - Volume expansion - Flowability - Extra weight - Not commercialized - Poor thermal conductivity - Potential liquid leakage after melting

material is associated with structural changes in the electrode active materials and thus with volume change and this causes stress on the electrodes, particularly on the anode as in most of Li-ion chemistries, the cell volume change is mainly caused by the anode. Thus the cell expands during charge and contracts during discharge [62, 84, 163].

When the battery is fully charged, Lithium ions intercalate into the anode thus the anode holds the lithium ions and it expands. At the end of the charging step, which produces a state on stress in the anode, there is a relaxation step due to the rearrangement of the lithium ions in the active material. There are some conditions such as high residual stored energy, high currents and low temperatures, which imply a larger relaxation time for the electrodes. The longer is the relaxation time, the longer is the time the battery exercises a higher field of stress. During discharging the Lithium ions de-intercalate from the anode thus it contracts. On the contrary, the cathode expands during discharging as it accepts the Lithium ions back, however the cathode expansion is usually much smaller than the anode [163].

In the following sections it is provided an overview of the state of the art of sensors used for cells monitoring. The discussion is distinguished in external and internal monitoring.

The main motivation supporting cells instrumentation is summarized in Fig. 2.3, further details on cells degradation modes are presented in Tab. 1.13.

2.3 External sensing

In [140] two Fibre Bragg Gratings (FBGs) sensors have been used to measure a pouch cells surface temperature and strain and these results have been compared with NTC thermistor and electrical strain gauges. The FBGs used are inscribed into polyamide-coated silica fibers. The core diameter and cladding diameter are 8 μm and 125 μm , respectively. The diameter of the coated fiber is approximately 155 μm . The Bragg wavelengths of the FBG sensors is 1555 nm and 1560 nm, respectively. For the test setup, the cell was clamped between two acrylic glass sheets and 2 cm-thick insulative Styrofoam sheets to simulate the module pressure and thermal environment. In addition to the FBG sensor signals current, voltage and temperature signals were monitored. The setup was arranged in an environmental chamber maintained at room temperature. The two FBG sensors were externally attached to a Li-ion cell. The first FBG sensor was bonded at two points to the surface of the pouch cell with epoxy and the bonding lengths were approximately 1 cm. The second FBG sensor was loosely attached with heat conducting paste. The bonded FBG was sensitive to both strain and temperature changes, while the loosely attached FBG sensor was strain independent and was used as reference sensor to compensate temperature variations and the strain due to thermal expansion of the cell. The reflected wavelength peaks of the FBG sensors were monitored by a National Instruments (NI) PXIe-4844 optical sensor interrogator (OSI). The OSI was used to monitor the reflected wavelength peak of the FBG sensors. The OSI consists of a tunable laser which is sweeping across the wavelength range and a photo

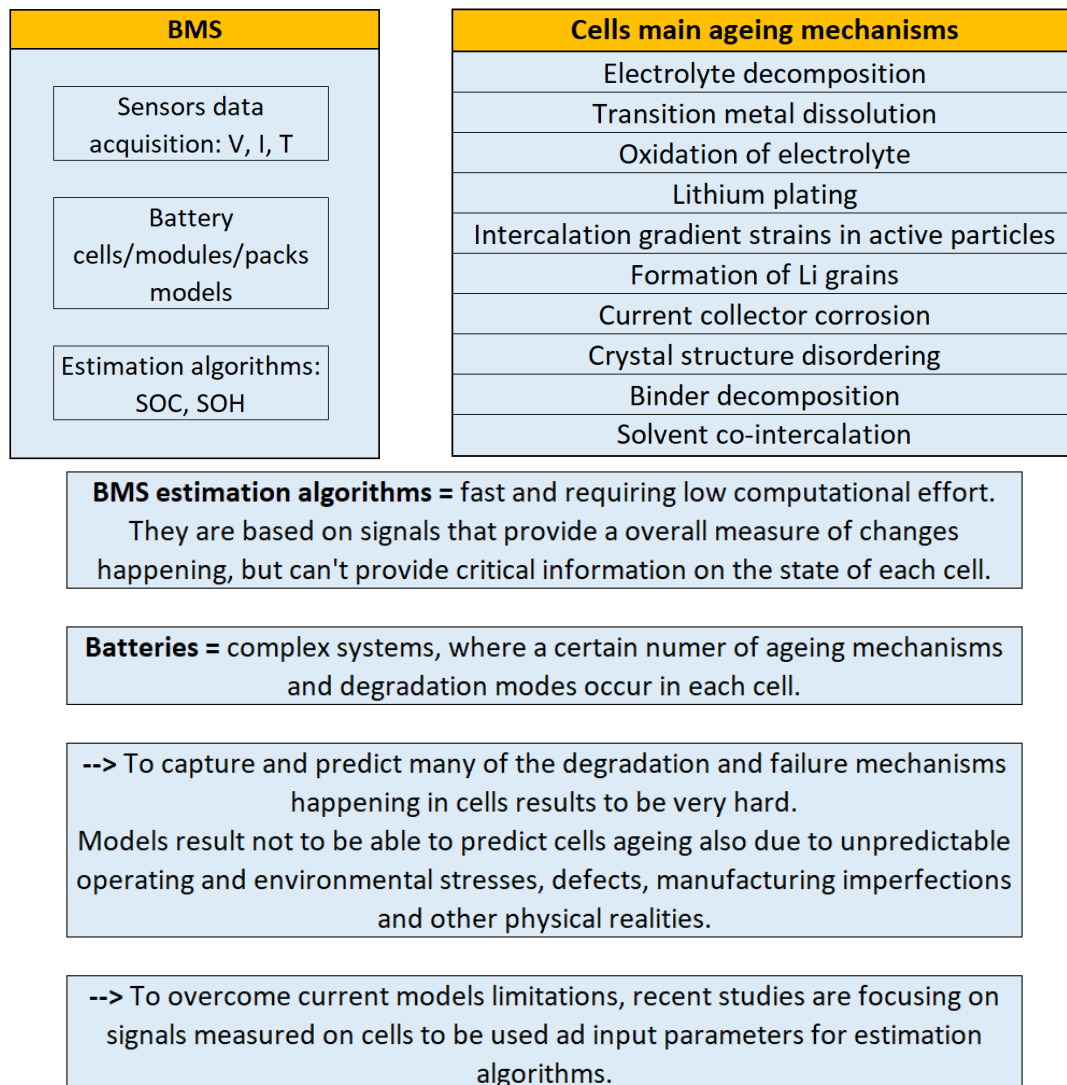


FIGURE 2.3: Main motivation supporting cells instrumentation.

detector which measures synchronously the reflected light. Once the wavelength of the laser matches the Bragg wavelength of the FBG, the photo detector monitors a corresponding response. The OSI detects peaks exceeding the set threshold intensity and assigns the peaks automatically to FBG sensors. The accuracy of the measured peak wavelength with the OSI is 1 pm. The cells explored in this study are LG Chem lithium ion pouch cell, with a nominal capacity of 15 Ah and an NMC/graphite chemistry. Analysis of signals from FBGs externally mounted on cells showed sharp features in the strain curve for charge and discharge that were repeatable across different C-rates. Sections with steep slope indicated as peaks in the corresponding derivative signals were assigned to phase transitions by correlating them to slow-discharge voltage measurements. These detectable intercalation stage transition points can guide cell analysis during design and characterization iterations, as well as for run-time monitoring in battery management systems to aid cell state estimation. The present study was limited to cell-level experiments in pouch cells. The results should be extensible to packs and modules where the pouch cells are packed in cans under pressure: the fiber-optic cables being hair-thin can be accommodated within existing commercial xEV module and pack designs, as well as embedded inside the electrode stack for direct internal electrode monitoring. Thus, this work demonstrated the potential of a FBGs, as a promising solution for monitoring additional cell parameters such as strain and temperature to aid state estimation in battery management systems [140].

In [103] it is presented a comparative study between the thermocouples and fiber sensors response for the monitoring of temperature variations occurring in three different locations of a lithium battery. The battery was submitted to constant current charge and different discharge rates, under normal and abusive operating conditions. In this work a commercial rechargeable Li-ion Polymer Battery (Iphone 5G Battery, Singapore) with maximum voltage of 4.3 V, nominal capacity of 1440 mAh and dimensions of 130 mm (length) \times 90 mm (width) \times 20 mm (height) was used. The temperature variations ΔT were monitored with three K-type commercial TCs (RS Pro) and three FBGs, all glued to the surface of the battery in three different positions (top, middle and bottom). The three FBGs (length of 3.0 mm), spaced by 40.0 mm, were written by the phase mask method in a commercial photosensitive single mode fiber (PS1250/1500, FiberCore). Typically, these sensors can operate from 0 °C up to 350 °C without damaging the sensor reflection signal. The TCs signals were acquired using a NI compactDAQ (NI cDAQ-9174, National Instruments) with a temperature module (NI 9211, National Instruments). The Bragg wavelength was monitored using an interrogation system (sm125-500, Micron Optics Inc., Atlanta, USA) with a sample rate of 2 Hz and a wavelength accuracy of 1 pm. The acquisition modules were controlled using a computer with a LabVIEW customized application, allowing the real-time monitoring of the acquired data. During all experiments, the battery was kept away from external heat sources, and the environmental temperature, monitored by a reference TC, was of 20.0 °C. In this work FBG and TC sensors were successfully coupled in order to monitor temperature

changes during testing at different discharge rates (0.53 C, 2.67 C and 8.25 C) and normal constant charge. Three different locations were monitored on the battery surface. For the higher discharge rate of 8.25 C, temperature variations of $(39.98 \pm 0.12)^\circ\text{C}$ were registered by the FBGs compared with the $(35.07 \pm 0.17)^\circ\text{C}$ registered by the TCs, on the top position. On the middle and bottom positions, the variations were of $(36.42 \pm 0.12)^\circ\text{C}$ and $(27.19 \pm 0.12)^\circ\text{C}$ for the FBGs and $(30.63 \pm 0.17)^\circ\text{C}$ and $(23.05 \pm 0.17)^\circ\text{C}$ for the TCs, respectively. For this specific application, the results showed that the fiber Bragg grating sensors have better resolution and a rise time 28.2% lower than the K-type thermocouples, making them a better choice for the real time monitoring of the battery surface temperature as well as a useful tool for failure detection and an optimized management in batteries [103].

2.4 Internal sensing

In [118], they used FBGs to instrument pouch cells for xEV applications. They used 15 Ah cells, with graphite anode and with a cathode material that is a blend of nickel-manganese oxide and manganese spinel. They first focused on the sealing method, in order to ensure a proper sealing of the pouch cell even in the region near the Fibre Optic (FO) entry point. A proper sealing is necessary to avoid moisture ingress into the cell but also to avoid electrolyte egress out of the cell. They used a protective heat seal film wrapped around the FO cable, between the pouch bag surfaces. The heat seal film material is the same material used on the tabs in the sealing region. A proper sealing is necessary to avoid moisture from entering the cell, that would produce HF that leads to cell degradation, and to prevent from electrolyte leakage, which would reduce the amount of electrolyte in the cell reducing the cell performance. To ensure a proper sealing, they carried out a seal integrity test, by manufacturing a pouch cell bag with an FO sensor, without any electrode inside, and by filling it with a known amount of electrolyte. The pouch bag was exposed to high temperature (60°C) and under high (95%) relative humidity conditions for a known period of time. Thus, these pouch bags were subjected to HF titration tests, that is a volumetric analysis, to examine the seal integrity under accelerated conditions. The tests results showed a volume of electrolyte comparable to that of a conventional sealed pouch bag without FO sensors. In their work [118] used FO characterized by a diameter of $125\ \mu\text{m}$ and $254\ \mu\text{m}$. They decided to manufacture multiple instrumented pouch cells so that every week they could open a different one and measure the amount of HF within the cell. This test allowed to show that pouch cells instrumented with $125\ \mu\text{m}$ diameter FO sensors developed an amount of HF very comparable with that of a conventional pouch cell, while the amount of HF was slightly higher but still comparable in the pouch cells instrumented with $254\ \mu\text{m}$ diameter FO sensors. In both cases, the results were below the maximum tolerable limit, that is 500 ppm/Ah/month thus the sealing procedure was successful. After the sealing procedure was defined, the next step was the definition of the FO sensor embedding procedure within the pouch cell stack. A portion of FO cable having at least one FBG sensor is placed

on one layer within the stack. The instrumented stack is then placed within the pouch casing layers and sealed with the conventional method, so that a portion of the FO cable including FBGs is within the pouch cell and the other portion is outside the cell and can be connected to the data acquisition system. The FO cable entry point is positioned approximately halfway between the positive and negative tabs but from the side opposite to that of the tabs and it was selected because it is considered a suitably informative position for sensing centrally inside the cell. Further attention must be paid during the sealing process due to the FO cable characteristics. In fact, the FO cable is very sensitive to bending as this can induce a noisy signal and in the worse case a FO cable damage if a small bending radius is applied, especially during the cell formation process, when gas are produced within the cell and the cell internal pressure increases. Thus, in order to minimize the FO cable bending near the sealing edge, attention is paid so that the distance between the level of the sealing point and the embedding level is as small as possible in order to reduce the stress on the FO cable. This is also the reason why the FO cable is placed in the middle layer of the stack, in order to avoid further curvature when exiting the pouch cell. The aim of [118] work is to monitor both temperature and strain during cycling, thus a FO cable with two FBGs is used so that one is used to monitor temperature and the other one is used to monitor strain. FBG sensors can also be used for current sensing as explained in [122], but [118] decided not to use FBG for this measurement as this technique is already well established in the literature and because the current measurement is already available from the battery cycler used during testing. The FO cable is bonded to the anode electrode using styrene-butadiene-rubber, that is a binder commonly used in Lithium-ion cells and used in the anode slurry of the pouch cells used within this work. After the FO cable was bonded on the anode, the electrodes were folded with the separator to get the instrumented stack. Thus the FBGs present on the FO cable can sense both temperature and strain changes. In a pouch cell, strain is due to electrode volume change over cycling and to thermal expansion or contraction of the electrode due to temperature variations. As an FBG sensor is sensitive to both temperature and strain, the two quantities must be decoupled. This is done following the procedure described in [122], thus one of the two FBGs, defined as reference FBG, is enclosed in a special tubing so that it is only sensitive to temperature. Then, the wavelength shift output of the reference FBG is subtracted to the wavelength shift output of the other FBG in order to compensate temperature variation on this second FBG. It is important to consider the expected output signal to verify that it is within the sensor specifications. The FBGs sensors wavelength shift output is linearly proportional to strain and temperature changes until the linear elastic material limits of the silica optical fibre or of its coating. In the case of acrylate coated optical fibre, that is a common fibre coating, the material linear elastic limit is between 2.5% and 4% [107]. In Lithium-ion cells, a 3% to 4% volume expansion and contraction is expected over the full depth of discharge cycle [136, 163]. As only the anode volume expansion is measured and accounting for the 35% volume fraction of the anode materials in the pouch cell

used in this work, an anode volume expansion up to 1.4% is expected over the full charge-discharge cycle, that is well within the linear elastic range of the FBGs. Thus the FBG sensor is expected to be suitable to accommodate the maximum anode strain at 100%. Similarly, considering the temperature output, silica fibres can work between -200 °C and 800 °C [87]. These temperature limits are far beyond the Lithium-ion cells operating and safety temperature limits thus the FO is suitable for temperature monitoring in the pouch cell. After the pouch cell instrumentation with FBGs for internal temperature and strain monitoring, [118] it was performed a stress test on both instrumented and not instrumented cells in order to compare the cell long service life and assess any performance variation. The cells, with a nominal capacity of 15 Ah, were cycled at 25 °C for 100 cycles at 1C charge and 2C discharge, and for 40 cycles at 2C charge and 2C discharge to increase the stress parameters. The results show that the degradation curves are very similar for both instrumented and not instrumented cells. The cells were then cycled at higher C-rates up to 5C/3 and while cycling they were cooled with the active thermal management system. The results show repeatable wavelength shift versus SOC curves across the different C-rates. This happens for discharging in the whole SOC range and during charging only in the constant current range. In the charging constant voltage range, the wavelength shift is no more representative of the SOC. [118] also compares the strain results obtained from internal and external sensing explaining that the spread in the strain curves at different C-rates obtained in the internal sensing configuration is much smaller than the spread obtained in the external sensing configuration [140], where the FO sensors were bonded on the cell pouch cell surface in the central location in order to monitor temperature and strain. This difference can be attributed to the much better thermal robustness and to the better temperature compensation of the FO strain sensor implemented in the internal sensing configuration. In fact in the internal configuration the FO sensor is bonded to the anode that is characterized by a much smaller thermal expansion coefficient than the pouch bag, thus it is less sensitive to temperature changes. Furthermore, the sensor is directly bonded on the anode where higher temperatures are developed during charging at high C-rates. On the contrary, in the external configuration the FO sensor is bonded to the pouch bag that has an higher thermal expansion coefficient and thus it is more sensitive to temperature variations at high C-rates and dynamic oscillations. Finally, the external FO is insulated from the actual internal electrode temperature by the separator layers and this, especially when high C-rate and aggressive dynamic cycles are applied, can bring to considerable temperature differences and can contribute to differences in the recovered strain curves at lower C rates where the temperature differentials are milder. After the test at constant 20 °C in the temperature-controlled chamber, [119] also performed the test at 45 °C and -10 °C. The results from these tests in terms of wavelength shift versus SOC curves are similar to the 20 °C test. After the cell level test, the instrumented pouch cells were connected in a 4-cells module with an actively cooled thermal management system (TMS) and they

were cycled in a module configuration at various C-rates and chamber temperature. The result of these tests consists again in a wavelength shift versus similar to the one obtained at cell level, however it is necessary to implement a machine learning algorithm such as dynamic time warping [11] for SOC estimation in order to let the two curves (obtained at cell level and at module level) overlap. The implemented algorithm yielded an average SOC estimation accuracy of better than 1% SOC and a worst-case error below 1%. After the static tests, the module was cycled with xEV dynamic cycles. The wavelength shift versus SOC curves obtained in dynamic cycling were overlapped to the curves obtained in static cycling with a general agreement between the two data sets, except for few regions. Thus the authors in [119] decided to move from the dynamic time warping to a better performing semi-empirical model to compute the SOC from the FO strain sensor output. The model is used together with an Extended Kalman filter (EKF) algorithm to estimate the SOC, as the process equation is linear in the states, but the measurement equation is nonlinear. The SOC estimation obtained from the EKF is then averages with the Coulomb counting SOC estimation.

In [118], they also estimated that the additional cell cost for embedding the FO sensor is expected to be within the 1 to 10 \$ range, including the added line equipment for the cells instrumentation procedure, taking into account the sensors price cost drop due to mass volume production and assuming to manufacture a number of xEV cells in the range of hundred thousands to a few million per year. Furthermore, as a module-level configuration, the fibres from each module can be consolidated into a single fibre passing through all the cells in one module. The cells from each module can in turn be monitored through a time-domain multiplexing by a single compact central optical readout collocated with the BMS. Finally, the data acquisition system cost, size and weight traditionally considered prohibitive for fielded deployments of FO sensing systems, can be overcome. In fact [78] developed a low-cost and compact wavelength detector suitable for FBGs. The overall system cost for a BMS with embedded FO sensors is projected to cost in the range of 100-500 \$ and thus it results to be comparable and competitive with the current cost of electrical sensing used in BMS. A final key advantage of FO sensors over electrical sensing is that the cost of FO sensing doesn't scale up linearly with the number of cells in a battery pack.

2.5 Scientific research trend

From the literature review on Li-ion cells monitoring, it results a growing interest on measuring additional quantities to the conventional voltage, current and point surface temperature already used in BMS. This is due to both the need to better understand what happens in a Li-ion cell in operating conditions and the need to provide further input to models and algorithms to estimate the state of the cell.

From the literature it is known that temperature is one of the main parameters influencing cells behaviour, performance and safety. When dealing with

External sensing	Internal sensing
✓ point sensing	✓ point sensing
✓ semi-distributed sensing	✓ semi-distributed sensing
✗ distributed sensing	✗ distributed sensing

FIGURE 2.4: Summary of topics studied in the literature.

temperature, it should be distinguished between temperature level and temperature gradients. Most of the studies in the literature focus on cells behaviour at high temperature level and at low temperature level and it is widely known that both these temperature levels are responsible for battery degradation that can be quantified in terms of capacity loss and resistance increase. Thus, the overall temperature level of the cell is of great importance. Concerning temperature gradients, it is known that especially if they occur over a wide temperature range and a large volume fraction of the cell, they provoke a battery degradation. Furthermore, temperature changes between two temperatures (thermal fatigue) can have a stronger impact than temperature gradients between the same two temperatures that are permanently in place [156]. This might be due to the fact that thermal expansion during temperature changes leads to increased mechanical degradation of the active material coating [155], however further studies are needed to clarify this degradation process due to temperature changes over time and space.

This leads to the importance of strain monitoring. In a cell strain is due not only to thermal expansion but also to Li-ions intercalation and to electrochemical failure mechanisms such as SEI growth, lithium plating, or gas formation as they all induce a volume expansion and therefore a mechanical stress. Results from the literature show that volume expansion increases with ageing, both in terms of reversible (over one cycle) and irreversible expansion. Furthermore, a direct correlation between the volume change and the capacity loss of a lithium-ion battery can be identified [159]. Therefore, strain monitoring is a useful tool for predicting the sudden cell death and might even serve as a diagnostic tool for the state-health, including safety aspects [159]. This topic is quite new to the literature and no specific studies on strain distribution have been published to date.

Various sensing options were investigated, and they can mainly be classified as: external vs internal sensing, and point vs distributed measurement, and all of them usually deal with temperature and/or strain measurements. A lack was found in the investigation of internal distributed temperature and strain measurements (Fig. 2.4), that is the main focus of this work.

The cell format selected for this study is the pouch format because it is of interest for xEVs applications and it is characterized by a cell surface that is large enough to investigate the distribution of measured quantities on it.

Chapter 3

Sensors

3.1 Sensors selection

As stated in the previous section, the main goal of this work is to perform a thermo-mechanical monitoring in-situ and in-operando in Li-ion cells in working conditions. In order to achieve this goal, a first fundamental step consists in the selection of the proper sensor type in order to be able to monitor distributed temperature and strain. Li-ion cells internal structure is characterized by a harsh environment because of the presence of electrolyte that is very corrosive. Battery cells are also very sensitive systems as their performance can be influenced by compositions changes, thus it is necessary to use sensors that are low invasive on the system. It is fundamental to avoid short circuits by creating an electrical connection between the anode and the cathode, thus electrical insulation is a fundamental specification as well. Because of the complexity of the system to be instrumented, a comparison among possible sensors is presented in order to select the most appropriate one for this type of application.

3.1.1 Sensors type classification

A first comparison can be made between electrical and optical sensors. In traditional electric sensors, such as foil strain gauges, thermocouples and RTDs, the DAQ system requires multiple wires per sensors, the sensors are sensitive to electromagnetic interference (EMI), and they are bulky with metallic wiring. On the contrary, fibre optic sensors are characterized by a DAQ system that doesn't need multiple wires as the sensors are multiplexed in the optical fibre, sensors are passive and chemically inert, lightweight and embeddable, they are characterized by high resolution (<1 mm), they can monitor many sensing points and are fast and easy to install [157]. A summary of this comparison is presented in Tab. 3.1. From this first comparison, fibre optic sensors result to be more suitable for this application, thus they were selected for further investigation.

3.1.2 Optical sensors classification

Once agreed to proceed using fibre optic sensors, a second selection is needed in order to identify the most suitable for this study. Optical sensor can

TABLE 3.1: Comparison between electrical and optical sensors.

Parameter	Electric sensor	Optical sensors
Electromagnetic interference	Sensitive	Immune
Electric conductivity	All wiring must be tightly insulated for applications outside or in water	Not conductive, no special attention required for use in water
Explosion risk	Hazardous in potentially explosive atmosphere	Safe in potentially explosive atmosphere
Weight	Weighty if the number of sensors is high (due of copper wiring)	Light-weight and limited wiring
Sensors installation and readout	Time consuming (to connect wiring). Operators with experience are required	Fast (<20 per sensor). Easy (can be done by not experts, no further wiring needed)
Measurable quantities	Temperature (thermocouples, thermistors), strain (strain gauges)	Lots of different quantities

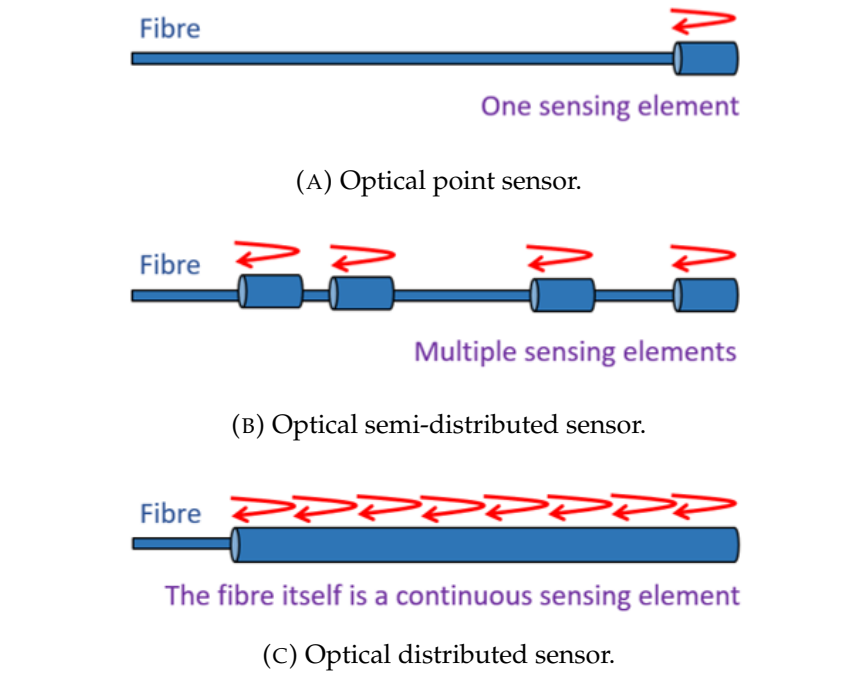


FIGURE 3.1: Optical sensors classification.

be based on various techniques. According to the technique, each sensor will be sensitive to various quantities, will have different sensing points, different resolution and sensing length. Optical sensors can be mainly classified as: point sensors, semi-distributed sensors and distributed sensors.

- In optical point sensors there is a single sensing element (Fig. 3.1a), thus only in the sensing element nearby quantities variations are observed. The main techniques used in optical point sensors are: Fabry-Perot, Mach-Zender, Michelson, Sagnac.
- In optical semi-distributed sensors there are multiple sensing elements (Fig. 3.1b) that are located along the fibre length according to pre-defined intervals. The main techniques used in optical semi-distributed sensors are: Fibre Bragg grating (FBG), Long period grating (LPG), Chirped fibre Bragg grating, Tilted fibre Bragg grating.
- In optical distributed sensors the fibre is itself a continuous sensing element (Fig. 3.1c), thus sensors are distributed along its whole length. The main techniques used in optical distributed sensors are: Rayleigh scattering, Brillouin scattering, Raman scattering.

As summarized in Tab. 3.2, each technique is characterized by different monitoring parameters, resolution and range. As in this work a short monitoring range is sufficient as the structure under test is characterized by small dimensions, in order to have a distributed measurement of both temperature and strain and to have a better resolution, Rayleigh (OFDR) based distributed fibre optic sensors were selected as the most suitable for the present application.

TABLE 3.2: Fibre optic sensors monitoring [57].

Sensing method	Sensors	Parameters ^a	Resolution ^b	Range ^c	Modulation method
Point	Fabry-Perot	Temperature / Strain	0.01% gauge length	10000 $\mu\epsilon$	Phase
Quasi distributed	FBG	Temperature / Strain	1-2 $\mu\epsilon$ /0.1 °C	5000 $\mu\epsilon$	Wavelength
Distributed	Rayleigh (OTDR)	Temperature / Strain	1 m/1 °C	2000 m	Intensity
Distributed	Rayleigh (OFDR)	Temperature / Strain	1 cm/0.1 °C	100 m	Frequency
Distributed	Brillouin (BOTDA)	Temperature / Strain	0.1 m/0.3 °C	1000 m	Frequency
Distributed	Raman	Temperature	1 °C	8000 m	Intensity

^a Can be configured to measure displacement, pressure, vibration, acceleration and acoustic.

^b Represents accuracy for point and quasi-distributed sensors and spatial resolution for distributed sensors, respectively.

^c Represents sensing distance for distributed sensors. Resolution deteriorates with increasing distance.

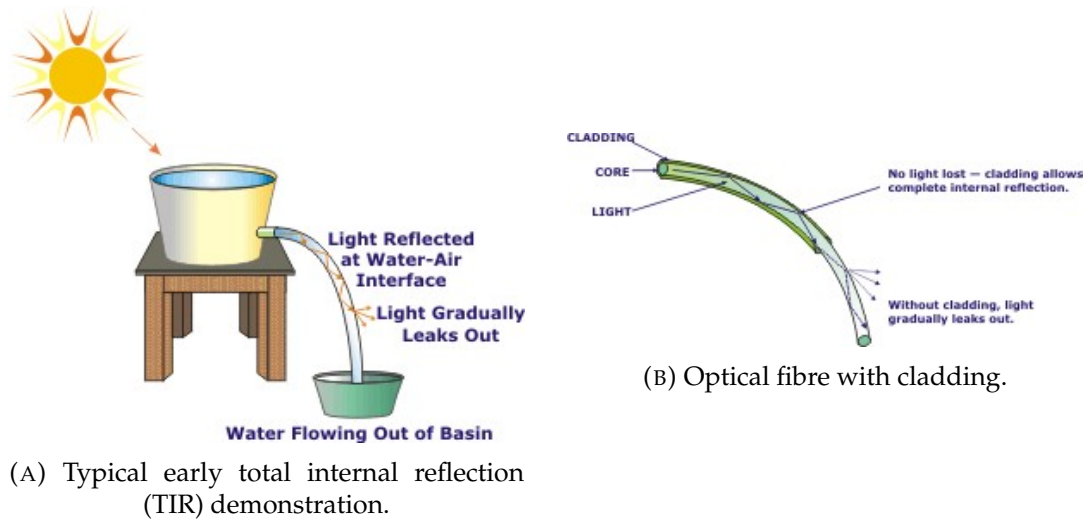


FIGURE 3.2: History of optical fibre [1].

3.2 Rayleigh (OFDR) based distributed fibre optic sensors

3.2.1 Fibre optic history

Guiding of light by refraction, the principle that makes fiber optics possible, was publicly demonstrated for the first time by John Tyndall in 1870. He used a jet of water flowing from one container to another and a beam of light to demonstrate the Total Internal Reflection (TIR) phenomenon. He used a container full of water with a spout in it. As water poured out through this spout, he directed a beam of sunlight at the path of the water. The light followed a zig-zag path inside the curved path of water (Fig. 3.2a) thus he showed that light follows a specific path. This experiment performed by Tyndall represents the first research into the guided transmission of light [1]. The fibre optic technology experienced a high rate of progress during the 1950's, due to the development of the fibrescope, an image-transmitting device using all-glass fibres. Early all-glass fibres experienced large optical loss, and this loss of light signal through the fibre was limiting the transmission along long distances. This limitation motivated scientists that developed glass fibres with a separate glass coating that could reduce light signal loss. These improved glass fibres were characterized by an inner glass region, called core, that was used to transmit light, and by a glass external coating, called cladding, that prevented light leaking out of the core (Fig. 3.2b). This light signal leakage reduction can be explained by the Snell's Law, stating that the angle at which light is reflected depends on the refractive indices of the two materials (core and cladding). Thus if the cladding is characterized by a lower refractive index, with respect to the core, the light will be angled back into the core (Fig. 3.2b), preventing light loss [1].

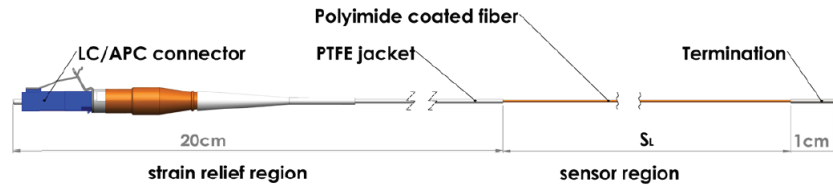


FIGURE 3.3: LUNA strain sensor scheme [134].



FIGURE 3.4: ODiSI-B measurement system. The ODiSI-B measures strain and temperature along the length of the fiber [90].

3.2.2 Data acquisition system

The sensors selected in this work are *LUNA* distributed fibre optic sensors. A schematic of a typical *LUNA* sensor is shown in Fig. 3.3 and the sensor specifications are summarized in Table 3.3. A sensor is characterized by a certain sensing region length and by two end points: one is the connector, that has to be connected to the data acquisition system, and one is the terminator. In the data processing, the sensor length increases going from the connector towards the terminator. The data acquisition system consists in the optical distributed sensors interrogator *LUNA* ODiSI-B (Fig. 3.4), that allows to acquire the signal from one sensor only. A fibre optic switch *LUNA* FOS 008 equipped with 8 channels, allows to connect up to 8 different sensors at the same time.

A scheme of the ODiSI-B working principle is summarized in the schematic in Fig. 3.5. The interrogator is based on frequency domain reflectometry. This technique was designed to measure reflected waves from circuits and components in fibre optics. This technique consists in the use of a laser that can be tuned to produce a beam of coherent light at a certain wavelength. This laser is used to generate a wavelength that sweeps a certain wavelength range (swept wavelength interferometry - SWI). This beam of light is used to scan a fibre optic, that is the sensor. Due to the Rayleigh scattering, that produces as results that light is diffused every time light is in contact with particles, light within the fibre is continuously diffused, in every point of the fibre. Waves

TABLE 3.3: LUNA Strain Sensor Specifications [134].

Parameter	Specification	Units
<i>Sensor Material</i>		
Fibre	Polyimide coated low bend loss fibre	
Connector	High Temperature LC/APC	
Strain Relief	PTFE (Teflon)	
Termination	304 Stainless Steel	
<i>Dimensions</i>		
Sensing Length	1, 2, 3, 5, 10, 20, 30, 50	m
Strain Relief Region Length	20	cm
Termination Length	1	cm
Sensor Diameter	155	μm
Termination Diameter	286	μm
Minimum Bend Radius	10	mm
<i>Performance</i>		
Maximum Operating Temperature Sensing Region	220	$^{\circ}\text{C}$
Minimum Operating Temperature Sensing Region	-40	$^{\circ}\text{C}$
Maximum Operating Temperature Connector	150	$^{\circ}\text{C}$
Minimum Operating Temperature Connector	-60	$^{\circ}\text{C}$

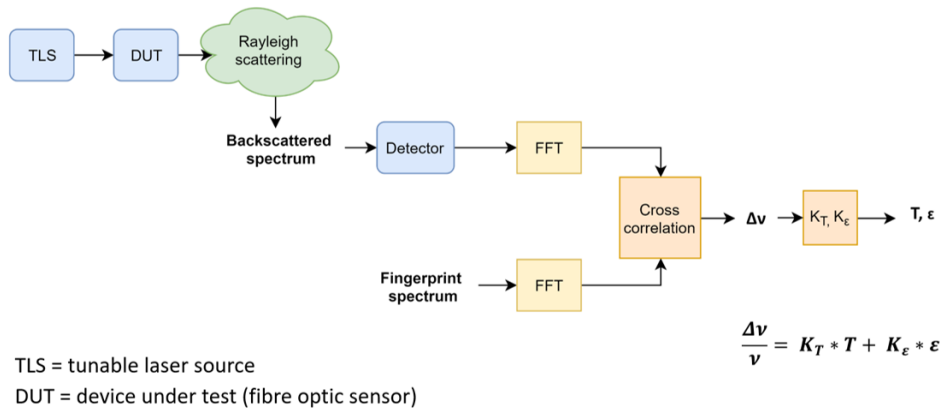


FIGURE 3.5: Rayleigh-based distributed optical fibre sensing working principle.

generated in this process in each point or the fibre interact each other and create an interference spectrum, called backscattered spectrum, that is received by a detector. Thanks to the technique that allows to sweep a certain range of frequencies, it is possible to correlate the backscattered spectrum with the locations along the fibre length. The optic fibre is intrinsically sensitive to temperature and strain variations, thus a variation in any of these quantities will produce a variation that can be quantified according to the variation in the backscattered spectrum. In order to be able to quantify the physical quantities variation, the backscattered spectrum is acquired in known conditions, and this acquired reference spectrum is called fingerprint spectrum. During a new acquisition, the cross correlation between this spectrum and a new spectrum is computed. This cross correlation allows to identify the variations occurred in the spectrum, that is a wavelength variation. This wavelength variation can be correlated with temperature and strain variation through the use of proper calibration coefficients. Finally, because a sensor is sensitive to both temperature and strain variations, it is necessary to decouple these contributions. Typically, a strain sensor is slid into a PTFE sleeve tube in which it can freely move, so that it becomes only sensitive to temperature variations. Finally, by subtracting the wavelength contributions coming from a strain and a temperature sensor it is possible to decouple these two signals.

The ODiSI-B can work at four different scan frequencies (Table 3.4), corresponding to different spatial resolutions.

3.2.3 Acquired signals

The data acquisition software consists in a *LUNA* proprietary software, that allows to manually switch from one port to the other of the FOS. However, as the test duration is long and it is necessary to continuously acquire the signal from the 8 channels, a software to automatically switch between

TABLE 3.4: ODiSI-B modes of operation [90].

Mode of operation	Maximum sensing length (m)	Acquisition rate (Hz)	Gage pitch (mm)	Gage length (mm)
Standard	10	100	2.61	5.22
High speed	2	250	2.61	5.22
High resolution	10	23.8	0.65	1.30
Extended length	20	50	2.61	5.22

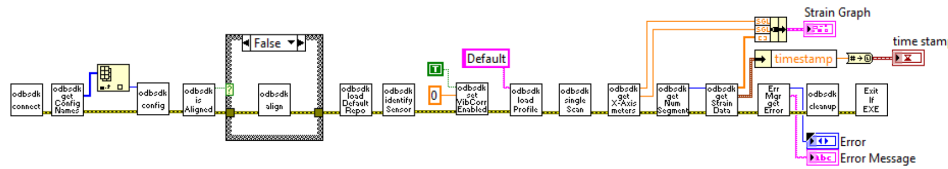


FIGURE 3.6: LabVIEW data acquisition program Block Diagram default functions [90].

the 8 ports was implemented in LabVIEW using the equipment communication functions provided (Fig. 3.6).

In order to start an acquisition it is necessary to select a certain operating mode, which means a certain scan frequency. When an acquisition starts, a certain number of scans will be logged in the data file, and the time between two consecutive scans depends on the scan frequency. Typically a number of 20 scans per channel is acquired every time, and this number was derived as a compromise between log data memory required and information acquired to be able to reduce the noise contribution. The acquired signal output file format is shown in Fig. 3.7. This output file is called “Processed” data file, because it is also possible to log data in a raw format that is only readable within the LUNA software environment and that requires a much larger memory. Thus data are usually logged in the Processed data file. The log file consists in a matrix where each column is a sensor gauge, thus it corresponds to a certain fibre location, and each row is a time instant, thus it corresponds to a different scan. The matrix contains the frequency shift in each sensor length location and for each scan.

As the test duration is long, it is necessary to reduce the data to the one of interest. Thus, a first step, usually consists in computing an average of the signal in the various scans. This can be done because the time interval between to scans is very low with respect to the observed phenomena, and this will help reducing the noise on the acquired signal. The acquired signal might also present some outliers that must be removed in order not to

Filename	\\endor\A-Team\temporary\datafile.txt					
First Column is Timestamp						
First Row is Location (m)						
Matrix is Strain (microstrain)						
-----	0	0.002614	0.005227	0.007841	0.010455	0.013068
2014-08-12T17:13:03.755794	2.08765	4.15394	3.54389	3.00304	1.25921	0.204553
2014-08-12T17:13:03.765789	1.46045	2.69927	1.44265	1.79435	1.2601	0.163225
2014-08-12T17:13:03.775784	4.24355	5.72183	3.80541	3.5637	2.6161	1.32038
2014-08-12T17:13:03.785777	3.03499	4.85323	4.18715	3.19642	2.12016	0.838889
2014-08-12T17:13:03.795772	0.820364	2.36942	1.53977	2.40057	0.965366	-0.13795
2014-08-12T17:13:03.805767	0.844993	4.52286	3.18605	2.9776	2.37473	1.92774
2014-08-12T17:13:03.815759	4.59216	5.46751	3.07043	3.33242	1.27408	0.917864

FIGURE 3.7: The formatting of the Processed Data File [90].

generate false indication of what is happening. Thus a check is performed both in time and space to verify that a certain frequency shift variation is an actual change. Also, it might happen that in a certain gauge location at a certain point in time, the signal quality might decrease below the quality threshold, for example because of an excessive vibration, and this will produce an unreadable point that results in a “NaN” in the Processed data file. Thus before computing an average in time, it is necessary to exclude the NaN points. However, it might also happen that a certain gauge is noisy in each of the scans logged. In this case, one or more gauge information will be missing and the signal will be interrupted in these points. This might be relevant if the interruption occurs in the sensing region of interest. In order to solve this problem, a signal reconstruction function is used, that allows to substitute the NaN points with frequency shift values derived by interpolation.

The data acquisition software implemented on LabVIEW, based on the functionality of the original LUNA software, will perform a loop among the number of active ports, that can be up to 8 because of hardware limitations, and for each port it will generate a Processed data file containing the frequency shift acquisition in each gauge location for a certain number of scans. After the interrogator scanned all the active ports, it will wait for the sampling period set to be completed, and it will start another lap. The LUNA functions don't allow to continue writing in the previous Processed data file, thus every time a new processed data file is created. This means that if the acquisition is performed on 8 channels and 1000 time iterations are performed, a total of 8000 Processed data files is generated. Because the data available is very large, it is fundamental to perform a preliminary data analysis to reduce the amount of data to the useful ones. In order to take into account these factors, the following data processing procedure has been derived and followed as a preliminary data analysis of each data set:

- *Step 1:* From the 20 scans acquired for each channel in each time instant, the average value is computed over the not NaN points, which means on all points whose signal quality is over the quality threshold. Thus

from a matrix of size $20 \times N$, where 20 is the number of scans and N is the number of gauges, a vector of size $1 \times N$ is obtained.

- *Step 2:* To delete outliers, the MATLAB Rlowess filtering is used. this is a robust linear regression over each window of A . It is more robust to outliers.
- *Step 3:* The NaN value is assigned to points that are characterized by a frequency shift value that is too much different from the expected value, that means it exceeds the temperature cutoff or the strain cutoff value, according to the sensor type.
- *Step 4:* The $N \times 1$ vectors obtained for a certain channel for each time instant. for a total of M time instants, are put together to build a matrix of size $M \times N$. Thus now this matrix contains the whole test duration information for a certain channel.
- *Step 5:* Check that the frequency shift difference between a certain gauge and the previous one and following one in space is not exceeding a certain threshold. Otherwise, in that point an average value is computed.
- *Step 6:* Check that the frequency shift difference between a certain gauge and the previous one and following one in time is not exceeding a certain threshold. Otherwise, in that point an average value is computed.
- *Step 7:* If a certain time acquisition is characterized by a number of NaN points that is over a certain limit, it means that acquisition is bad quality and not reliable, thus it is eliminated from the data set. This step will modify the matrix size from $M \times N$ to $M' \times N$ where M' can be different for each channel, according to the quality of the signal acquired.
- *Step 8:* The signal reconstruction is performed using the MATLAB Fillgaps function. This function will replace NaN points with values derived by interpolation.
- *Step 9:* Synchronize the temperature and sensors signals that are bonded on the same pouch cell by using the MATLAB Synchronize function. This is an interpolation method for the synchronize operation, specified as 'linear' for linear interpolation. This step will modify the matrix size from $M' \times N$ to $M'' \times N$ where M'' is the same for all channels that are acquiring the output signal from sensors bonded on the same system.

After this preliminary data analysis, the data set results to be much smaller in size and much easier to be read and further processed.

TABLE 3.5: Coefficients and Units.

Quantity	Unit
K_T	1 / °C
K_ϵ	-
k_T	°C / GHz
k_ϵ	$\mu\epsilon$ / GHz

3.3 Sensors calibration

As explained in Section 3.2.2, the ODiSI-B output is a frequency shift that must be correlated to the physical quantity through proper calibration coefficients (Tab. 3.5):

$$\text{Frequency shift (GHz)} \rightarrow k_t (\text{°C/GHz}) \rightarrow \text{Temperature (°C)} \quad (3.1)$$

$$\text{Frequency shift (GHz)} \rightarrow k_\epsilon (\mu\epsilon/\text{GHz}) \rightarrow \text{Strain } (\mu\epsilon) \quad (3.2)$$

LUNA sensors are already calibrated by the manufacturer, thus they are provided with both temperature and strain calibration coefficients using a linear and a quadratic regression respectively. However, it might happen to work with sensors from other manufacturers or to be using LUNA sensors and to be interested in computing the calibration coefficients using a different regression. In this situation, a calibration procedure must be implemented in order to correlate the frequency shift to the quantity variation. Here the calibration procedure implemented is explained.

To perform the DFOS calibration, a very simple setup was used (Fig. 3.8). It consists in a bar of high purity aluminum with a known thermal expansion coefficient. One strain sensor was bonded on a certain region of the aluminum bar using epoxy glue. Another region of the same sensor was put in a PTFE tube in order to avoid any strain on it and keep it only sensitive to temperature variations. Finally, two RTDs Pt100 Class A were bonded on the aluminum bar surface in known locations, identified through the *touch to locate* technique, in order to acquire the actual bar temperature. This technique consists in applying a localized heat to a certain point of the fibre, close to the RTD. A soldering iron tip heated up to about 150 °C is used to apply the localized heat to the fibre. As the whole fibre length is at room temperature and only a localized fibre segment is hot, this will rapidly produce a peak in the fibre output and the this peak can be easily identified with respect to the fibre end. This procedure allows to identify the fibre location close to the RTD, that is defined by a certain gauge number corresponding to a certain fibre length. Once the fibre sensor location corresponding to the RTD location has been defined, during the calibration procedure it will be possible to

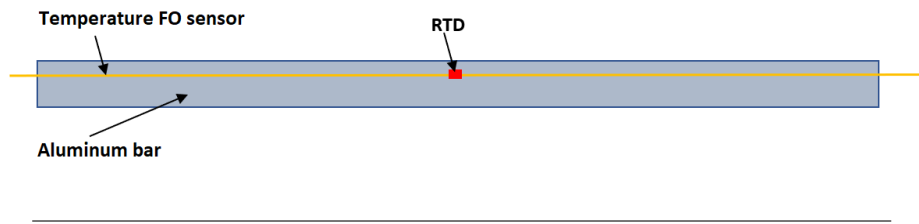


FIGURE 3.8: Calibration Setup.



(A) NI cDAQ 9174 chassis.



(B) NI 9217 RTDs data acquisition module.

FIGURE 3.9: NI RTDs data acquisition system.

directly compare these two values.

Thus the RTDs temperature output and the thermal expansions of the aluminum bar provide the reference temperature and strain values versus which the sensor frequency shift output signal can be calibrated. To perform the calibration test, the instrumented aluminum bar was placed in a thermal chamber and a temperature cycle was applied in order to induce temperature and volume changes on the aluminum bar. To define the temperature range of interest for the calibration test, it is important to take into account both the actual expected temperature and strain values to be acquired in actual operating conditions and the testing equipment temperature limits. In the current setup, together with the instrumented aluminum bar, also the NI cDAQ 9174 and the module NI 9217 to acquire the RTDs data and the Luna FOS 008 to acquire the DFOS data are placed in the thermal chamber. In Tab. 3.6 the operating temperature ranges of this equipment are summarized. From Tab. 3.6 it is clear that the minimum operating temperature is set by the Luna FOS 008 to 5 °C and the maximum operating temperature is set by the NI cDAQ 9174 to 55 °C. As the pouch cells tests were planned to be conducted at a chamber temperature in the range 10 °C to 40 °C, the pouch cells output is expected to be within the 5 °C to 55 °C calibration range. Thus, the defined setup results to be suitable for the identified temperature calibration range.

TABLE 3.6: Calibration equipment operating temperature limits.

Equipment	T_{min} (°C)	T_{max} (°C)
RTD Pt 100	-50	250
Polyimide coated strain DFOS sensing region	-40	220
Polyimide coated strain DFOS sensing region in PTFE (Teflon) sleeve tube	-40	220
DFOS connector	-60	150
ESPEC thermal chamber	-35	180
Luna FOS 008	5	70
NI cDAQ 9174	-20	55
NI 9217	-40	70

The temperature calibration procedure allows to compute the temperature calibration coefficients that allow to convert the frequency shift measurement into a temperature measurement. In a fibre optic temperature sensor:

$$\frac{\Delta\lambda}{\lambda} = -\frac{\Delta\nu}{\nu} = K_T\Delta T \quad (3.3)$$

$$\Delta T = -\frac{\Delta\nu}{\nu} \cdot \frac{1}{K_T} = -\frac{\bar{\lambda}}{cK_T}\Delta\nu = k_T\Delta\nu \quad (3.4)$$

thus:

$$k_T = -\frac{\bar{\lambda}}{cK_T} = -\frac{1}{\nu K_T} \quad (3.5)$$

where k_T is the conversion factor and K_T is the calibration constant. The calibration procedure consists of the following steps:

1. Use the *touch to locate* technique to localize the RTDs.
2. Place the aluminum bar in the climatic chamber.
3. Set the acquisition system in order to acquire:
 - temperature with RTD $\rightarrow T_{RTD}$ (°C)
 - frequency shift with FO sensor in the same point in which the RTD is located $\rightarrow \Delta\nu_T$ (GHz)
4. Set the chamber to various temperatures for a sufficiently long period of time: 5 °C, 15 °C, 25 °C, 35 °C, 45 °C, 55 °C (Fig. 3.10).
5. Fit the acquired stationary points on MATLAB with the desired type of regression (e.g. linear regression, quadratic regression).

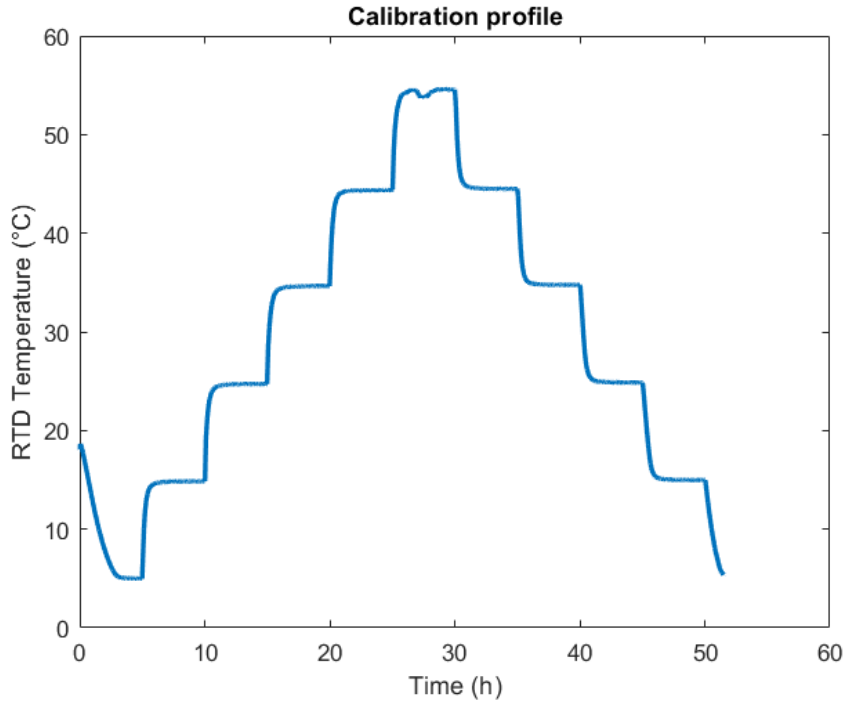


FIGURE 3.10: Climatic chamber temperature profile applied in the calibration procedure.

Linear fitting:

$$T = A_0 + A_1 * \Delta\nu_T \quad (3.6)$$

Quadratic fitting:

$$T = A_0 + A_1 * \Delta\nu_T + A_2 * \Delta\nu_T^2 \quad (3.7)$$

The coefficients obtained from the fitting procedure (A_0, A_1, A_2) can be used to convert the raw frequency shift into a temperature measurement.

The strain calibration procedure allows to compute the strain coefficients that allow to convert the frequency shift measurement into a strain measurement. In a fibre optic temperature sensor, sensitive to both temperature and strain, the procedure is very similar to the temperature sensor. However, a preliminary step is needed, and this is the signals decoupling. In fact, as for the temperature sensor, only the frequency shift due to strain must be correlated to the physical strain measurement. Thus the strain sensor acquired frequency shift first need to be modified in order to remove the temperature variation contribution. Knowing that:

$$\frac{\Delta\lambda}{\lambda} = -\frac{\Delta\nu}{\nu} = K_\epsilon \epsilon = K_\epsilon \epsilon_{TOT} = K_\epsilon \cdot (\epsilon_S + \epsilon_T) \quad (3.8)$$

Thus:

$$\epsilon_S = \epsilon_{TOT} - \epsilon_T \quad (3.9)$$

where:

$$\epsilon_{TOT} = k_\epsilon \cdot \Delta\nu_{TOT} \quad (3.10)$$

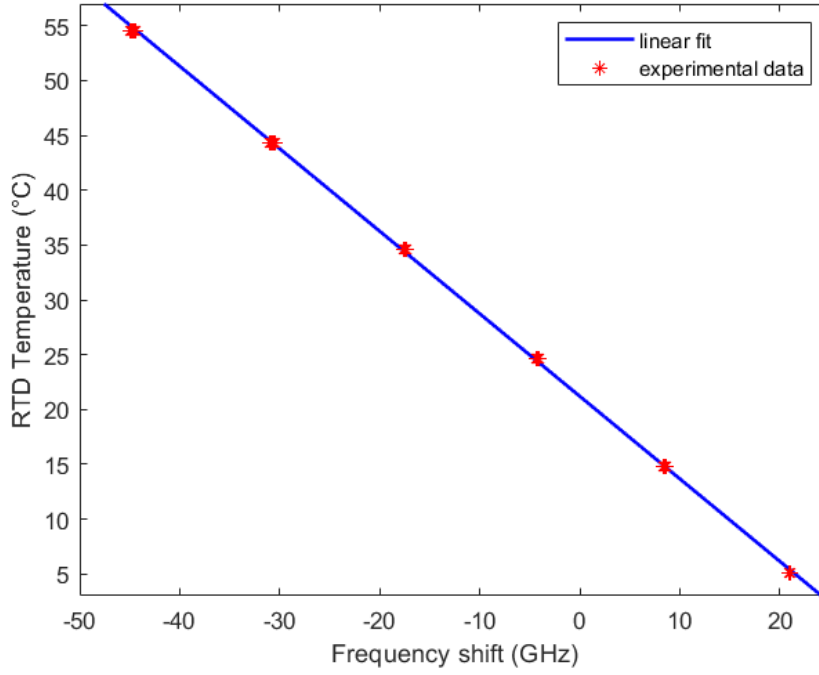


FIGURE 3.11: Temperature data fitting.

$$\varepsilon_T = k_\varepsilon \cdot \Delta\nu_T \quad (3.11)$$

so:

$$\varepsilon_S = k_\varepsilon \cdot \Delta\nu_{TOT} - k_\varepsilon \cdot \Delta\nu_T = k_\varepsilon \cdot (\Delta\nu_{TOT} - \Delta\nu_T) = k_\varepsilon \cdot \Delta\nu_S \quad (3.12)$$

$$\Delta\nu_S = \Delta\nu_{TOT} - \Delta\nu_T \quad (3.13)$$

where: $\Delta\nu_{TOT}$ is the output spectral shift in the strain sensor (GHz), $\Delta\nu_T$ is the output spectral shift in the temperature sensor (GHz) and $\Delta\nu_S$ is the decoupled spectral shift in the strain sensor (GHz), k_ε is the conversion factor and K_ε is the calibration constant.

In order to properly decouple the two signals, it is fundamental to know the correspondence between the temperature sensor and the strain sensor bonded regions. This can be done using the *touch to locate* technique to define the sensor location of interest. Then in the data post-processing, the sensor index corresponding to that locations are used to align the sensors and decouple the signals. The $\Delta\nu_S$ can be used in the data fitting and in order to compute the strain coefficients.

Linear fitting:

$$S = A_0 + A_1 * \Delta\nu_S \quad (3.14)$$

Quadratic fitting:

$$S = A_0 + A_1 * \Delta\nu_S + A_2 * \Delta\nu_S^2 \quad (3.15)$$

The coefficients obtained from the fitting procedure: A_0 , A_1 , A_2 can be used to convert the raw frequency shift into a strain measurement.

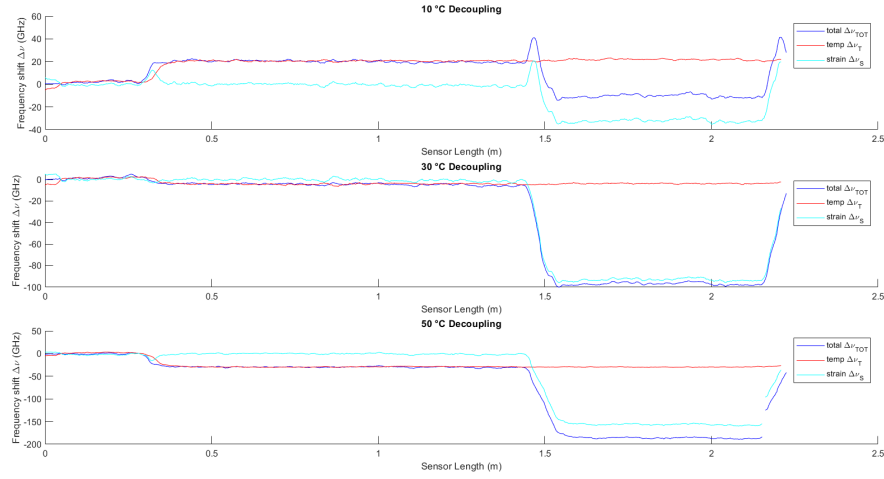


FIGURE 3.12: Calibration Signal Decoupling.

TABLE 3.7: Calibration coefficients.

Coefficient	Temperature	Strain
A_0	0.00000	0.00000
A_1	-0.68000	-6.67167
A_2	0.00000	-0.00005
A_3	0.00000	0.00000
A_4	0.00000	0.00000

3.4 Fibre optic sensors manufacturing process

As Rayleigh-based distributed fibre optic sensors use conventional single mode fibre optic cables it is possible to easily manufacture cheap sensors. It is only necessary to have a fusion splicer equipment in order to splice a connector, compatible with the interrogator connector) to the single mode fibre. In the present work, a *Fujikura 70S+* (Fig. 3.13) fusion splicer was used. In order to be able to splice two fibres together, the first step consists in removing the external coating that protects the silica core and cladding. To do so, various techniques can be used according to the coating material. For example, for polyimide coating three main different techniques can be used [47]:

- Thermal techniques: Polyimide can be oxidized under sufficiently intense heating, forming the basis of thermally removing the coating (e.g. open flame: matches and lighters tend to leave the glass brittle, thus this is a quick and easy method but it is not recommended if the strength of the stripped region is important).
- Chemical techniques: Due to the inert nature of polyimide, very hostile chemical environments are required to remove it. Great care should be exercised if these techniques are to be employed (e.g. sulphuric acid: the acid should be heated to approximately 100 °C, removing the polyimide very rapidly).
- Mechanical stripping: Although chemically bonded to the glass surface and much tougher to remove than an acrylate coating, with care the polyimide coating can be mechanically stripped (e.g. wire strippers: do not generally work, since the bond between the polyimide and the glass is so strong. The strippers will damage the glass in removing the polyimide).

The splicing procedure consists in:

- Remove the fibre coating (follow the right procedure according to the coating material).
- Clean the fibre with isopropyl alcohol (IPA) and wipes.
- Use the cleaving machine to cut the fibre end part with the right angle (90°).

Figs. 3.14 and 3.15 show the steps of the fusion splicing procedure: fibres are first loaded into the fusion splicer machine, then the two fibres end are aligned and finally they are fused together. Results are shown respectively for two identical fibres and for two different fibres. The two identical fibres are two original *LUNA* fibres: one fibre connector and one fibre cable; the two different fibres are one pigtail connector and one *Fibercore* fibre cable. During the fusion splicing process, the equipment will provide the information of the loss in the fusion point (Tab. 3.8). A low loss is an indication that



FIGURE 3.13: Fujikura 70S+ fusion splicer.

the fusion splicing process was performed properly, with a clean fibre and a good cleave angle. The important result is that the loss obtained from the splicing of two identical *LUNA* fibre sections is comparable with that of two different fibres. This second scenario is the most common one when someone is interested in manufacturing a distributed fibre optic sensor.

After splicing it is important to check the quality of the sensor output signal. This can be done using the distributed fibre optic interrogator. The signal quality results to be acceptable if, at least in the sensing region of interest but possibly along the whole fibre length, it is above the quality threshold, that is set by *LUNA* to a value of 0.38.

Before showing the results of the signal quality of the sliced fibre, it is fundamental to introduce another very important element influencing the signal quality, that is the terminator. As explained in the previous sections, the signal transmission inside the fibre optic is based on the total internal refraction principle. In order to have a good signal quality it is important that the signal loss are reduced and this is usually done by applying a protection element at the end of the fibre, that can be either a tiny metal tube, as in *LUNA* fibre optic sensors, or some index matching gel, as commonly done in fibre optic applications. The result of the signal quality comparison between a brand new *LUNA* sensor, equipped with a tiny metal tube and a *LUNA* sensor without terminator first, and then with the addition of index matching gel in the end tip of the fibre is presented in Fig. 3.16. The results show that a terminator, either a metal tube or index matching gel, is fundamental to have a signal quality that is over the quality threshold and thus produces readable results. As the metal tube is a *LUNA* design and it is much easier to singly apply some index matching gel on the tip of the fibre, the signal quality results that will be presented on the fusion spliced fibre have been obtained by applying some index matching gel on the fibre end tip.

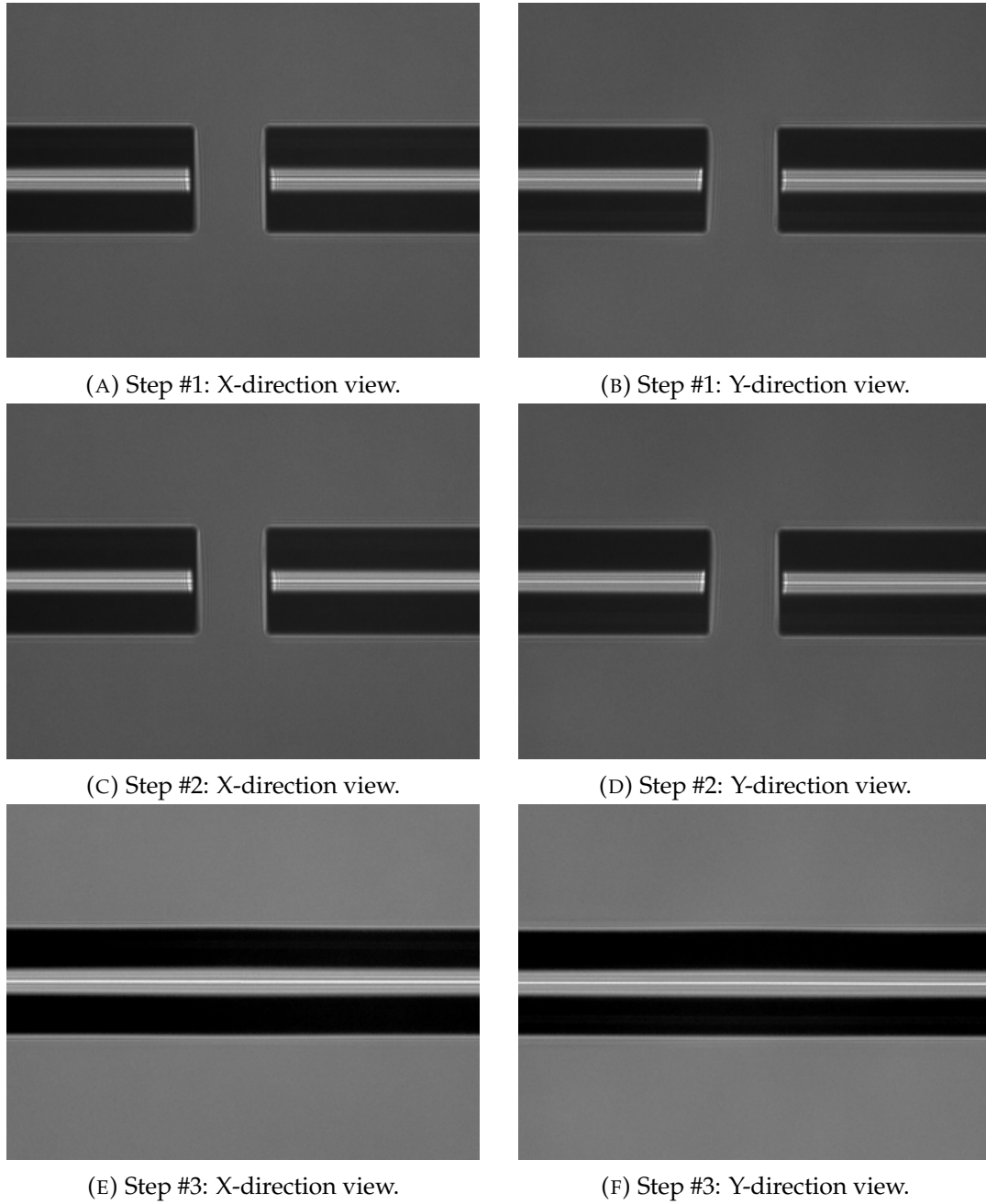


FIGURE 3.14: Fusion splicing using two identical fibres: A) - B) fibres before alignment; C) - D) fibres after alignment; E) - F) fibres after fusion splicing.

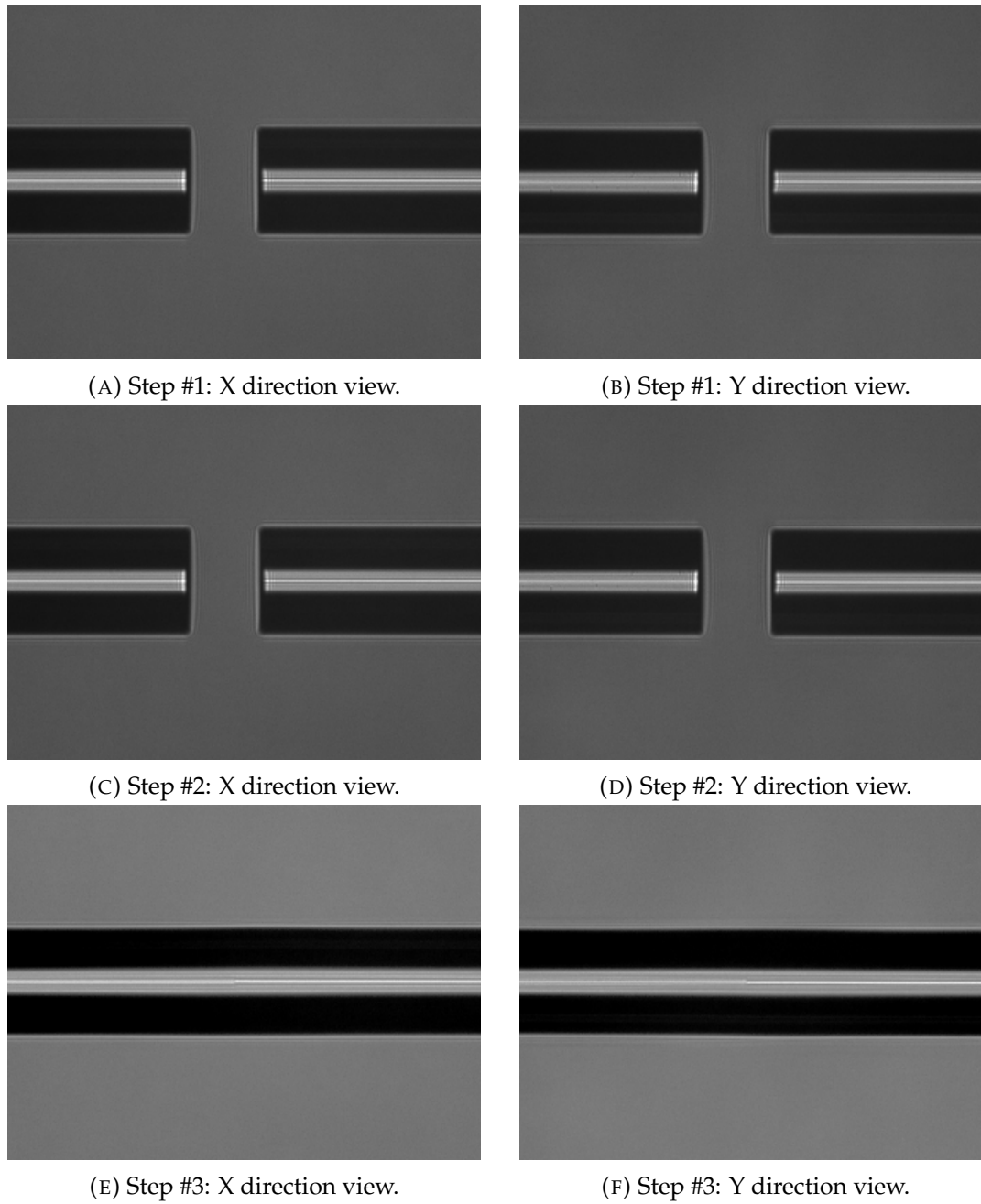


FIGURE 3.15: Fusion splicing using two different fibres: A) - B) fibres before alignment; C) - D) fibres after alignment; E) - F) fibres after fusion splicing.

TABLE 3.8: Fusion splicer output after fibre splicing.

	Same fibre	Different fibre
Memory No.	20	23
Fibre Type	SM	SM
Loss	0.01 dB	0.02 dB
Core Offset Pause	0.1 μm	0.2 μm
Core Offset Finish	0.1 μm	0.2 μm
Cladding Offset Pause	0.5 μm	0.7 μm
Cladding Offset Finish	0.3 μm	0.3 μm
Cleave Angle Left	1.5°	0.4°
Cleave Angle Right	0.8°	0.2°
Fibre Angle	0.4°	0.3°
Gap	16 μm	15 μm

Thus, after applying some index matching gel, the fusion spliced sensor output signal quality has been verified. Fig. 3.17 shows that the signal quality of the fusion spliced fibre is good along the whole fibre length. Fig. 3.17 also shows the frequency shift output signal. This signal shows a very evident peak in the splicing point nearby, as a consequence of the strain applied to the fibre in that point. This however, doesn't produce any influence on the output signal after the splicing point. Two main questions might rise from this figure. The first one is that the frequency shift peak corresponds to a sensor length that is shorter than the raw pigtail fibre. This is because the pigtail signal was acquired before the fusion splicing. Then, the splicing process implies that the sensor end has to be cleaned and cleaved and this implies

TABLE 3.9: Sliced sensors signal quality comparison.

Sensor	Mean	Variance
Luna Brand New sensor	0.8294	0.0034
Pigtail	0.9177	0.0026
Pigtail spliced with fibre	0.7879	0.0043

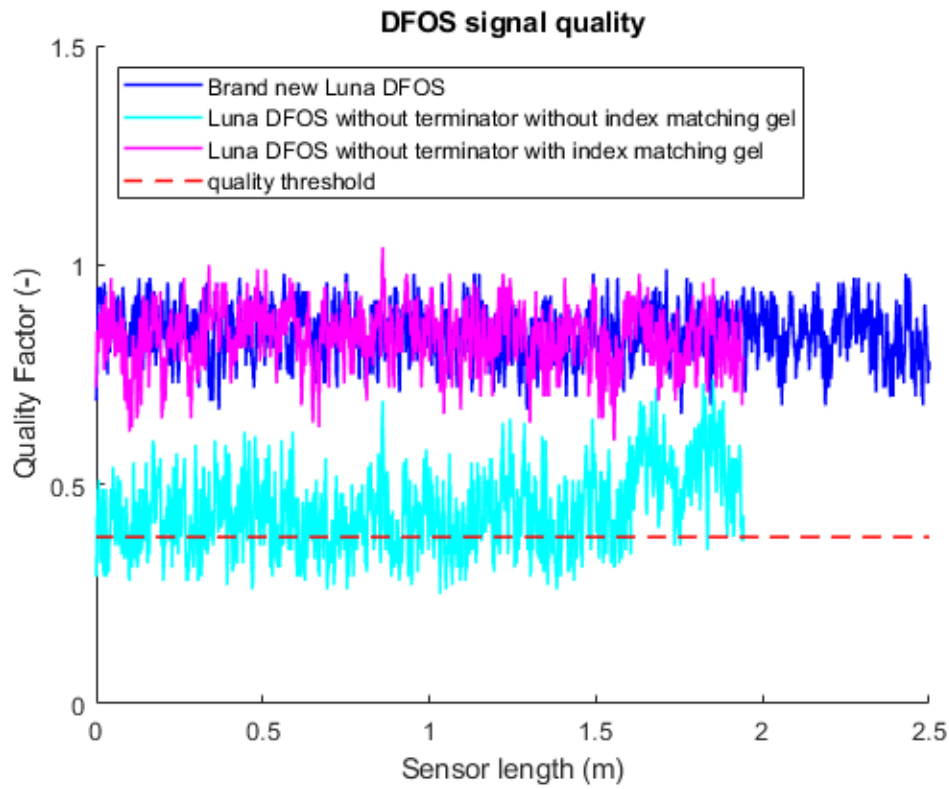


FIGURE 3.16: Terminator Quality Comparison.

that the fibre will be shortened. The second question might be that the frequency shift output is higher for the LUNA sensor than for the spliced fibre. This is due to both the facts that the fibre itself is different, thus it produces a different output when subjected to a certain stimulus (so it requires different calibration coefficients), and also because the signal was acquired in ambient temperature, that was slightly different in the two acquisitions.

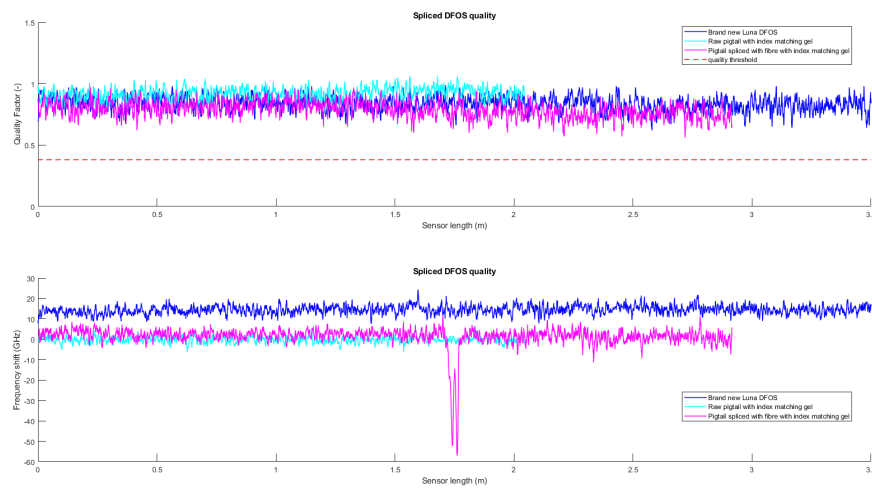


FIGURE 3.17: Splicing quality and frequency comparison.

Chapter 4

Pouch cells instrumentation

4.1 Pouch cells manufacturing process

As explained in Chapter 1, the main components of a pouch cell are: the positive and the negative electrodes, the separator and the electrolyte, and they are all enclosed in a pouch bag. In this section it is explained how these components are prepared and assembled to manufacture the final cell. All equipment used in the pouch cell manufacturing process are *Solith SOVEMA*. An overview of the manufacturing process using the pilot assembly line from *Solith SOVEMA* equipment is shown in Fig. 4.1.

Pouch cells used in this work were assembled by the author, while the current collectors coating procedure was conducted by other professionals on this topic, as to perform this process on large format electrodes (like the one used in this study) it is required particular experience as the process involves exposure with large quantity of hazardous materials. A summary of the battery cell manufacturing process is presented in Tab 4.1.

Coated current collectors are obtained starting from Aluminum and Copper foils (Fig. 4.2), for cathode and anode respectively, that represent the electrodes substrate. Then a slurry coating, different for anode and cathode, is spread over the substrate. The slurry is typically made up of various components:

- an active material, responsible for the electrode capacity;
- carbon black, to provide good conductivity to the electrode;
- a binder, to provide the slurry the ability to be bonded to the substrate;
- a solvent, to provide the slurry a certain viscosity.

The binder and the solvent mixed together are usually indicated as binder solution. Binder solution can be water based or NMP based. Water based binder solutions are made of styrene-butadiene rubber (SBR) and water-based solvent; N-methyl-2-pyrrolidone (NMP) based solutions are made of polyvinylidene difluoride (PVDF) and NMP-based solvent. Carbon black typically used is C₄₅ or C₆₅. The electrolyte composition is: salt (LiPF₆), solvent (a mixture of alkyl carbonates, such as ethylene carbonate (EC), propylene carbonate (PC), dimethyl carbonate (DMC) and diethyl carbonate (DEC)) and additives (Vinylidene Carbonate (VC)).

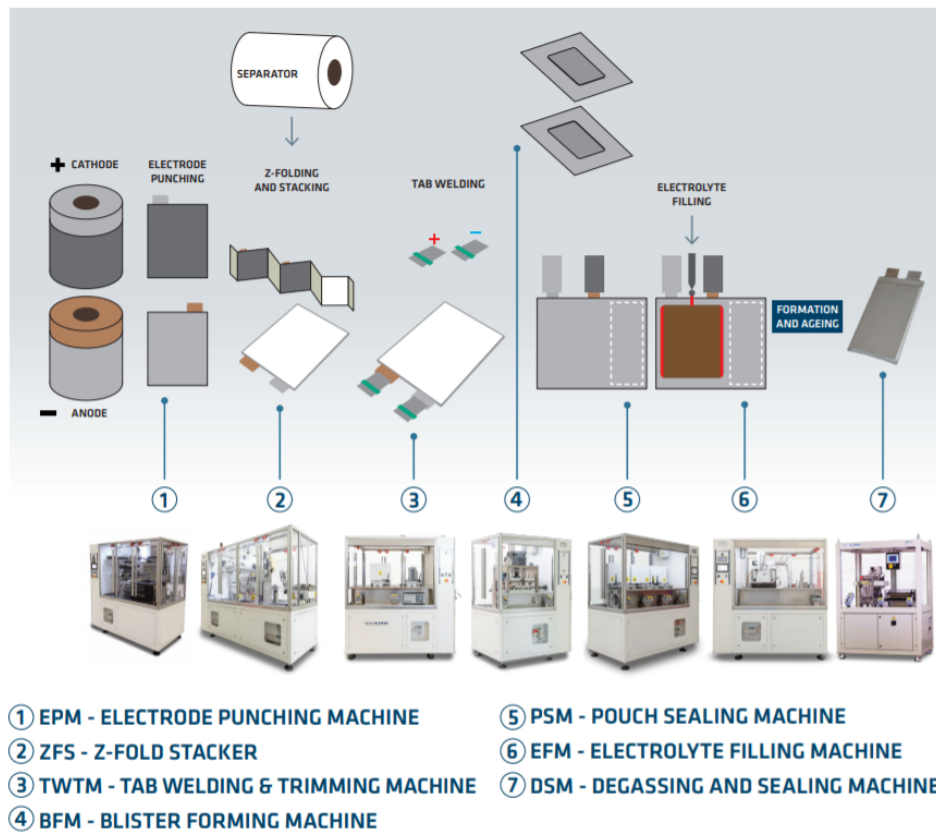


FIGURE 4.1: Pouch Li-ion cell pilot assembly line [141].

TABLE 4.1: Battery cell manufacturing process summary including material in- and outflow [9].

Manufacturing process		Material
Electrode Manufacturing	Slurry mixing	+Active material
		+Conductive agent
		+Solvents
		+Binder
	Coating	+Al/Cu foil
	Drying	-Solvents
Cell Assembly	Calendaring	
	Cutting	+Remaining Al/Cu foil
	Stacking/Winding	+Separator
		+Adhesive tape
		+Al/Cu tabs
	Packaging (pouch/case)	+Pouch foil/casing
	Temporary sealing	+Solvents
Formation	Drying	
	Filling	-Remaining Al/Cu foil
	Permanent seal	
	Formation	
	Cell testing	

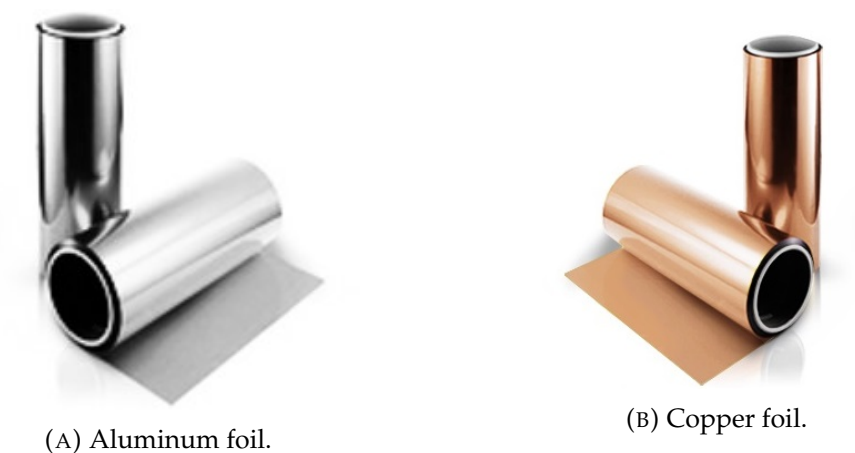


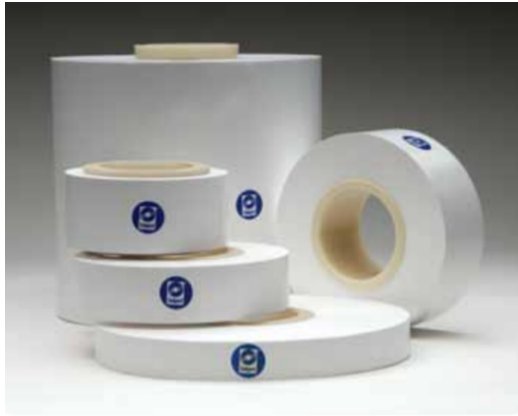
FIGURE 4.2: Positive and negative electrodes substrate.

The main difference between materials used in anode and cathode slurry is the active material. In anodes slurry the active material is typically graphite, while in cathodes slurry it is a mix of various metals. In the cells used in this work, the anode active material is graphite and the cathode active material is Lithium Nickel Manganese Cobalt Oxide (LiNiMnCoO_2 - NMC). Electrodes used in this study are double-coated, which means that the slurry was applied on both sides of the current collector.

The whole assembly process was performed in a dry-room in order to limit the amount of moisture in the manufactured cell. Similarly, all components to be assembled in the cell, were kept in the dry-room for a sufficiently long time in order to reduce the amount of moisture as much as possible.

Coated current collectors were punched in order to get the electrodes size of about 130 mm x 185 mm suitable to manufacture A5 pouch cell format (about 150 mm x 210 mm). Two different punching machines were used for anodes and cathodes in order to both avoid materials contamination and because of different punching dimensions. In fact, the anodes surface is punched slightly larger than cathodes (about 1 mm per side), as conventional in electrodes design, in order to minimize lithium plating [5]. In fact, if more anode surface is available, lithium-ion can more easily diffuse in the electrode, rather than building a lithium metal deposit (lithium plating) on the anode surface, that involves anode degradation.

Punched A5 electrodes were assembled according to the z-folding technique typical of pouch cells. Also during stacking, the separator length is slightly larger than the anode in order to make sure it will be able to avoid any contact between electrodes present in the various layers. The separator composition is: porous polyolefin membranes (polyethylene (PE), polypropylene (PP) and their blends such as PE-PP and high-density polyethylene (HDPE)-ultrahigh molecular polyethylene (UHMWPE)) or Ceramic separator. Before stacking electrodes it is important to measure the average electrode thickness, as this can vary due to the manufacturing process variability, and it will influence the tension level to be applied to the separator during stacking, in order to prevent bending. To measure electrodes thickness, an electrode expansion



(A) High Performance Battery Separators [20].



(B) Aluminium Laminated Film for Pouch Cell Case [27].

FIGURE 4.3: Separator (A) and pouch bag film (B) rolls.

gauge is used. Another important parameter is the number of electrodes to be stacked, as this will influence the final stack thickness. The number of electrodes depends on the target capacity, and is always an odd number as the number on anodes is always one more than the number of cathodes. The result of the stacking process is called stack.

After stacking, the cell terminals are trimmed to the right length, so that tabs can be welded. Tabs are welded using ultrasonic welding, a technique that uses ultrasonic waves or vibration to generate dynamic shear stress between the contact regions of two surfaces. The friction between the moving contact surfaces will produce heat that will locally melt both materials, thus a joint formation will take place at the interface.

For what it concerns the pouch bag, it is originally a roll of plastic-coated aluminum foil, that must be shaped according to the required size (Fig. 4.3b).

It is usually initially cut to the rough final dimension, and then it is cold formed to create a certain thickness in order to be able to arrange the stack inside. The thickness can vary according to the stack thickness. Once the bag thickness has been defined, also the bag length and width are defined by trimming away the excess material. Now the stack can be placed in the pouch bag in order to be sealed. The sealing process is performed using a pair of plates that will apply pressure and heat to a certain region of the pouch bag, allowing its internal plastic layer to melt, and once cooled down the two pouch bag layers will be bonded each other. This procedure is performed for 3 of the 4 sides of the pouch bag. The last side is left open, as it will be used as the gate to introduce electrolyte in the cell.

The amount of electrolyte to be introduced depends on the cell expected capacity. As explained, in order to avoid lithium plating, the anode surface available in a cell is larger than the cathode surface. Also, the specific capacity of the anode active material (about 370 mAh/g) is usually larger than the cathode active material (about 160 mAh/g). As the final cell capacity is limited by the electrode that provides the less amount of capacity, in a cell the limiting electrode is the cathode and the final cell capacity will be almost

equal to the capacity provided by the cathode active material. Thus, according to the cathode active material specific capacity, the weight of the cathode coating material (computed as the difference between a coated foil and a not coated foil), the percentage of active material present in the slurry (that is the only material providing capacity to the electrode), and finally the number of cathodes in the stack, the cell expected capacity can be computed. Then, a quantity of electrolyte proportional to the cell capacity (ml/Ah or g/Ah) will be inserted in the pouch bag through the side left open. Electrolyte filling is performed in a chamber under vacuum and then the last bag side is sealed using hot pressurized plates. With respect to the three previous sides, where the sealing region is close to the stack location, the last side is sealed in the pouch bag border. In this way, an empty region will be available next to the stack. This region will be useful to collect gas produced during the formation process and it will be finally trimmed away after degassing. So, after the last sealing, the cell is completely sealed and can be moved outside the dry-room as no contamination with the internal substances of the cell is possible anymore. From now on it is important to avoid contact between the positive and the negative tabs, thus it is useful to add an insulating protection cap to at least one tab.

At this point the cell needs some rest to allow the electrolyte uniformly soak in the electrodes. After a certain soaking time, the cell is ready to be formed. A longer soaking time will allow a more uniform electrolyte distribution in electrodes and thus a more performing cell. At this stage, the cell terminal voltage will be approximately zero.

The formation process is the name given to the first charging and discharging cycles, as during these cycles the majority of the SEI layer will be formed. In order to have a stable and uniform SEI layer, it is important to use a low current during cycling. During this initial cycling, some gas might be produced from reactions happening, thus usually the test setup consists in using some plates to apply a small pressure on the stack region, to avoid delamination induced by the gas as thanks to the plates the gas will move towards the empty region on the pouch bag. After formation, the degassing is performed and to do so, again a chamber under vacuum is used. The equipment in the chamber will make some holes in the pouch bag to allow the gas exit the bag, and then hot pressurized plates will seal the pouch bag. This time the sealing will be performed close to the stack location, thus at the end of this step the final cell layout is obtained.

Before starting the actual testing and ageing, the cell capacity needs to be stabilized. In fact, because in the first cycles the SEI layer is formed, the actual cell capacity is not properly defined yet and it may vary from a cycle to another. It will usually take 3 to 5 charge-discharge cycles to get cells with a certain capacity that, in the same cycling conditions (i.e. mainly same current rate, temperature and ageing), will not vary. Now the cells are ready to be used for further testing.

4.2 External instrumentation procedure

External cells instrumentation is performed by using conventional pouch cells (Fig. 4.4a) and bonding both the fibre optic temperature and strain sensors on the cell surface. Li-ion NMC/graphite 5 Ah pouch cells were manufactured according to the conventional procedure. Then, the fibre optics are first placed in the desired location on the cell surface and then bonded using tape (Fig. 4.4b). This procedure is repeated twice, once for the temperature sensor and once for the strain sensor. Then, in order to obtain a clean result, the region around the fibres is bordered (Fig. 4.4c) and then the epoxy adhesive is applied and let cured (Fig. 4.4d). In this work *Araldite* Fusion epoxy adhesive was used. As shown in Fig. 4.4, one sensor was bonded to multiple regions of the pouch cell. After the fibre has been firmly bonded to the pouch cell surface it is important to identify the sensor length of each bonded segment and the corresponding location with respect to the sensor starting point (i.e. close to the connector) in order to be able to properly process the acquired data. Thus, as explained for the calibration process, the *touch to locate* technique is used. Using the soldering iron tip, some localized heat is applied to the start and the end of each segment, and the corresponding sensor length is noted down. In the external instrumentation layout, each segment is about 130 mm long, as the cell width. This procedure is performed twice, once for the temperature sensor and once for the strain sensor, and the two sensors segments length and location is identified.

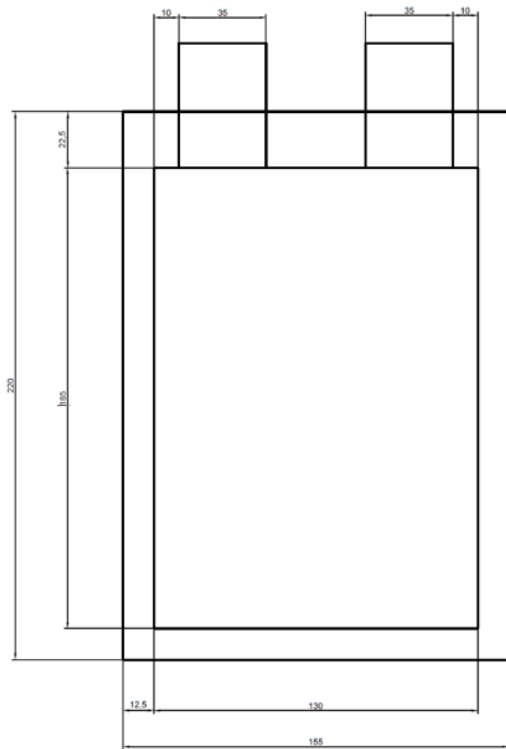
4.3 Internal instrumentation procedure

Internal cell instrumentation is a more complex task. In fact, it implies a modification of the pouch cell manufacturing process, in order to be able to properly place the temperature and strain fibre optic sensors inside the cell. Because of the higher complexity, a simpler sensors layout was selected with respect to the external sensing configuration, where sensors were bended and bonded on multiple regions of the same cell. Thus for the internal sensing the fibre optic sensors were placed straight from the tabs side to the bottom side, for the whole cell length of 185 mm. The final instrumentation procedure was defined as a consequence of a series of preliminary attempts and investigations. In the following sections, a description of the preliminary feasibility checks performed is presented, before the final implemented procedure.

4.3.1 Feasibility checks

Fibre optic sensor survival test in electrolyte

A first feasibility check consists in verifying that fibre optic exposure to the electrolyte will not cause any damage to the fibre external coating. In order to verify possible damage due to electrolyte contact, a portion of fibre was placed in a bottle filled with electrolyte and was left inside for some weeks. After few weeks the fibre surface was optically observed. To do so,



(A) A5 pouch cell format dimensions.



(B) Sensors bonded to the cell surface with tape.



(C) Bordered regions around the fibre.



(D) External instrumented cell.

FIGURE 4.4: External sensing instrumentation procedure.



FIGURE 4.5: ZEISS Sigma scanning electron microscope (SEM).

the fibre was first removed from the electrolyte and let dry. The fibre was first observed at the optical microscope, however for a clearer image, the observation was repeated at the SEM. The optical investigation was performed using the scanning electron microscope (SEM) ZEISS Sigma (Fig. 4.5). In order to be able to look at the fibre surface with the SEM, the investigated surface must be conductive. Because the fibre surface is polyimide that is not conductive, it is first necessary to deposit a thin platinum coating on the fibre surface and this was done using a *Cressington 208HR* sputter coater (Fig. 4.6). Results (Fig. 4.7) obtained using a ZEISS Sigma equipment showed no damage on the fibre coating surface, except for small scratches produced by fibre handling with tweezers. Thus obtained results showed no damage on the fibre optic coating due to the electrolyte exposure.

Fibre optic sensor survival test in the sealing region

Once verified the fibre coating was able to survive the aggressive electrolyte, a first version of instrumented cells was manufactured. In the very first version of the instrumented pouch cells, a temperature and a strain sensor were simply slid into a pouch cell stack. The stack was then sealed according to the conventional procedure. The immediate result of this process was a failure of the temperature sensor. In fact, even if the sleeve tube that is outside the fibre optics is made of PTFE that is a very performing polymer and is characterized by a high maximum operating temperature, because during the sealing process hot pressurized plates are used to seal the pouch bag, the polymer deflection temperature was exceeded, with the consequence of a PTFE tube melting on the fibre optics in the sealing region. This melted region (Fig. 4.8) involved the sensor to stop working. On the



FIGURE 4.6: Cressington 208HR sputter coater.

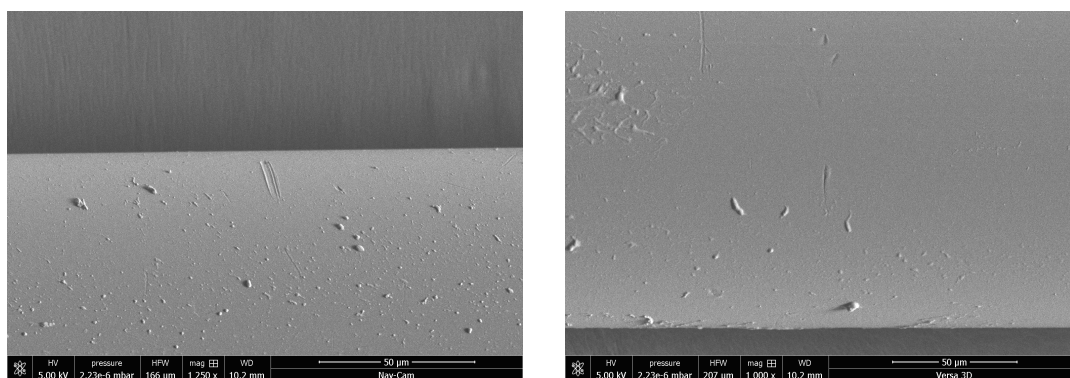


FIGURE 4.7: SEM observation results after electrolyte exposure.
Only small scratches on fibre coating surface are visible.

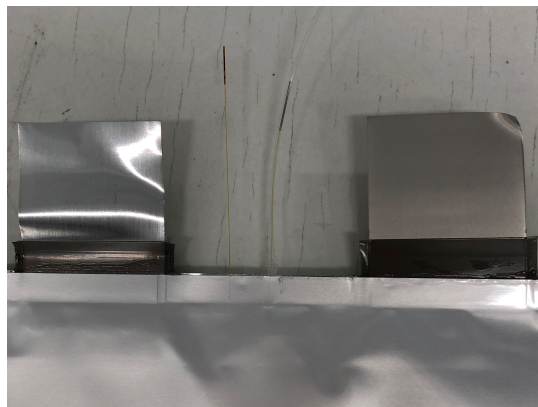


FIGURE 4.8: Melted PTFE tube in the sealing region.

contrary, the strain sensor output signal resulted to be very good, without any effect on the signal quality.

As a consequence of this result, an improvement was implemented by avoiding the presence of the PTFE tube in the sealing region. This result can be achieved by cutting the PTFE tube only for the length necessary to go across the whole pouch cell length, that is about 185 mm. Then, a strain sensor is used and it is slid into the PTFE tube. In fact, as already demonstrated in the calibration procedure, a strain sensor with an outer sleeve tube applied in a certain region will act exactly as a temperature sensor in that region. Thus, even if a strain sensor is used, this 185 mm region can be used to sense temperature in the pouch cell. After this first improvement, the instrumented cell design consists in the scheme represented in Fig. 4.9.

The instrumented cells manufacturing according to the current design was carried out proceeding with the next stages consisting in electrolyte filling and final sealing. After a certain soaking time, the instrumented cells were cycled to perform the formation cycle. Finally, the degassing and resealing was performed. Before starting the actual testing, the cells capacity need to be stabilized. It is known that, to get performing cells, the soaking time and the formation stage should be slow enough to allow a uniform electrolyte distribution in the stack and the formation of a stable SEI. Thus, because the sensors presence was already introducing some modifications to the cells normal behavior, in order to make sure to manufacture performing cells, the soaking time duration used was one week, and the formation was performed with a C/25 charging-discharging current. This ended up to take almost two weeks to complete the manufacturing process. At the end of this process, the sensors signal was acquired again. Unfortunately, after this time, the sensors ended up to be no more working. In fact the data acquisition system was no more able to identify the connected sensors, thus it was impossible to acquire any signal.

In order to investigate this damage, an optical observation was conducted. Three of the four pouch bag sides are sealed at 150 °C and 6 bar, except for the tabs side where sealing parameters consist of 160 °C and 9 bar. Cells tabs consist of a metal thin plate and a hot melting glue in the region that will

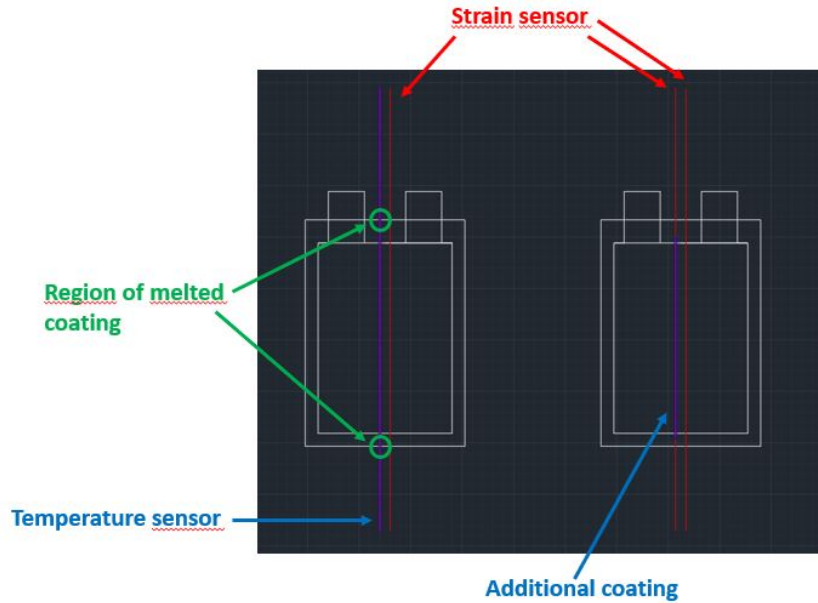


FIGURE 4.9: Temperature sensor vs strain sensor slid into a PTCE sleeve tube in the sensing region of interest in the pouch cell.

be placed in the pouch cell sealing region. When pressurized hot plates are used, both the tabs hot melting glue and the plastic inside the pouch bag will melt and the bag will be sealed. Thus, due to the tabs presence on this side, an higher temperature and pressure is applied in order to make sure the glue will melt and the bag will be properly sealed. Thus, the more aggressive sealing conditions happen of the tabs side. Optical observations show that when the fibre is sealed in the aluminum bag at 160 °C and 9 bar, the fibre coating results to be damaged. The fibre has first been observed at the optical microscope (Fig. 4.11) and then for a clearer image, the observation has been repeated at the SEM (Fig. 4.12). Again in order to be able to look at the fibre surface with the SEM, a thin film of conductive platinum was applied in order to coat the fibre surface. Fig. 4.12 clearly shows evident cracks on the fibre coating. This was considered to be the source of the fibre optic sensor damage. The crack involved the sensor to work as soon as it was exposed to the electrolyte, but it stopped working after some time because the electrolyte soaked up to the fibre glass cladding, damaging it.

Other possible solutions were considered, such as the adoption of fusion protection sleeves on the strain fibre in the sealing region. However, these resulted to damage the pouch bag (Fig. 4.10).

Partial sealing layout

Finally, in order not to damage the sensors during the sealing process, a partial sealing layout was adopted. This means that rather than simply sealing the pouch bag on the four sides, the sealing regions were split into sub-regions, in order to avoid having the sensors under the hot pressurized

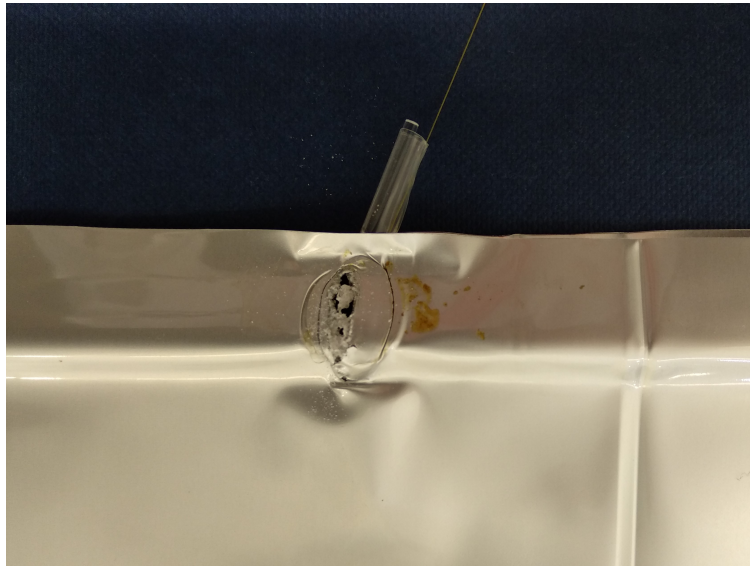
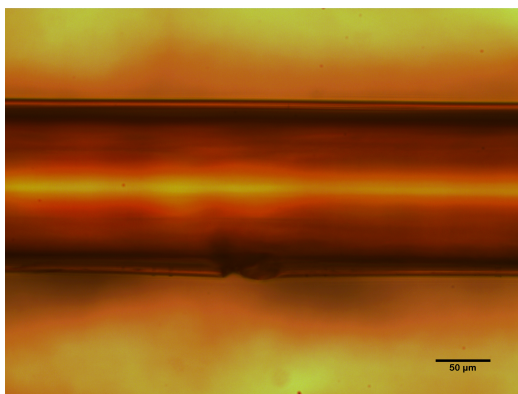
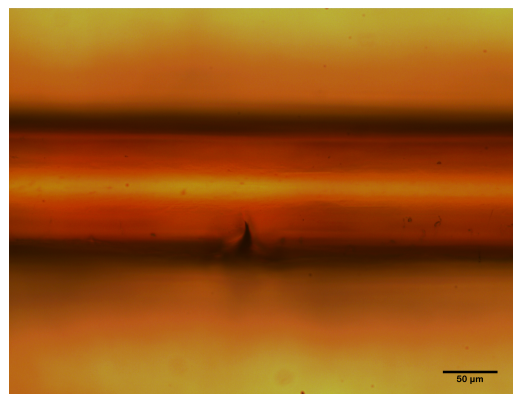


FIGURE 4.10: Pouch bag damaged by the fusion protection sleeve.

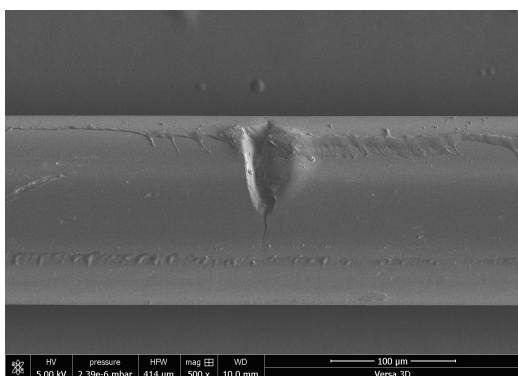


(A) Focus on coating borders.

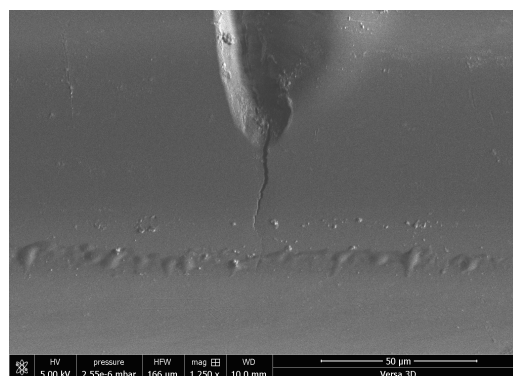


(B) Focus on coating crack.

FIGURE 4.11: Optical microscope observation of the fibre coating after sealing.



(A) Damage on fibre coating after sealing.



(B) Zoom on fibre coating crack.

FIGURE 4.12: Damage on fibre coating after sealing at 160 °C and 9 bar.

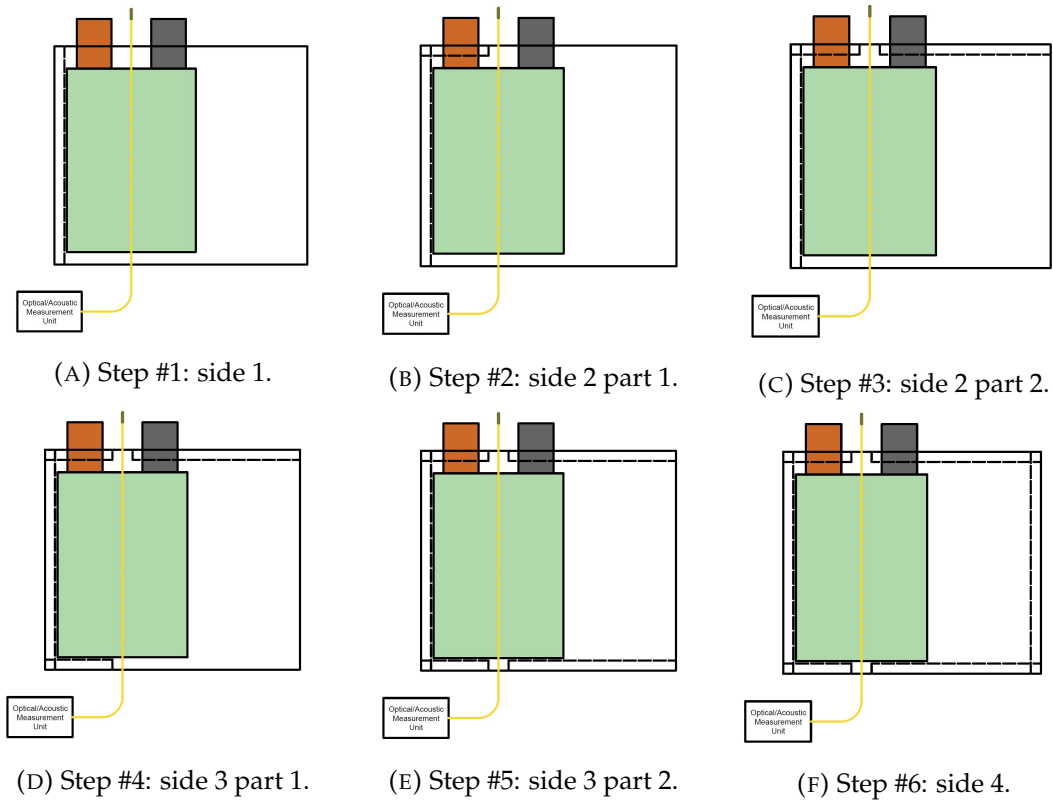


FIGURE 4.13: Procedure for pouch bag sealing with sensor.

sealing bars. Because in this layout the sensor in passing through the sealing region only on the tabs sides and on the opposite side, these two regions were split into sub-regions. In Fig. 4.13 the various steps of the sealing procedure have been summarized. This sealing procedure allows to avoid damaging the optic sensors with the sealing bars.

Using a partially sealed bag means an alternative way must be defined to seal the bag in the not sealed regions. The solution was found in the use of the *Permabond* ET514 glue, able to survive to the electrolyte. To verify this glue ability to seal the bag, a dummy partially sealed pouch bag was manufactured and was sealed with the glue. After 24 h, the pouch bag was filled with electrolyte. After 1 week there was no leakage from the glued regions, meaning the selected glue was suitable for this application.

Fibre optic sensor bonding on anode

Once the pouch bag sealing problem was solved, we can focus on the instrumented electrodes manufacturing. In fact, in order to be able to monitor strain on electrodes, the strain fibre optic sensor must be bonded to the electrode surface. In order to perform a low invasive operation, one electrode per pouch cell was instrumented, and the choice was to measure strain on the anode as, according to the literature [87], the highest volume change usually occurs in this location.

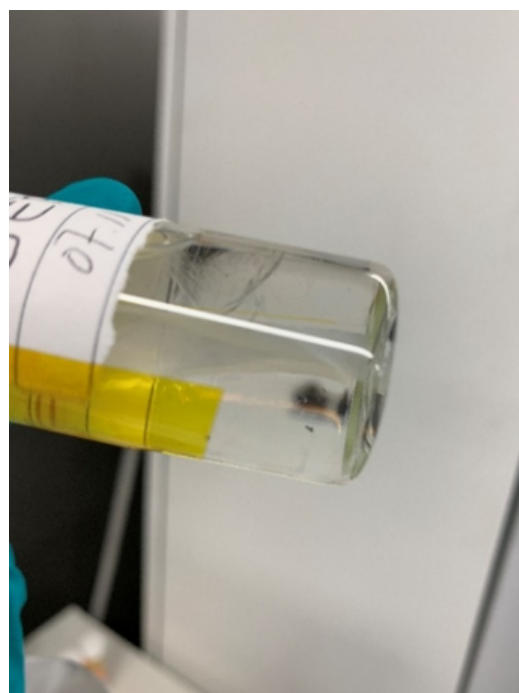
To find the best method to bond the strain fibre optic sensor on the anode

surface, a few different options were considered. A first attempt was done using epoxy glue. This material has been selected as it is commonly used to bond fibre optic sensors on the substrate. A small portion of sensor, about 80 mm long was bonded on the anode surface, as shown in Fig. 4.14a. After the glue was dry and cured, a smaller piece of anode was cut out of the large one and it was put in a small bottle full of electrolyte, as shown in Fig. 4.14b. The specimen was kept in the electrolyte for one week. After this test time, the epoxy glue resulted to be swollen and the sensor resulted to be no more bonded to the anode surface. Thus the epoxy glue resulted to be not suitable for this application. A second attempt was done using a binder solution made by SBR and water-based solvent. SBR is a binder commonly used in water based electrodes slurry, and it provides the sticky feature to the final slurry. This material has been selected because it is already used in Li-ion batteries and it successfully works as an adhesive. Again a portion of fibre was bonded on the anode surface and exposed to electrolyte as shown in Fig. 4.15. After one week of electrolyte exposure, the sensor was still bonded on the anode surface. After this successful attempt, a final material was selected and tested. As electrodes used in this work were made with NMP based binder solution, a binder solution made by PVDF and NMP-based solvent was selected as bonding material for this final attempt. In particular, rather than only using the binder solution, that is the sticky component of the electrode slurry, the complete slurry was used to bond the sensor on the surface. To do so, some anode slurry was manufactured and then spread on the anode surface to bond the sensor. Again, after the slurry was dry, the specimen was exposed to electrolyte and the bonding test resulted to be successful. Among the three methods, the last one using anode slurry was selected as the best one because it was able to keep the sensor bonded on the anode surface even after electrolyte exposure and at the same time it was the less invasive as it was using the same material composition that was already present in the anode. The anode slurry manufacturing procedure will be described more in details in the next section.

Because in order to perform this third test, new anode slurry was manufactured, some additional checks were performed to verify that the material structure was comparable to the original anode. Both the original anode coating and the new fibre optic sensor overcoating were observed at the SEM. The SEM electrodes images shown in Fig. 4.16 have been obtained with the following settings: EHT = 5 kV, Signal = SE2 (secondary electrons), WD (working distance) = 10 mm, Magnification = 800 X, while the SEM fibre images shown in Fig. 4.17 have been taken with a Magnification = 200 X. Fig. 4.16a shows the original anode coating manufactured with the conventional process by professionals on this topic. Fig. 4.16b shows the new anode that was manufactured in order to bond the fibre optic sensor on the anode surface. The comparison of the two images shows that the new manufactured anode slurry has a structure that is very similar to the original anode thus the anode slurry manufacturing process was successful. Fig. 4.17a and Fig. 4.17b respectively show the fibre bonded on the anode surface before electrolyte exposure and after electrolyte exposure. The comparison of the two images

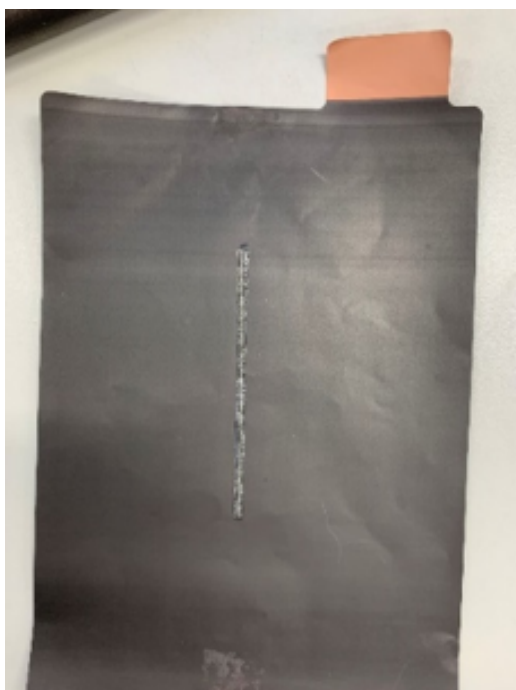


(A) Strain sensor bonded on anode using epoxy glue.

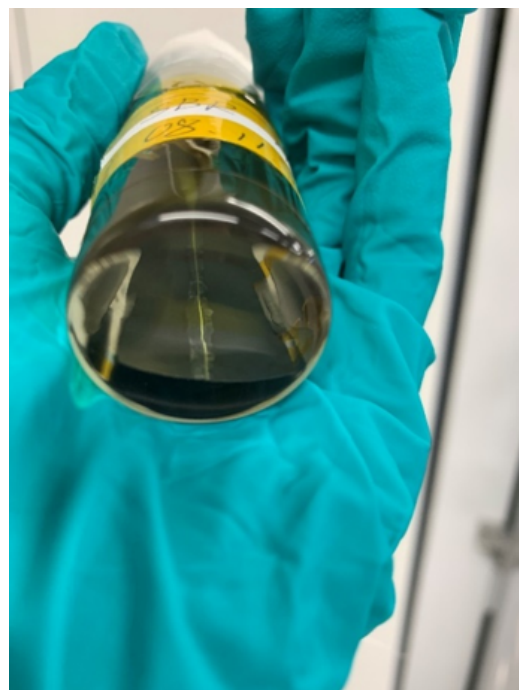


(B) Strain sensor bonded on anode using epoxy glue exposed to electrolyte.

FIGURE 4.14: First attempt to bond the strain sensor on the anode surface using epoxy glue.



(A) Strain sensor bonded on anode using SBR.



(B) Strain sensor bonded on anode using SBR exposed to electrolyte.

FIGURE 4.15: Second attempt to bond the strain sensor on the anode surface using SBR.

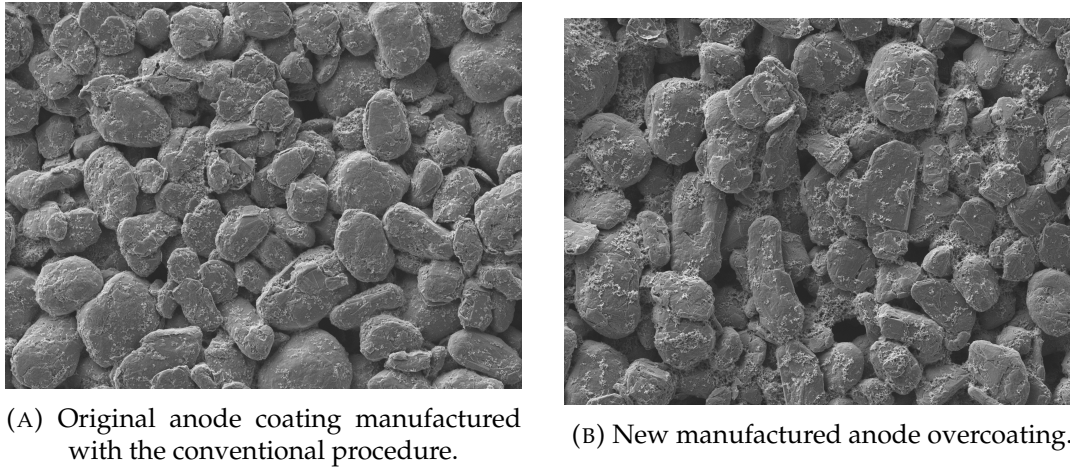


FIGURE 4.16: Comparison between anode original coating and new overcoating.

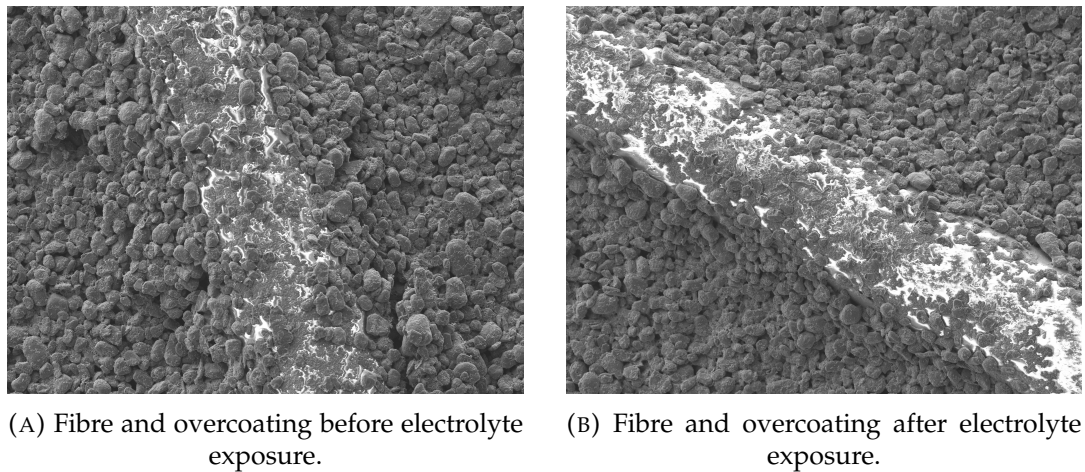


FIGURE 4.17: Comparison between fibre and overcoating before and after electrolyte exposure.

shows that after being exposed to electrolyte, the overcoating is still able to keep the fibre optic sensor bonded to the anode substrate.

4.3.2 Instrumented cells manufacturing process

Once the various manufacturing steps and corrections to be implemented were defined, it is possible to proceed to the actual manufacturing of the instrumented cells. As explained, for the bonding procedure it is necessary to use some new anode slurry, thus a first very important step consist in the anode slurry manufacturing.

The anode slurry preparation procedure can be summarized in the following steps:

- First of all you need to prepare the binder solution. In the current work, NMP-based binder solution was used. To prepare it you need 92% in weight of 1-methyl 2-pyrrolidinone (NMP) solvent and 8% in weight

TABLE 4.2: Anode slurry recipe components proportions.

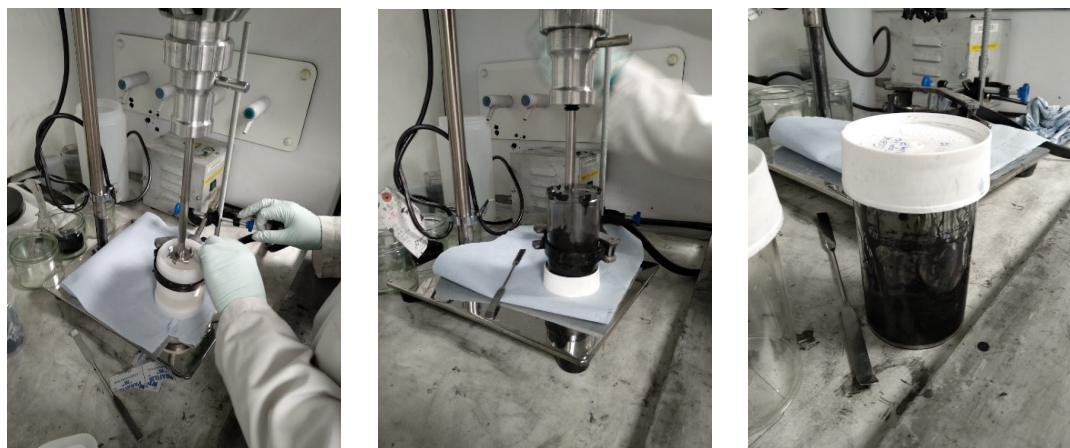
Component	State	Percentage	Amount
PVDF powder	solid	6% of 50 g	3 g
NMP solvent	liquid	69% of 50 g	34.5 g
Carbon black	solid	2% of 50 g	1 g
Oxalic acid	solid	0.17% of 50 g	0.085 g
Graphite	solid	91.83% of 50 g	45.915 g
NMP solvent	liquid	40% of 50 g	20 g
Total liquid content	liquid	52.15% of 104.5 g	54.5 g
Total solid content	solid	47.85% of 104.5 g	50 g
Total content	liquid+solid	100% of 104.5 g	104.5 g

of PVDF powder. You need to mix it with an high-speed mixer until you get a texture like a uniform gel, that means your binder solution is ready.

- Now you can start to prepare the slurry. Prepare 91.83% of natural graphite, 2% of Carbon black C₆₅, 0.17% of Oxalic Acid. All these components are powders so you can mix them together.
- Add you the powder the PVDF solution and additional NMP in order to get the right viscosity . It is important to always take note of the actual solid and liquid content you used during the preparation in order to eventually be able to adjust it to get a final slurry solid content of about 47%-51%. In fact, a rheology check (slurry viscosity) is important as it influences the slurry coating performance: if the slurry viscosity is too high, than the coating layer once dried will not stay flat, but it will bend; on the contrary if the slurry viscosity is too low it will not stay on the current collector and it will drain away.
- Again use a high-speed mixer to get a uniform slurry.

In the mixing process, sometimes vacuum can be used (if there is the presence of bubbles), especially towards the end of the mixing process. Sometimes, the slurry can be heated up and put under vacuum in order to get the right viscosity. The components proportions to prepare the anode slurry are summarized in Tab. 4.2.

This manufactured slurry can now be used to bond the fibre sensors on the anode surface. The sensors location was defined according to the scheme in Fig. 4.19. As shown in Fig. 4.20, the bonding procedure consists in apply-



(A) NMP solution mixing.

(B) Slurry mixing.

(C) Final slurry.

FIGURE 4.18: Slurry manufacturing procedure.

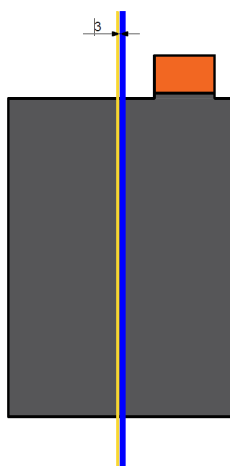


FIGURE 4.19: Instrumented anode scheme.

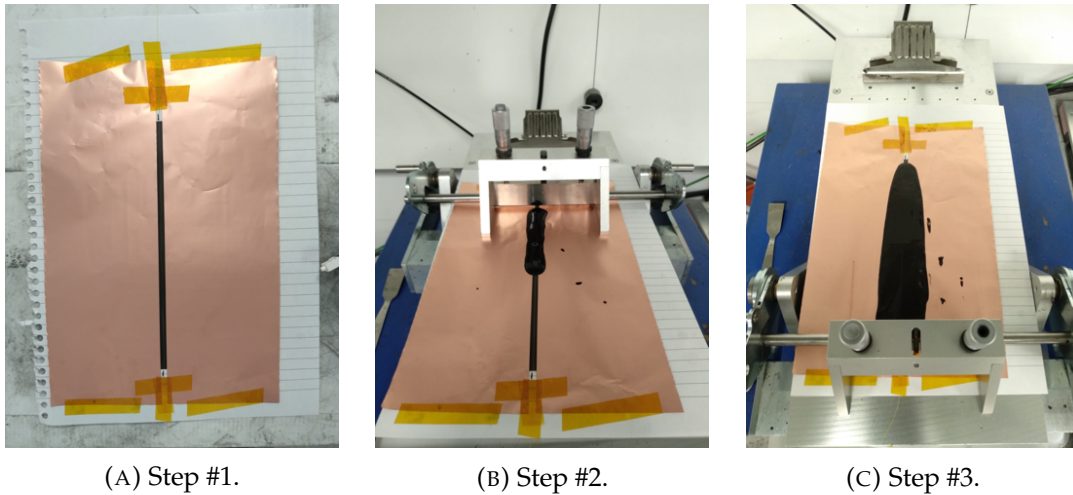


FIGURE 4.20: Procedure for sensor overcoating.

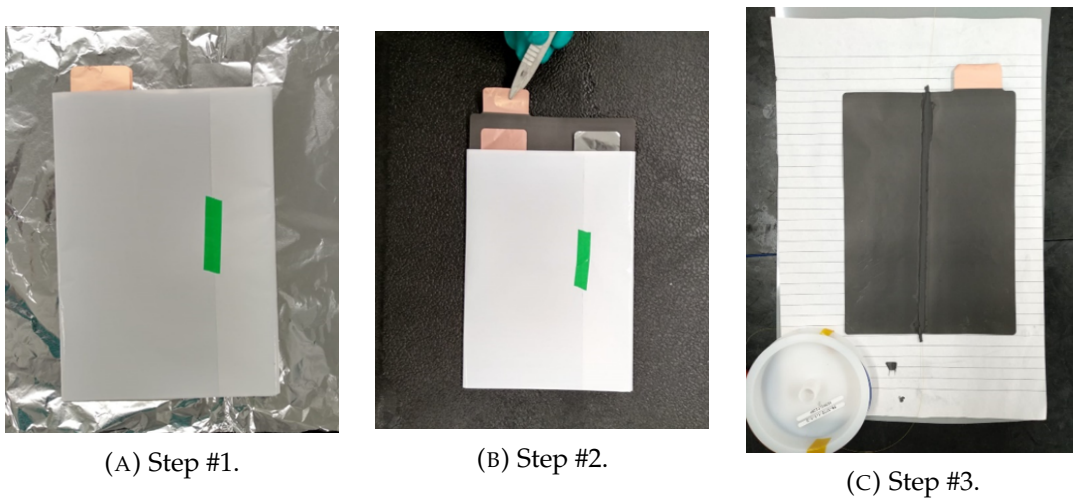


FIGURE 4.21: Procedure for conventional anode removal from the pouch stack.

ing some tape to hold in the sensor in position, then to apply some borders to limit the slurry to spread all over the anode surface and finally to use a coating machine to spread the slurry on the sensor. To let the NMP based slurry dry, it is necessary to use an hot plate set to 80 °C. It will take about 20 minutes to get it completely dry. Once the instrumented anode has been manufactured it can be used to replace a conventional anode in a pouch stack. Thus, as shown in Fig. 4.21, one conventional anode was extracted from a stack and it was replaced with an instrumented anode.

The result is a stack with one anode instrumented with a strain fibre optic sensor (Fig. 4.22). The stack will then go through the conventional tabs welding process (Fig. 4.23). After tabs welding, the temperature fibre optic sensor is slid inside the stack, close to the strain sensor. Then the stack is sealed in the pouch bag (Fig. 4.24) according to the defined procedure (Fig. 4.13) and the gates on the tabs side and the opposite side are sealed with glue. The glue is let cured for 24 h before performing the electrolyte filling (Fig. 4.25)

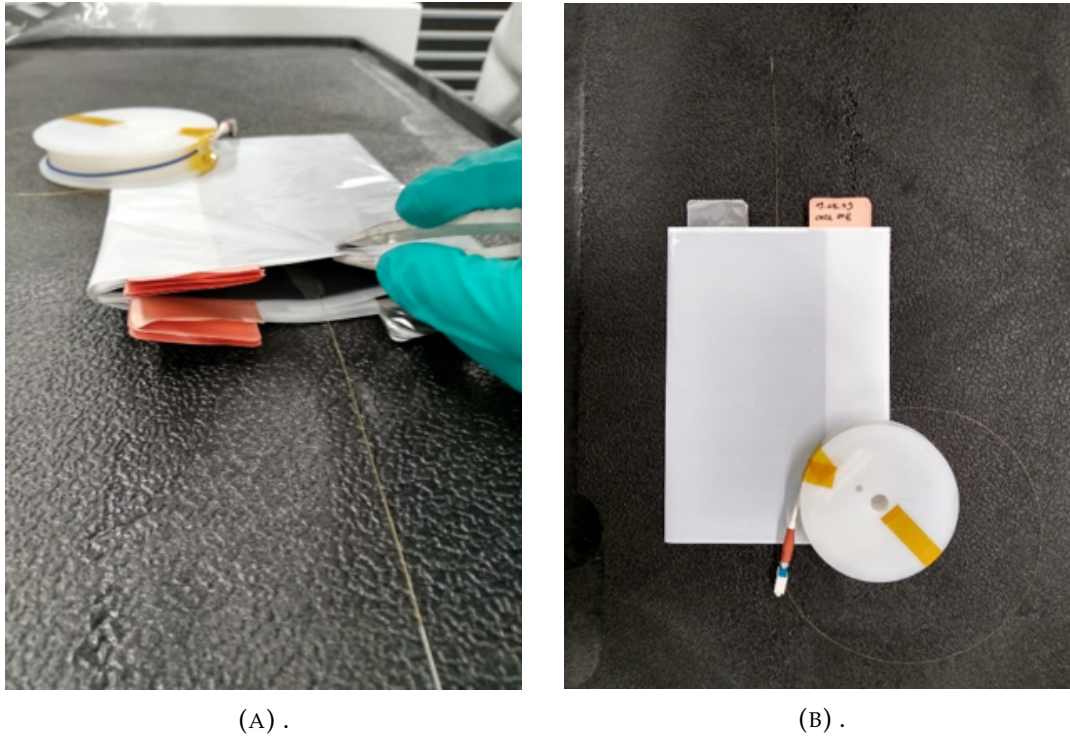


FIGURE 4.22: Procedure for instrumented anode insertion in pouch stack.

and the final sealing. Thus the instrumented cell manufacturing process is completed (Fig. 4.26).

As for the externally instrumented cells, also in this case after the cell was completed the *touch to locate* technique is used to identify the sensor region located in the pouch cell. Four instrumented cells were manufactured and results are summarized in Tab. 4.3. The manufactured cells were then placed in a properly designed test rig (Fig. 4.27). The test rig structure is made by plexiglass plates and brass connectors. It can be placed in the climatic chamber and be easily connected to the cells cycler. The cycler is the equipment used to apply user defined charging and discharging profiles and cycles to cells under test.

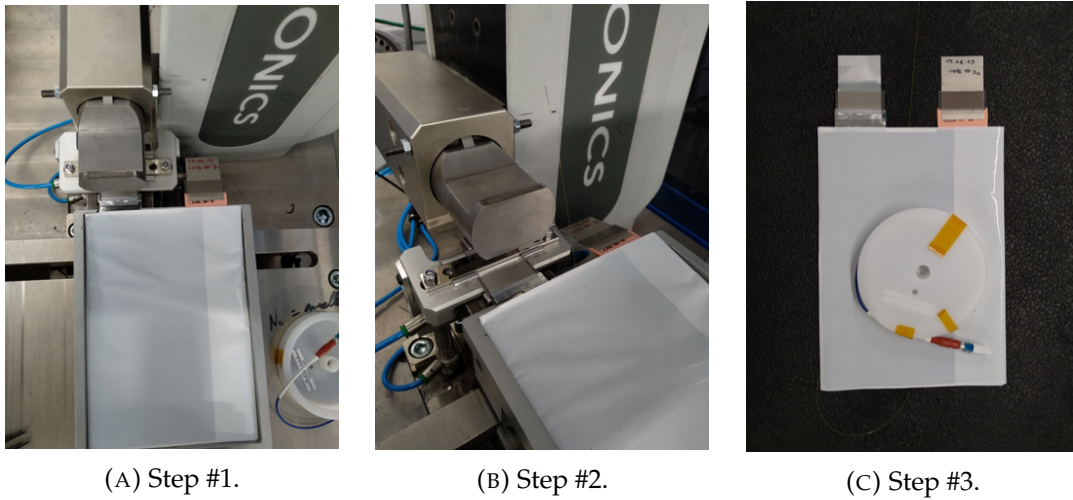


FIGURE 4.23: Instrumented pouch stack tabs welding.

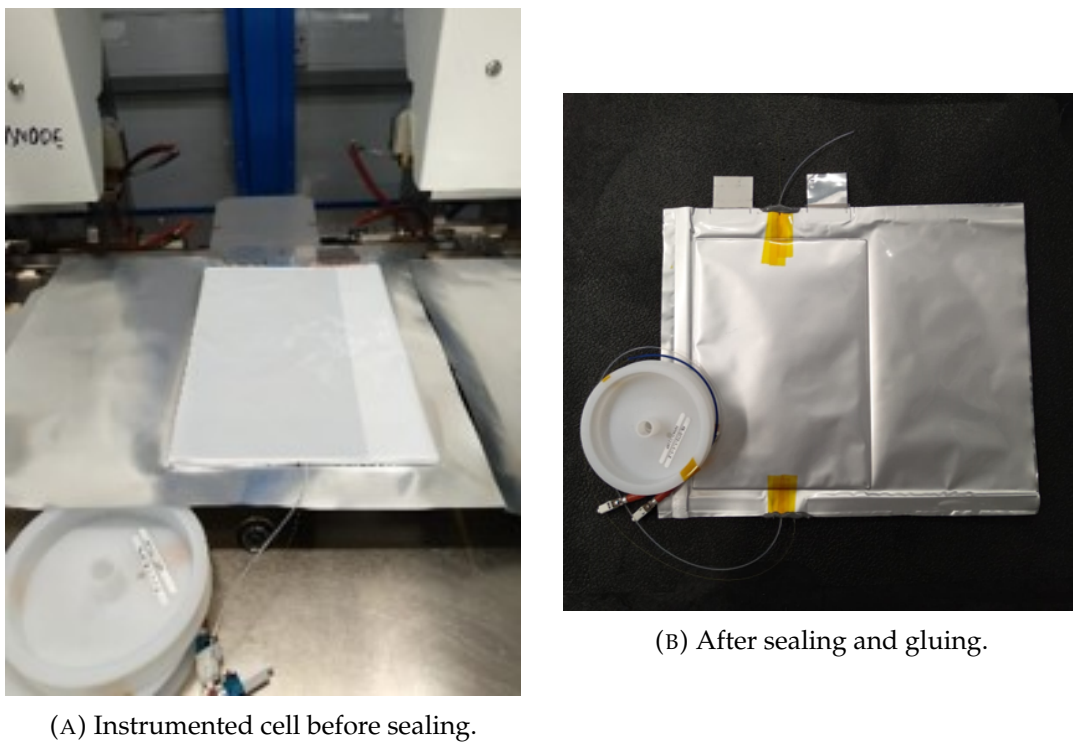
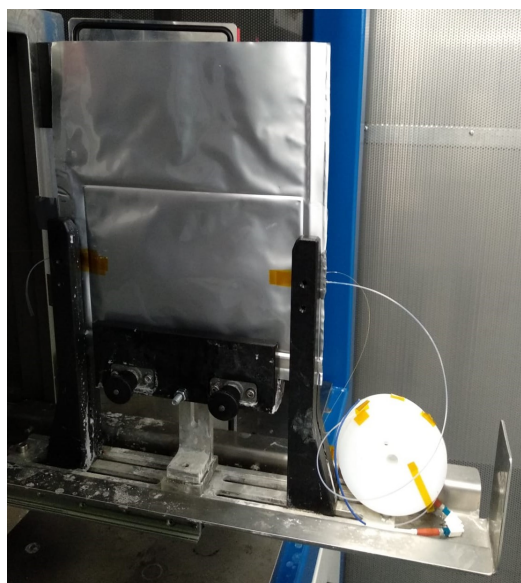


FIGURE 4.24: Manufactured instrumented cell with fibre optic sensor after assembly and sealing.



(A) Cell holder.



(B) Sealing equipment.

FIGURE 4.25: Instrumented cell electrolyte filling.



FIGURE 4.26: Instrumented cell with fibre optic sensor at the end of the manufacturing process.

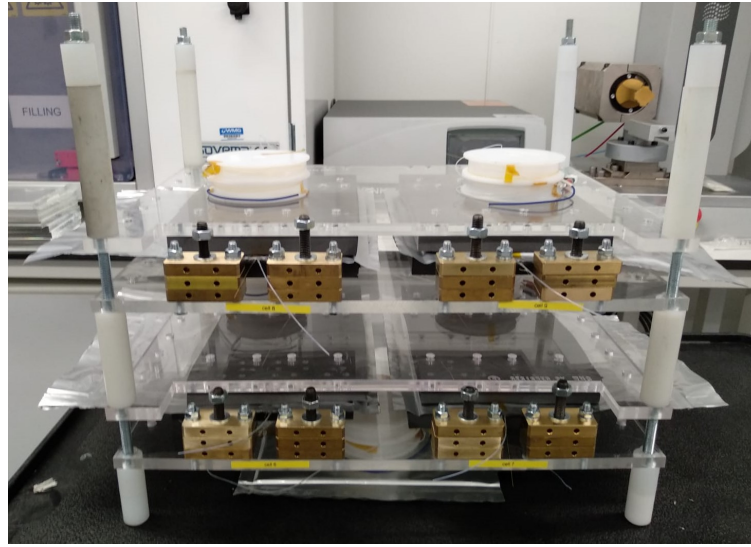


FIGURE 4.27: Instrumented cells test rig.

TABLE 4.3: Instrumented Cells Test Layout.

Quantity	Sensor SN	LUNA FOS ch	Section start (m)	Section end (m)	Cell #
Temperature	FS02019LUNA008885	1	1.955	2.140	6
Strain	FS02019LUNA060878	5	1.935	2.120	6
Temperature	FS02019LUNA008883	4	1.950	2.135	7
Strain	FS02019LUNA060851	8	1.945	2.130	7
Temperature	FS02019LUNA008884	2	1.965	2.150	8
Strain	FS02019LUNA060872	6	1.940	2.125	8
Temperature	FS02019LUNA008886	3	1.960	2.145	9
Strain	FS02019LUNA060857	7	1.950	2.135	9

Chapter 5

Cells characterization results

5.1 Manufacturing results

In the end of Section 4.3.2 the manufactured instrumented cells were accommodated in a properly designed test rig that can be placed in the climatic chamber and be easily connected to the cells cycler. In this Chapter, the cells testing results are presented.

First the four cells in the test rig were placed in a climatic chamber at 25 °C and were connected to four different channels of the cycler. When cells are connected to the cycler, if no user profile is applied, a little amount of current, either positive or negative, flows. In the cycler convention, a positive current means charging and a negative current means discharging. Fig. 5.1 shows that even if this current is positive, as for example for cells #7 and #8, the voltage measured at the cell terminals tends to decrease rather than increasing, as it would be expected to happen in charging conditions. This happens after electrolyte filling, during soaking.

After soaking, the first cycling of a cell is called formation cycle, as during this cycle the majority of the SEI layer is formed. During formation, cells were charged according to a CC-CV protocol at 0.5 A (C/10), and then discharged at the same current rate. Fig. 5.2 shows the output result of this process for the four manufactured cells. It can be clearly seen that the voltage, initially about 0 V, increases up to the charging voltage limit of 4.2 V. After a rest period, the cell is discharged up to the cutoff voltage of 2.5 V. After the first formation cycle, the cell capacity is not stable and constant yet, but it will vary from a cycle to another due to SEI formation. Thus the formation cycle is usually followed by 3 to 5 cycles called stabilization cycles. During stabilization, cells were charged according to a CC-CV protocol at 2.5 A (C/2), and then discharged at the same current rate. The result of the stabilization cycles is also shown in Fig. 5.2. The figure clearly shows that the four cells plot do not perfectly overlap. This means that the actual cells capacity is different thus the time period needed to reach the charging voltage limit and the cutoff voltage is different. As the four cells were cycled at the same current rate, longer times imply larger capacity, thus cell #6 presents the smallest capacity and cell #8 presents the largest capacity. This difference in capacity is due to differences in the manufacturing process. In conclusion, results obtained from the manufacturing process show that the cells behaviour is in line with expected results in terms of voltage profile, thus the instrumented

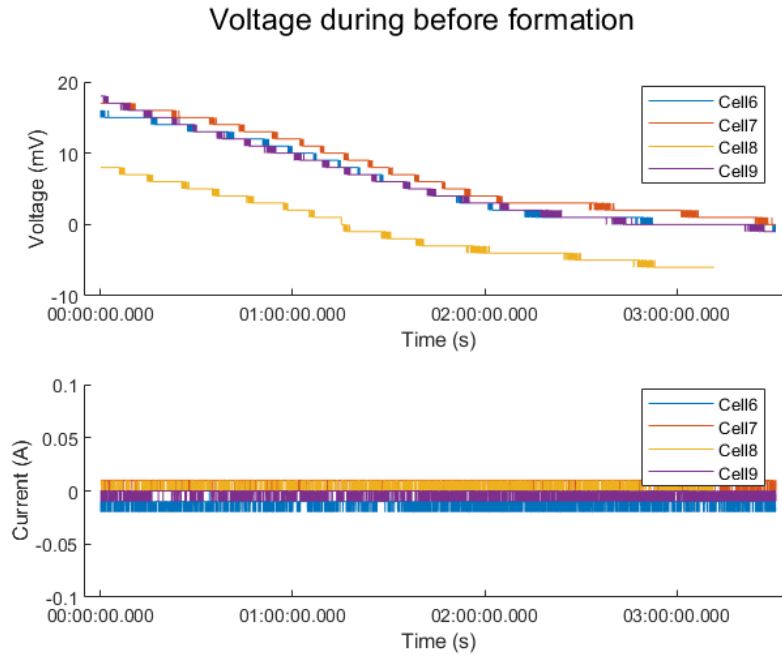


FIGURE 5.1: Cells voltage comparison after electrolyte filling and before formation.

cells manufacturing was successful.

5.2 Characterization results comparison

In order to evaluate the instrumented cells performance, after stabilization these cells went through a characterization process. In this process, instrumented cells performance were compared with conventional cells. Some of the characterization techniques presented in Section 1.3 were applied to characterize both internally instrumented and not instrumented cells to check the impact of sensors in the cells.

First the EIS characterization test was performed. In order to perform EIS analysis, a *Solartron* potentiostat with a 2 A current booster was used. Fig. 5.3 shows the cell voltage during the EIS test. The cell is first charged to 100% SOC and the first EIS measurement is performed. The cells is then discharged to 95% SOC and the EIS measurement is performed again. This procedure is repeated by moving respectively to 75% SOC, 50% SOC, 25% SOC, 5% SOC and finally 0% SOC. To do this, a cycler is used to periodically discharge the cell to a certain SOC and a potentiostat is used to periodically perform the EIS measurement.

Before performing the EIS measurement, it is important to select the current amplitude to be applied in order to get a good signal. When performing the EIS measurement, a current sine sweep with increasing amplitude is applied. The current amplitude increases up to a current amplitude limit that must be defined by the user. The user imposes a current limit I that defines

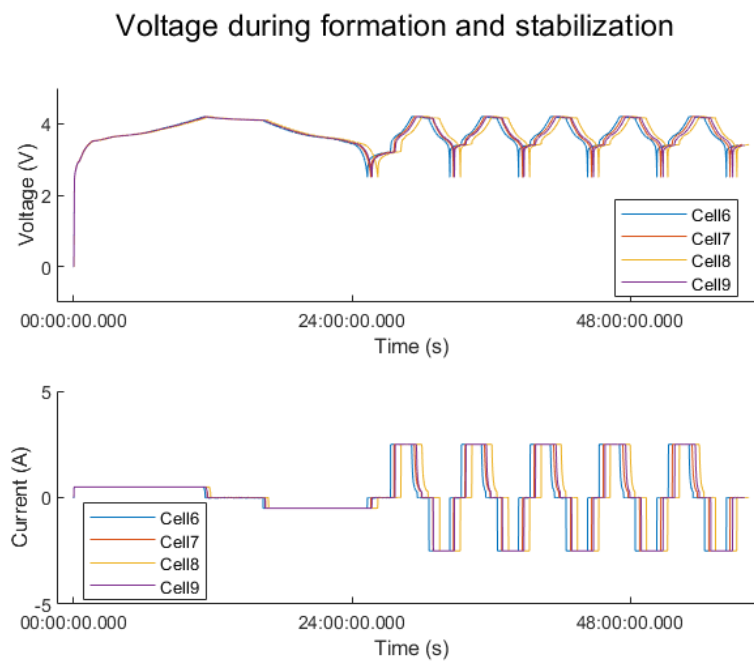


FIGURE 5.2: Cells voltage comparison during formation and stabilization.

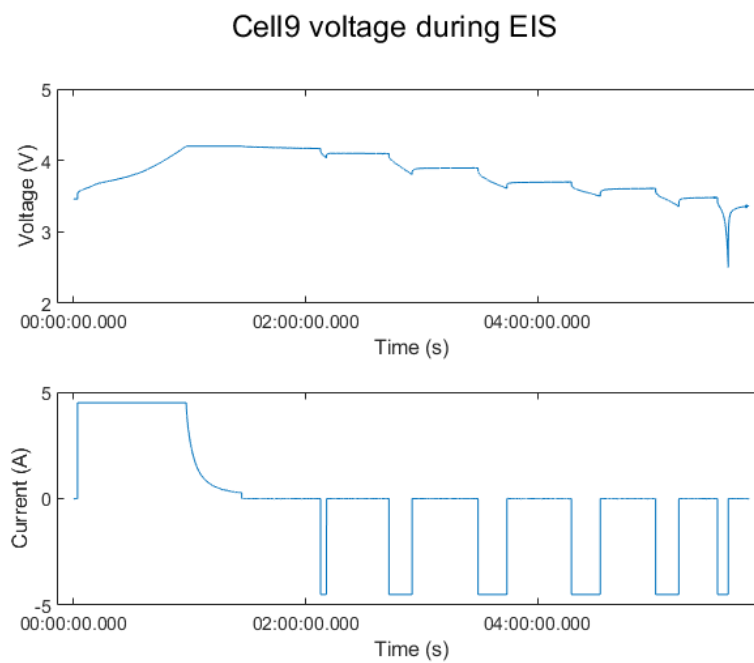


FIGURE 5.3: Cell voltage during EIS.

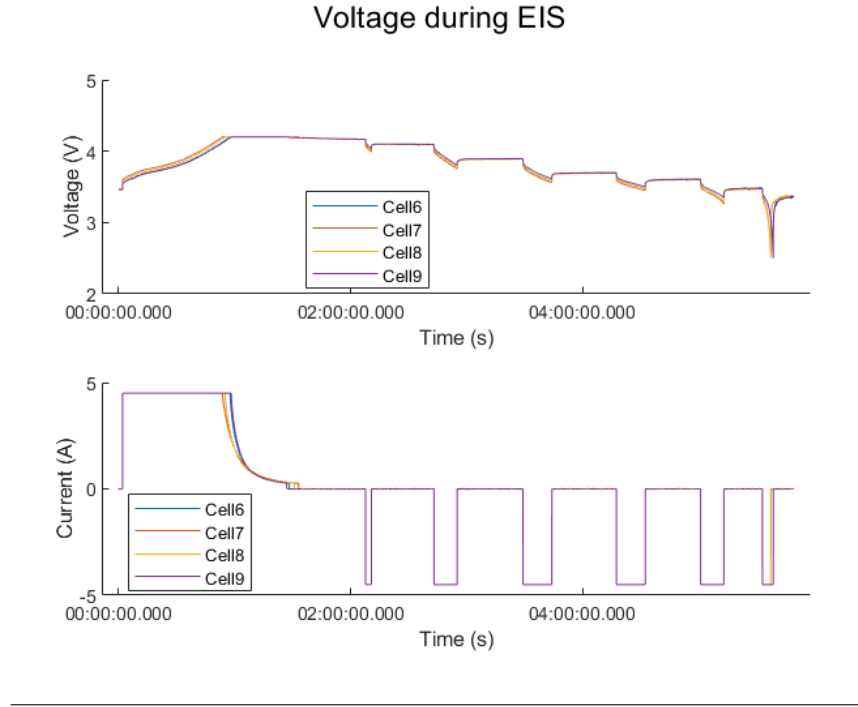


FIGURE 5.4: Cells voltage comparison during EIS.

the maximum applied current amplitude \hat{I} , according to Eq. 5.1.

$$\hat{I} = I \cdot \sqrt{2} \quad (5.1)$$

In the EIS test, the cell impedance is measured in a certain range of frequencies. In order to acquire the right impedance value, it is important to be in the linearity range that is the range in which current is linearly proportional to voltage, thus their ratio is constant. Applying a low current guarantees to be in the linearity range. However, if the current applied is too low, the result will be noisy as the signal to noise ratio (SNR) will be small. Thus it is important to identify a current amplitude to be applied that is small enough to be in the linearity range and large enough to have a good SNR. Fig. 5.5 shows a comparison of the impedance obtained at various current levels. It is usually suggested to start from a current of $C/20$, that for these cells corresponds to 250 mA. The impedance output is acquired and then the current is gradually increased respectively to 500 mA, 1000 mA and 1400 mA. The current 1400 mA represents the maximum current that can be selected on the equipment used, as the maximum current is 2000 mA ($= 1400 \cdot \sqrt{2}$). Fig. 5.5 shows that the impedance profile obtained at the various current levels doesn't vary, which means that even when the maximum current is applied, the output is always in the linearity range. Furthermore, the 250 mA output results to be more noisy and it is very evident in the circular region. The output improves at 500 mA and finally both the 1000 mA and 1400 mA current levels present a good SNR. Thus the 1000 mA current was selected for the actual EIS test as it can guarantee a good output. During the EIS measurement, a current sweep from 100 kHz to 100 mHz is applied and the

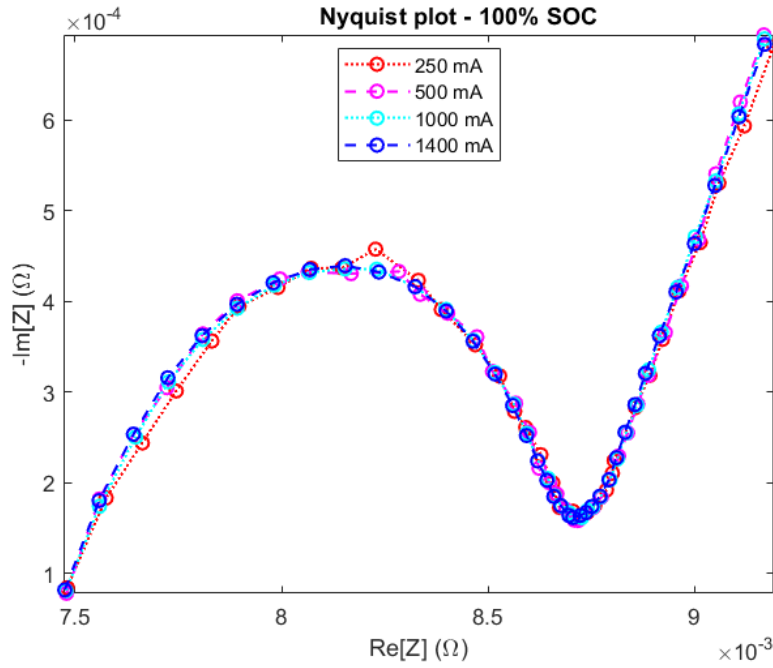


FIGURE 5.5: EIS output at various current amplitude.

test duration is about 60 seconds. The EIS test results are shown in Fig. 5.6 at various SOC levels. It is possible to observe that at the various frequencies, the not instrumented cells impedance is lower than the instrumented cells impedance. This means the DFOS introduced in the cell produced a modification of cells performance. These differences are visible especially at high and low SOC, respectively 100% SOC and 25 % SOC. However, the impedance measured in instrumented cells in the whole frequency range is comparable to impedance of not instrumented cells thus again the results can be considered successful.

Then the IC-DV test was performed. In this test cells were cycled at a current rate of $C/25$. The post-processing of data acquired in this low current charge and discharge cycles allowed to build the IC and the DV curves. Results obtained are shown in Fig. 5.7 and Fig. 5.8. Results obtained for instrumented cells are comparable with results from not instrumented cells, as peaks position and amplitude is aligned in both results. The main change is a slight capacity difference, visible in Fig. 5.8, again due to the sensor presence. Thus also the IC and DV result for instrumented cells was successful as no major differences were identified in results obtained between instrumented and not instrumented cells.

Finally, the HPPC test was performed. In this test the cell resistance is measured at various SOC levels. The test results are shown in Fig. 5.9. Results show that cells resistance of instrumented and not instrumented cells is consistent in the whole SOC range. The main difference is at low SOC where the instrumented cells resistance results to be higher.

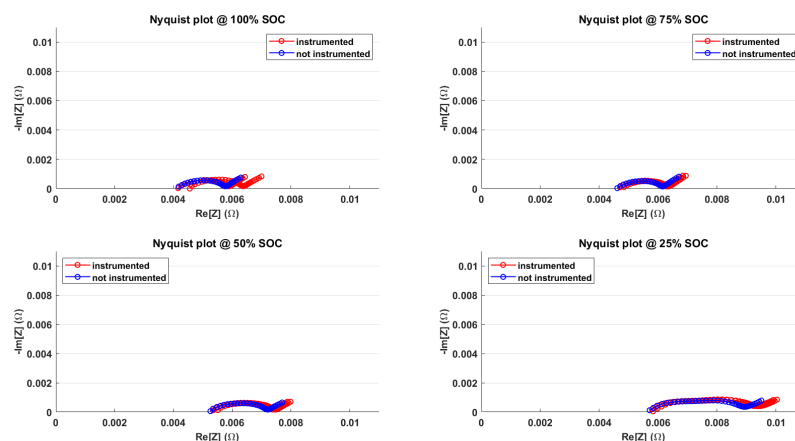


FIGURE 5.6: EIS curve comparison between internally instrumented and not instrumented cells.

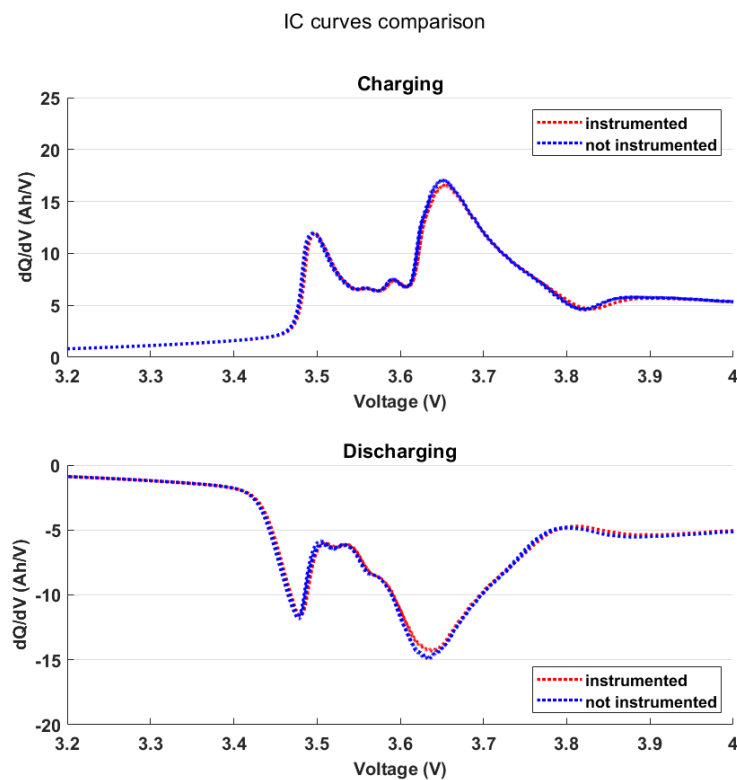


FIGURE 5.7: IC curve comparison between internally instrumented and not instrumented cells.

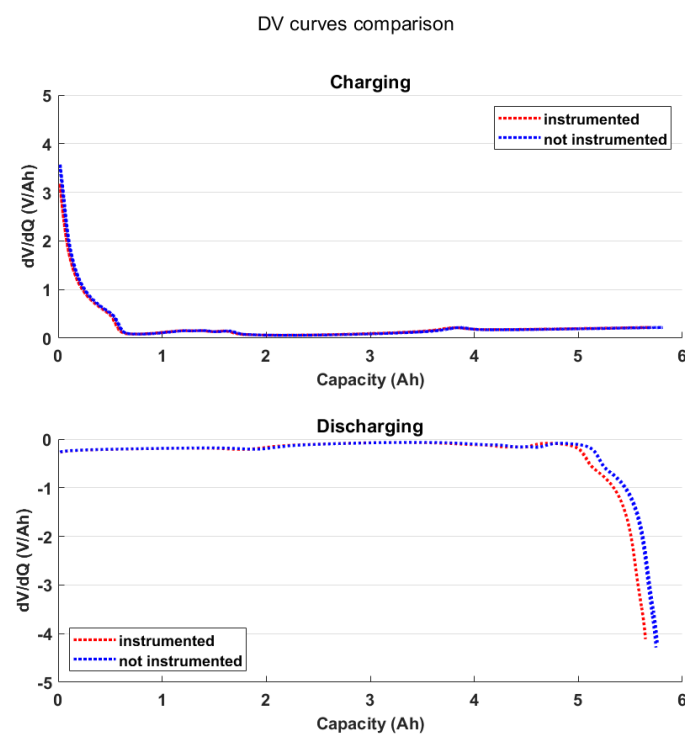


FIGURE 5.8: DV curve comparison between internally instrumented and not instrumented cells.

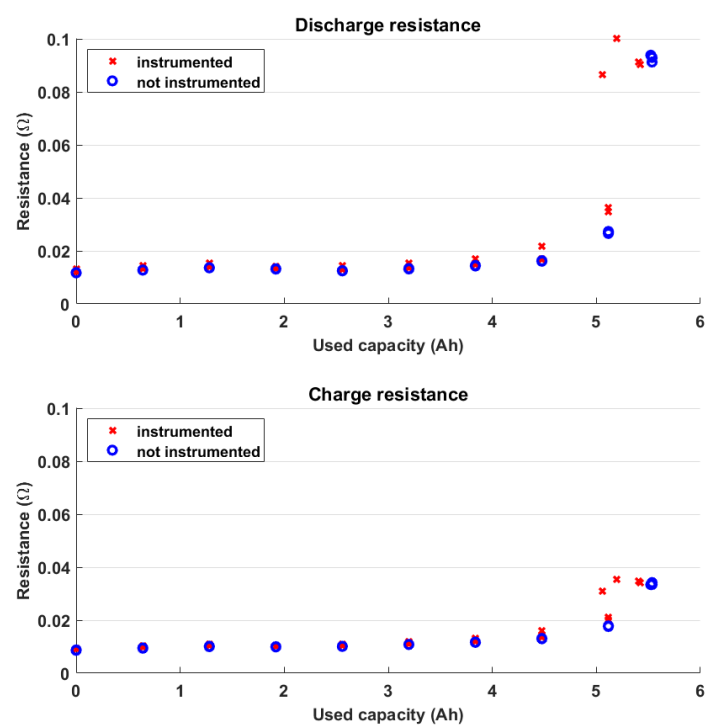


FIGURE 5.9: HPPC resistance comparison between internally instrumented and not instrumented cells.

In conclusion, characterization results obtained from the various characterization techniques implemented are consistent each other. They all show that instrumented cells capacity is slightly lower than capacity of cells manufactured according to the conventional procedure. Furthermore they show that instrumented cells impedance is slightly larger than conventional cells impedance, especially at low SOC levels. The characterization results obtained are satisfying, thus it is possible to proceed to further testing. Testing results are presented in Chapter 6.

5.3 Post-mortem analysis

After testing (Chapter 6), a post-mortem analysis was performed on instrumented cells in order to verify what happened in the electrodes region in contact with the fibre optic sensor. In order to perform the post-mortem analysis, the cell needs to be opened and disassembled. The whole procedure must be carried out in a glove-box with a low moisture content in order to avoid HF (Hydrofluoric acid) formation. In this procedure, great attention must be paid in avoiding to spread electrolyte in the operating area, as it is highly corrosive, and in avoiding to let anodes and cathodes touch each other in order to avoid short circuits.

The first step consists in preparing all necessary tools and introducing them in the glove-box through the antechamber. Once everything is ready inside the chamber, it is possible to start the procedure to open the cell. First it must be identified clearly and carefully where to cut the cell in order not to damage the stack. To cut the cell, ceramic scissors should be used, in order not to create electrical contact among the various layers touching the scissors. The cell borders should be cut on 3 sides, except for the tabs side. Once opened, the electrolyte should be squeezed out from the cell and collected in a glass bottle. The bottle filled with electrolyte should be immediately sealed in order to avoid contamination of the glove-box atmosphere. Once the electrolyte has been removed from the cell stack, the last side must be cut. To do so, the tabs location must be identified and a ceramic knife should be used to cut the terminals inside the pouch bag. When doing this, a small portion of not-coated current collector should be saved, in order to be able to easily distinguish afterwards if a certain electrode is an anode or a cathode. The stack can finally be removed from the external pouch bag. The stack closure is a polyimide green tape that locks the end part of the separator. This tape can be removed using plastic tweezers. Now the separator can be unwrapped and the positive and negative electrodes can be put apart. The electrodes should be let dry in the glove-box and then put in a sealed plastic bag and removed from the glove-box.

The disassembled electrodes can be used for SEM analysis in order to identify possible alterations with respect to normal conditions. SEM samples must be completely dry, in order to avoid equipment damage. Thus the disassembled electrodes should be put in a fume hood to let them dry completely. Now the electrodes can be cut and a small portion can be used as SEM sample for analysis. Similarly, an analysis of the extracted electrolyte can be performed by

dropping some drops on the carbon tape of a SEM sample holder. An SEM analysis of electrodes surface and electrolyte from both instrumented and not instrumented cells was carried out. The SEM equipment also allowed to perform energy dispersive X-ray spectroscopy (EDS) to investigate material elementary composition. Results showed no difference in electrodes surfaces and electrolyte composition of instrumented and not instrumented cells.

Chapter 6

Experimental tests

6.1 Data acquisition system

Both instrumented and not instrumented pouch cells were tested and aged using cyclers. Cyclers can be used to apply user defined charging and discharging profiles to battery cells in order to characterize them, to test performance and to induce ageing. According to the equipment availability, various cyclers were used for testing activities, such as *MACCOR* battery test system, *Bitrode*, *Digatron* and *Chroma* 17020 battery pack tester (equipped with one charge/discharge controller 69200-1, two regenerative charge/discharge testers 69225-60-4, one data communication unit A692000 and one DC/AC bi-directional converter A691101). All tests were performed in climatic chambers, either *Espec* or *Vötsch* Technik VT3050. Climatic chambers allow to both perform tests in temperature controlled conditions but also to protect the external environment from potential hazards related to cells. The optical sensors signal was acquired using the optical distributed sensors interrogator *LUNA* ODiSI-B and the fibre optic switch *LUNA* FOS 008. The thermocouples signal was acquired using the *NI cDAQ 9174* and the *NI 9213* module.

6.2 DFOS signals data analysis

In Section 3.2.3, the preliminary data analysis procedure applied to all data sets was explained. At the end of that procedure, the each data set consists of a matrix of size $M'' \times N$ per channel, where N is the number of gauges and M'' is the number of time instants. M'' is the same for all channels that are acquiring the output signal from sensors bonded on the same system, that is the pouch cell, as sensors output signals were synchronized. Thus from now on, the data analysis will be carried out at the same time on both sensors bonded on the same pouch cell, which means one temperature sensor and one strain sensor. The main steps of the following data analysis procedure are summarized here:

- *Step 1*: Select the sensing regions of interest along each sensor, using the information from the *touch to locate* procedure.



FIGURE 6.1: Testing setup: climatic chamber, cells cycler, distributed fibre optic sensors interrogator, thermocouples.

- *Step 2:* Align the sensing regions of interest of sensor bonded on the same cell in order to have a correspondence between the temperature DFOS and the strain DFOS output signal in each bonded section.
- *Step 3:* Perform signals decoupling.
- *Step 4:* Use calibration coefficients to convert frequency shift into a physical quantity variation.
- *Step 5:* Apply the tare to each acquisition by subtracting the value of the first acquisition on both temperature and strain sensors.
- *Step 6:* Synchronize DFOS acquisitions with thermocouples acquisitions.
- *Step 7:* Synchronize DFOS acquisitions with cycler acquisitions.
- *Step 8:* Post-process the time intervals of interest to produce graphical results.

In the following sections, the main graphical results obtained from the testing activity and the data analysis procedure are presented. The test flow used for both external and internal sensing is summarized in Fig. 6.2. Each test consist in charging the cell, having a rest period where no current is applied in order to let the cell recover, discharging the cell and having a last rest period. This flow, at a set temperature, is repeated changing the current rate from

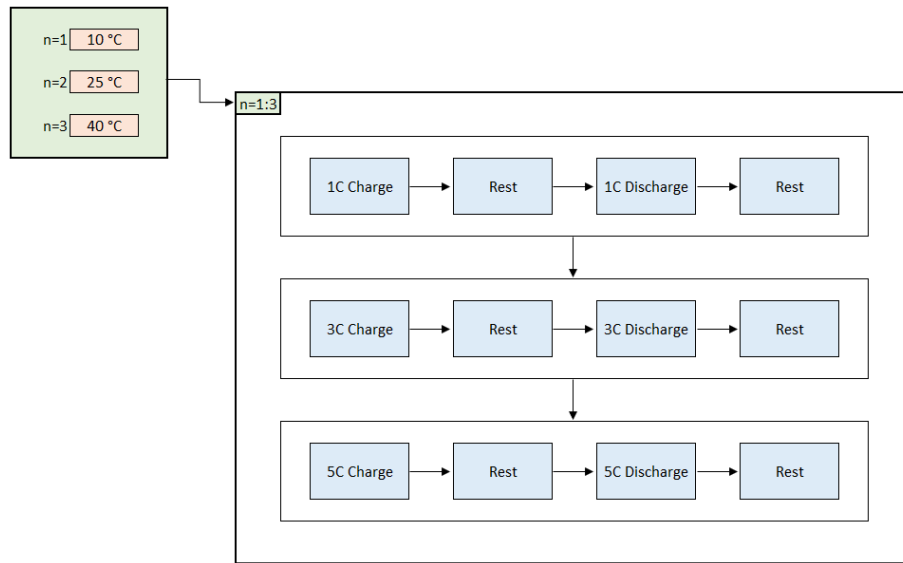


FIGURE 6.2: Cells testing at various temperature and current rate test flow.

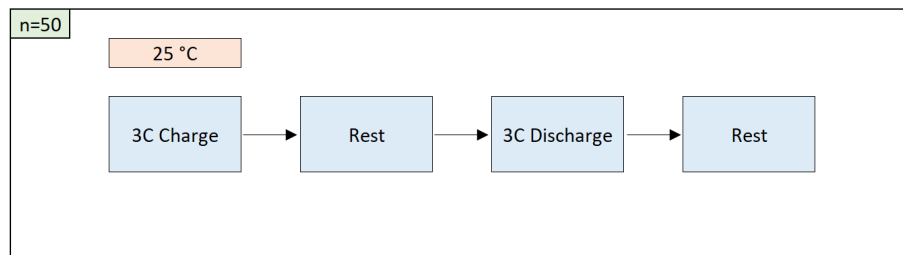


FIGURE 6.3: Cells ageing test flow.

1C to 5C. Finally, the chamber temperature is set to a different value, going from $10\text{ }^{\circ}\text{C}$ to $40\text{ }^{\circ}\text{C}$, and the flow is performed again. Then, cells ageing is performed at constant temperature and current, respectively $25\text{ }^{\circ}\text{C}$ and 3C (according to Fig. 6.3), and cells are cycled over 50 cycles.

6.3 External sensing testing

In this section, results from DFOS external instrumented cells are presented. These results are compared with data acquired from point sensors. Fig. 6.5 shows temperature sensors output. These results allow to validate results obtained from optical sensors, as the output from optical and electrical sensors is consistent, taking into account the sensors accuracy. These results also allow to highlight point sensors limitations in the information provided in order to investigate the observed phenomenon. In fact, point sensor only allow to monitor what happens in a certain localized region, thus if a certain phenomenon happens somewhere in the nearby, the point sensor is not able to detect this variation. On the contrary, temperature DFOS provide results

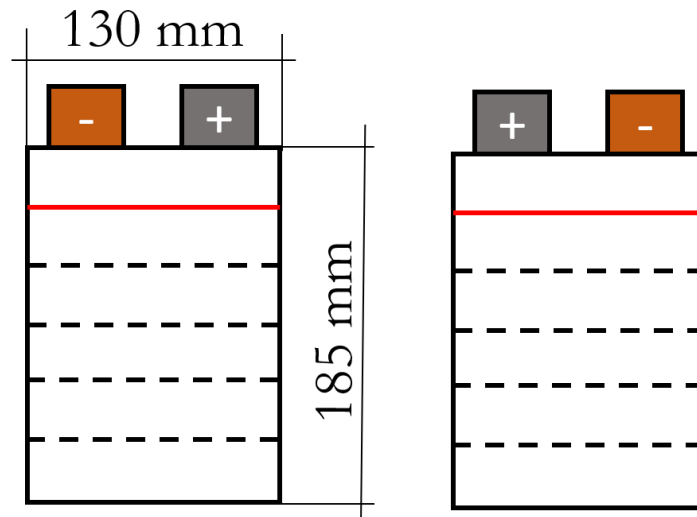


FIGURE 6.4: Sensing sections on external instrumented cells.

on a wider region.

Cells were cycled at 1C, 3C and 5C at 10 °C, 25 °C and 40 °C. During the cell cycling, external temperature experience variations of 3 °C, 7 °C e 13 °C respectively in 1C, 3C and 5C tests. No evident variations in the external temperature trend are shown when the cell is cycled at different ambient temperature. Fig. 6.6 shows the temperature distribution along the cell profile in one of this testing conditions. The temperature profile results to be quite uniform in the central region and to decrease in the cell sides.

Also the strain distribution measured along the surface is quite uniform, maximum values of about 300 $\mu\epsilon$ are recorded (Fig. 6.7). Both temperature and strain trend follow the cell behaviour in operating conditions, especially at 3C and 5C (Fig. 6.8). Strain follows the same trend as temperature, meaning that strain measured is mainly due to thermal expansion.

6.4 Internal sensing testing

In this section, results from DFOS internal instrumented cells are presented.

Fig. 6.9 shows results of formation and stabilization cycles of one instrumented pouch cell. Strain measured on the electrode follows the same trend as the voltage measured on the cell terminals in the CC charging phase, thus the strain DFOS is able to catch strain due to Li-ions intercalation and deintercalation. On the contrary, strain measured on the cell surface follows the same trend as the external temperature, thus it mainly consists in thermal strain. Fig. 6.10 is a zoom of Fig. 6.9 on one stabilization cycle. It shows that strain on the anode increases in the CC charging stage and decreases in the CV charging stage. This happens because the current flowing in the two stages is different. As explained in Section 1.3, during charging Li^+ ions

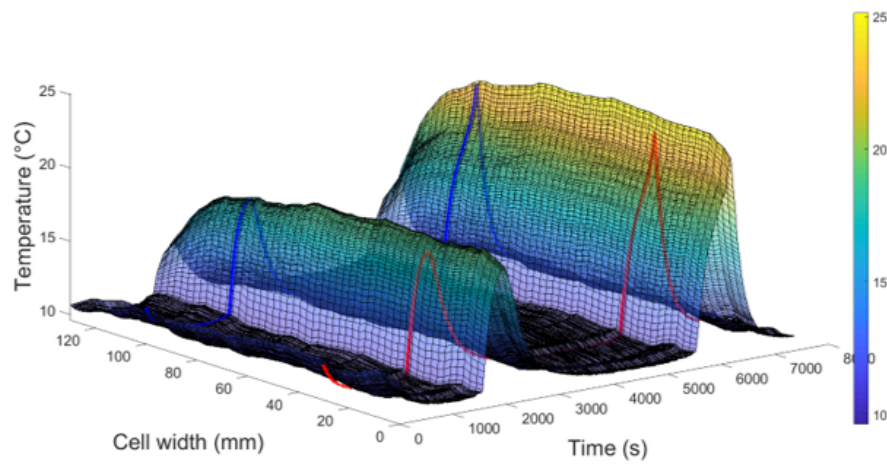


FIGURE 6.5: Point versus distributed experimental temperature measurement: evolution in time.

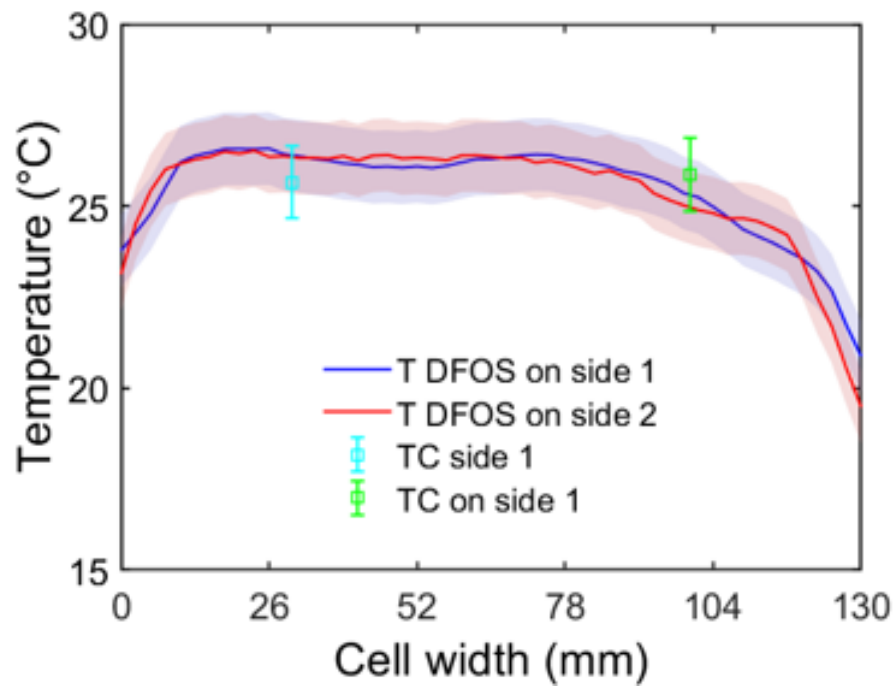


FIGURE 6.6: Point versus distributed experimental temperature measurement: evolution in space.

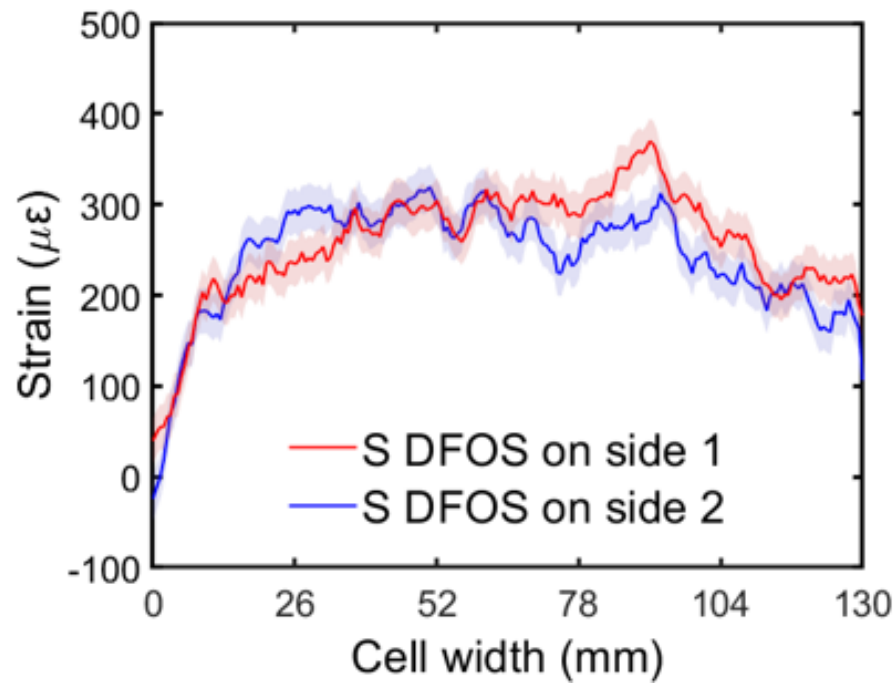


FIGURE 6.7: Distributed experimental strain measurement: evolution in space.

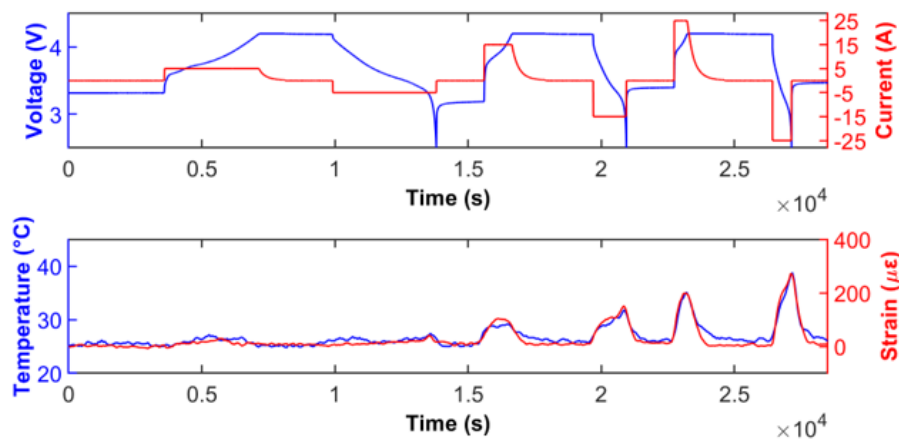


FIGURE 6.8: Distributed experimental temperature and strain measurement: evolution in time.

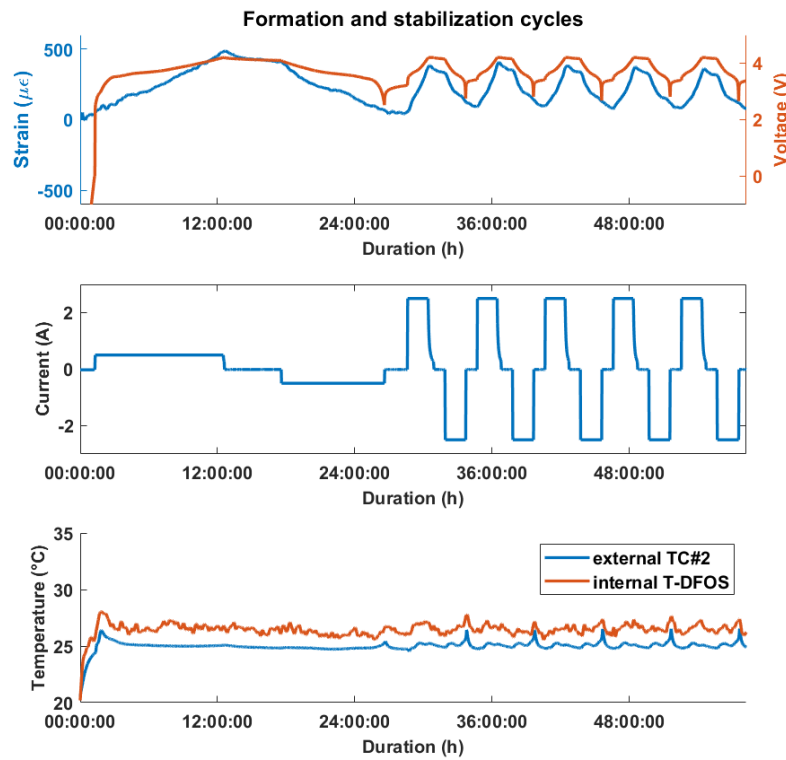


FIGURE 6.9: Formation and stabilization cycles of one instrumented pouch cell.

leave the positive electrode and intercalate into the negative electrode. This means that during charging that the anode active material must accept the Li^+ ions and host them thus the stress in the anode will increase. When Li^+ ions intercalate, they first enter the anode surface and then slowly diffuse into the anode thickness in order to fill the empty spaces available. This diffusion process takes some time. In the CC phase current is constant thus a constant amount of Li^+ ions is flowing into the anode producing a stress level that is linearly increasing. Then, in the CV phase, the current flowing is decreasing, but still Li^+ ions are moving to the anode thus the number of Li^+ ions in the anode is increasing. The reason why the stress level in the CV phase is decreasing is due to the fact that, because the current flow is reduced, Li^+ ions have more time to diffuse and rearrange into the anode. In the discharging phase, Li^+ ions leave the negative electrode, thus the stress level decreases.

The trend of internal temperature measured follows quite well the overall trend of external temperature. Internal temperature results to be about 2°C higher than external temperature. Internal temperature sensor output results to be quite noisy as measured temperature variations are close to the sensor accuracy.

After formation and stabilization, the cells were cycled at 3 different temperatures and with 3 different currents in order to record what happens to

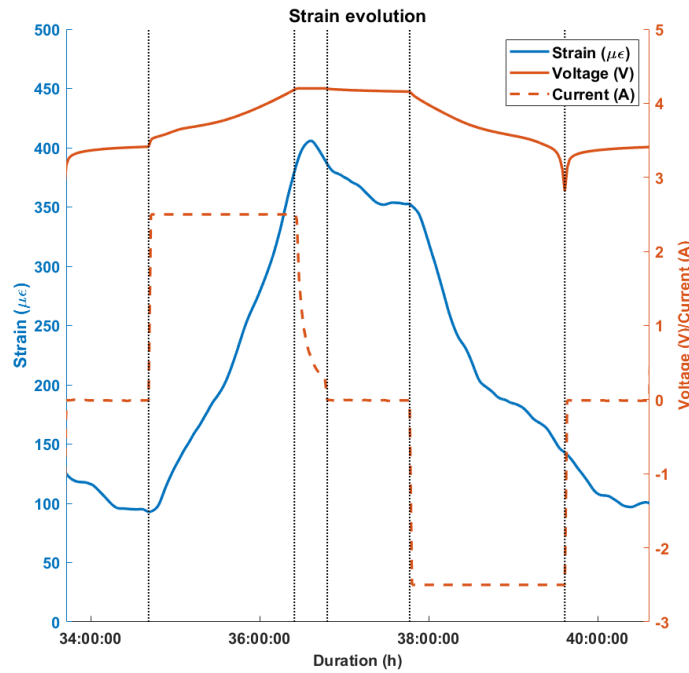
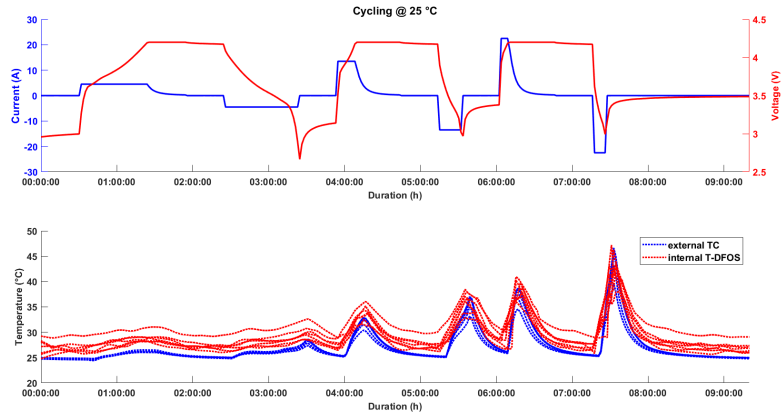


FIGURE 6.10: Zoom on one stabilization cycle of one instrumented pouch cell.

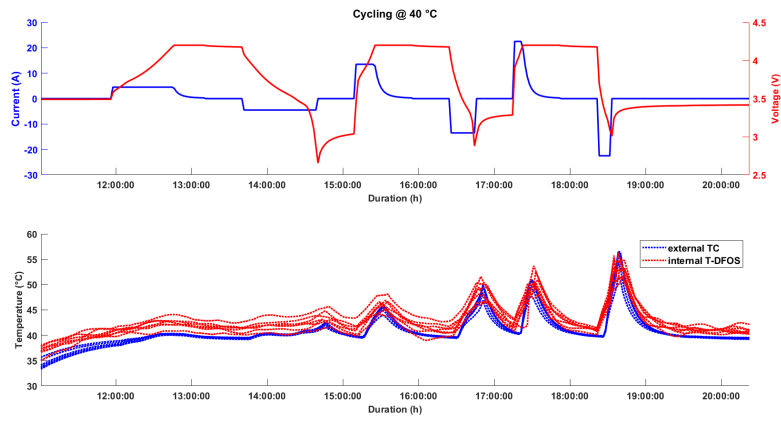
strain and temperature in various operating conditions. The cells were cycled at 10 °C, 25 °C and 40 °C with a current of 1C, 3C and 5C. The temperature results obtained are shown in Fig. 6.11a, 6.11b and 6.11c. It is possible to clearly observe that internal temperature sensor are much more reactive to temperature variation. In fact, as soon as current starts to flow, the internal temperature sensor records a temperature increment, while it takes longer for the external sensors to react. In all temperature and current conditions it is possible to clearly identify this delay.

The cells were cycled for 50 cycles. Focusing on the hottest point during cycling it is possible to observe an evident variation of the hottest point within one cycle but no variation with ageing. When the cell is charging, the cell hottest region is the bottom region of the cell, while during discharging the cell hottest region is the top region of the cell. This trend is confirmed from the temperature measurements acquired from both external TC and internal T-DFOS. Cells location are named from 1 to 7 respectively from top to the bottom of the cell. From Fig. 6.12 it is possible to observe that when current is positive (charging phase) the maximum temperature is in location 5 (bottom of the cell), while when current is negative (discharging phase) the maximum temperature is in location 2 (top of the cell). This trend is repeated over cycling and no differences in the hottest point are highlighted with ageing.

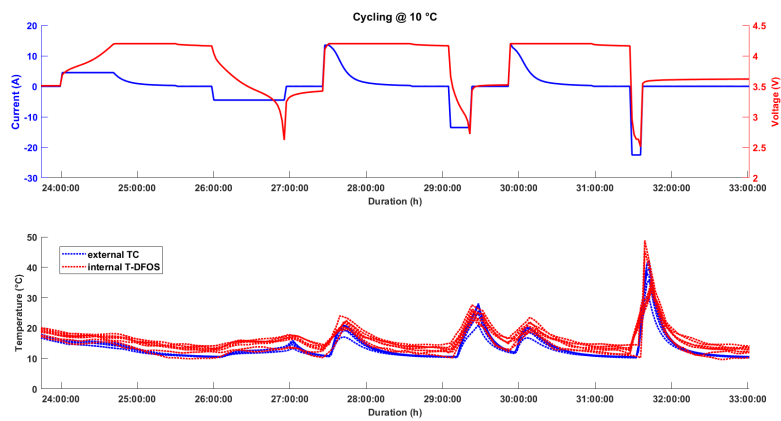
No additional information come from strain sensors as during cycling the sensor separated from the anode surface, thus it was no more able to record



(A) Cycling @ 25 °C.



(B) Cycling @ 40 °C.



(c) Cycling @ 10 °C.

FIGURE 6.11: Cycling at 1C, 3C, 5C @ 25, 40, 10 °C.

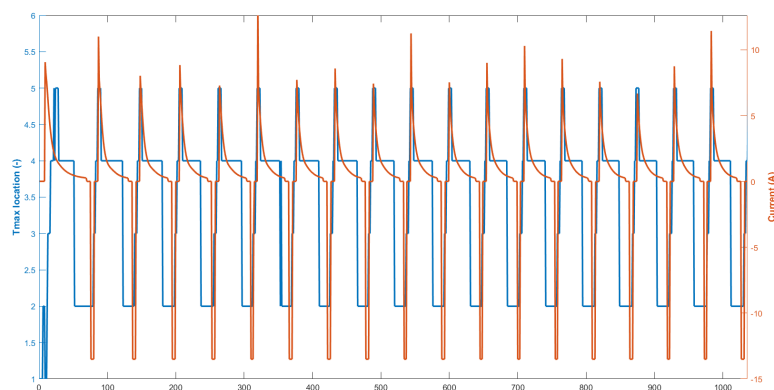


FIGURE 6.12: Tmax location during cycling.

strain variations. The strain sensor separation from the cell anode was not expected to happen. The bonding technique was proven to work on a dummy cell at beginning of life (BoL), however it was not investigated over cycling. In the implementation in an actual working cell the bonding procedure resulted to be suitable for the first cycles, however it was not able to withstand the following ones. The bonding failure is mainly to be attributed to the mismatch between the anode and the optic sensor thermal expansion coefficient. The bonding procedure was performed at room temperature, at about 20–23 °C. Similarly, the cells formation and stabilization cycles were performed at 25 °C. In these cycles the bonded strain sensor was able to withstand both the strain variation due to Li-ions intercalation/de-intercalation in the anode and the mismatch between the anode and sensor thermal expansion induced by the cell internally generated heat and the temperature variation over cycling. However, after this initial stage at constant ambient temperature, the cells were exposed to an environmental temperature cycle over a wide temperature range (10 °C to 40 °C). In this condition, the thermal expansion mismatch between the sensor and the substrate was enhanced and caused the sensor separation from the anode. The strain sensor signal was still readable, meaning that no sensor damage occurred over cycling, however as it was no more bonded to the surface, it was no more able to monitor strain. This bonding failure suggests that in a future installation, the bonding procedure defined should be performed at a temperature that is as close as possible to be testing temperature and that testing should be performed at constant environmental temperature.

Chapter 7

Conclusions

7.1 Comparison of previous literature studies

In the present work, the conditions summarized in Fig. 7.1 were studied, implemented and analyzed. Results obtained from testing activities are here compared with results from the literature, reviewed and summarized.

As anticipated in [118], one fibre optic sensor was used to monitor multiple cells in the external sensing configuration.

As investigated by [118], pouch cells were internally instrumented with FO sensors characterized by an external diameter of $125\ \mu\text{m}$, as this allows to introduce a low invasive modification in the manufacturing process and thus to reduce risk of moisture ingress into the cell and electrolyte egress out of the cell. As in [118], the FO was placed in the middle layer of the stack, in order to avoid further curvature when exiting the pouch cell. As in [118] the instrumented electrode was the anode. In [118] the FO was bonded to the anode surface using SBR, as it was also used in the anode slurry of the pouch cells used within that work. On the contrary, the anode slurry of pouch cells used in this work was made with PVDF, as it was NMP based, thus it was selected as a better and more effective choice. With respect to [118], in the instrumented cells manufacturing process there was no need to use any additional protective heat seal film to properly seal the bag. On the contrary, in order to avoid to damage the sensor, the sealing region overlapped with the sensor was not sealed with the conventional pressurized hot plates of the sealing machine, but a partial sealing was performed and the remaining region was sealed using some structural glue.

Temperature results show that, as in [103], temperature-DFOS have an faster response time with respect to K-type thermocouples.

Strain results in [140] showed that using FBGs bonded to the pouch cells surface it was possible to monitor strain evolution during cycling. On the contrary, in this study it was not possible to detect strain variation with externally mounted strain-DFOS, and it was only possible with internally mounted sensors. As explained by [118], this difference can be attributed to the fact that the internal FO sensor is bonded to the anode that is characterized by a much smaller thermal expansion coefficient than the pouch bag, thus it is less sensitive to temperature changes. As in [118], the strain sensor results show repeatable wavelength shift versus SOC curves for discharging in the whole SOC range and during charging only in the constant current

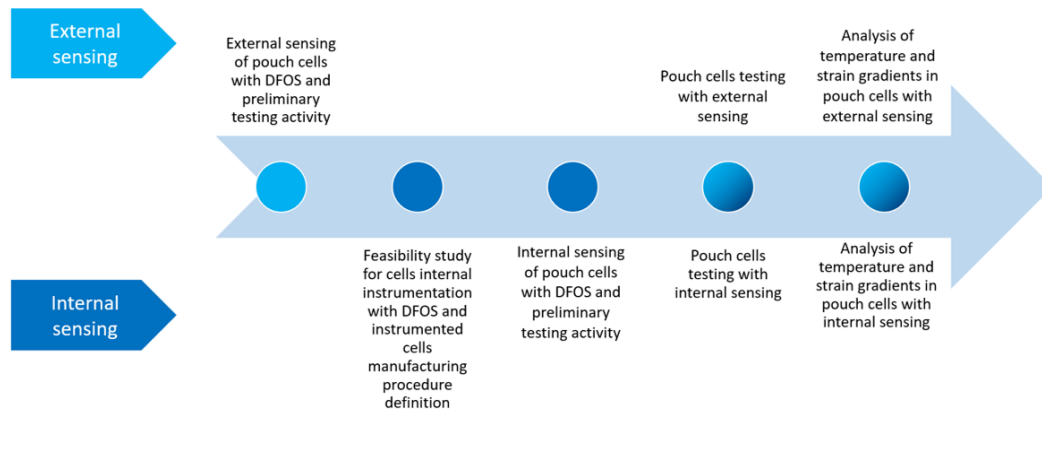


FIGURE 7.1: Summary of conditions studied in the present work.

range, while in the charging constant voltage range, the wavelength shift is no more representative of the SOC.

7.2 Implications of the work

Further conclusions can be derived from the experimental tests results:

- The Proof of concept was successful, showing that it is possible to use DFOS to manufacture instrumented cells, never done before, having performance comparable with conventional cell.
- Distributed fibre optic sensors have been effectively used to monitor temperature and strain in pouch cells. An instrumentation procedure was defined and signals were acquired continuously during cycling, thus an in-situ in-operando monitoring was performed.
- Temperature distributed fibre optic sensors were able to monitor the cell behavior during the whole testing duration. On the contrary, strain distributed fibre optic sensors were able to monitor the cell behavior during the initial testing duration, but after the first cycles, the sensor separated from the anode surface thus it was no more able to detect strain variations.
- No evident temperature or strain peaks distribution was highlighted in the experimental tests performed.

These results can be analyzed to implement some improvements in future works:

- Fibre sensors can not only be used to monitor strain and temperature distributed signals. They can also be coated with different materials in order to detect different elements and compounds. Thus, they can be used as chemical sensors. Once the procedure to instrument cell

has been developed and validated, new kind of sensors based on fibre optics, can be investigated and developed.

- The fibre optic sensor can be coated on the current collector directly during the manufacturing process. This might be less invasive and might produce a lower impact in the instrumented cells performance.
- It might be worth inducing further ageing to instrumented cells to evaluate if when more ageing occurs the temperature and strain distribution changes along the cell profile. Ageing can be induced by cycling at lower temperature and higher C-rate in order to accelerate ageing mechanisms to happen. DFOS output signal can be correlated with information on the cell state deriving from cells characterization techniques. As explained in Section 1.3.3, various characterization techniques are currently used to investigate the state of a battery and they are mainly implemented off-board. As DFOS are installed on-board and provide a real-time information on the cell condition, having a correlation between ageing mechanisms and DFOS output signals would allow to perform an on-board detection of cells abnormal behaviour and to preventively intervene to avoid further damage of the battery pack.
- As already presented in [118], where pouch cells were instrumented with temperature and strain FBGs, instrumented cells can be used as a substitute of some conventional cells in battery modules and packs. This is the reason why it is very important that these instrumented cells have performance comparable to conventional cells. In a battery module, instrumented cells would provide additional information of the condition of cells that experienced similar working conditions, as they are all located in a certain region of the battery pack, they are subjected to a similar surrounding temperature, mechanical vibration and power request. Thus, after the study performed at cell level, a module level study should be performed.

Bibliography

- [1] *A Brief History of Optical Fiber*. URL: http://www.olsontech.com/mr{_}fiber/fiber-history.htm{\%}0A.
- [2] Takeshi Abe et al. "Solvated Li-Ion Transfer at Interface Between Graphite and Electrolyte". In: *Journal of The Electrochemical Society* 151.8 (2004), A1120. ISSN: 00134651. DOI: [10.1149/1.1763141](https://doi.org/10.1149/1.1763141).
- [3] Takayuki Nakajima Akira Yoshino, Kenichi Sanechika. *US 4668595 - Secondary Battery*. 1985.
- [4] A.C. Alkidas. "Combustion advancements in gasoline engines". In: *Energy Convers. Manag.* 48 (2007), pp. 2751–2761.
- [5] Seong Jin An et al. "Design and Demonstration of Three-Electrode Pouch Cells for Lithium-Ion Batteries". In: 164.7 (2017), pp. 2–11. DOI: [10.1149/2.0031709jes](https://doi.org/10.1149/2.0031709jes).
- [6] Todd M. Bandhauer, Srinivas Garimella, and Thomas F. Fuller. "A Critical Review of Thermal Issues in Lithium-Ion Batteries". In: *Journal of The Electrochemical Society* 158.3 (2011), R1. ISSN: 00134651. DOI: [10.1149/1.3515880](https://doi.org/10.1149/1.3515880). arXiv: [1701.08214](https://arxiv.org/abs/1701.08214). URL: <http://jes.ecsdl.org/cgi/doi/10.1149/1.3515880>.
- [7] Anthony Barré et al. "A review on lithium-ion battery ageing mechanisms and estimations for automotive applications". In: *Journal of Power Sources* 241 (2013), pp. 680–689. ISSN: 03787753. DOI: [10.1016/j.jpowsour.2013.05.040](https://doi.org/10.1016/j.jpowsour.2013.05.040). URL: <http://dx.doi.org/10.1016/j.jpowsour.2013.05.040>.
- [8] Shenzhen Lithium Battery and International Summit. "The Rechargeable Battery Market and Main Trends 2012-2025". In: September (2013).
- [9] Gert Berckmans et al. "Cost projection of state of the art lithium-ion batteries for electric vehicles up to 2030". In: *Energies* 10.9 (2017). ISSN: 19961073. DOI: [10.3390/en10091314](https://doi.org/10.3390/en10091314).
- [10] W. Berg. "Legislation for the reduction of exhaust gas emissions". In: *Traffic and Environment*. Ed. by Springer. Gruden, D. Berlin/Heidelberg, Germany, 2003, pp. 175–253. ISBN: 978-3-540-00050-1.
- [11] Donald Berndt and James Clifford. "DTW(dynamic time warping)". In: *Workshop on Knowledge Knowledge Discovery in Databases* 398 (1994), pp. 359–370.
- [12] Berker Bilgin et al. "Making the Case for Electrified Transportation". In: *IEEE Transactions on Transportation Electrification* 1.1 (2015), pp. 4–17. ISSN: 23327782. DOI: [10.1109/TTE.2015.2437338](https://doi.org/10.1109/TTE.2015.2437338).

- [13] Christoph R. Birkel et al. "Degradation diagnostics for lithium ion cells". In: *Journal of Power Sources* 341. February (2017), pp. 373–386. ISSN: 03787753. DOI: [10.1016/j.jpowsour.2016.12.011](https://doi.org/10.1016/j.jpowsour.2016.12.011). URL: <http://dx.doi.org/10.1016/j.jpowsour.2016.12.011>.
- [14] L.F. Nazar B.L. Ellis, K.T. Lee. "Positive electrode materials for Li-ion and Li-batteries". In: *Chemistry of Materials* 22.3 (2010), pp. 691–714.
- [15] Kyle Bradbury. "Energy Storage Technology Review". In: January 2010 (2010).
- [16] Ralph J Brodd and Henderson Nv. "Comments on the History of Lithium-Ion Batteries". In: (2002), p. 89074.
- [17] Heide Budde-Meiwes et al. "A review of current automotive battery technology and future prospects". In: *Proceedings of the Institution of Mechanical Engineers, Part D: Journal of Automobile Engineering* 227.5 (2013), pp. 761–776. ISSN: 09544070. DOI: [10.1177/0954407013485567](https://doi.org/10.1177/0954407013485567).
- [18] Heide Budde-Meiwes et al. "A review of current automotive battery technology and future prospects". In: *Proceedings of the Institution of Mechanical Engineers, Part D: Journal of Automobile Engineering* 227.5 (2013), pp. 761–776. ISSN: 09544070. DOI: [10.1177/0954407013485567](https://doi.org/10.1177/0954407013485567).
- [19] Stephan Buller et al. "Impedance-based non-linear dynamic battery modeling for automotive applications". In: *Journal of Power Sources* 113.2 (2003), pp. 422–430. ISSN: 03787753. DOI: [10.1016/S0378-7753\(02\)00558-X](https://doi.org/10.1016/S0378-7753(02)00558-X).
- [20] Celgard. "High performance Battery Separators". In: 2200 (). URL: http://www.jobike.it/Public/data/DanieleConsolini/2012517114032{_}Celgard{_}Product{_}Comparison{_}10002.pdf.
- [21] G. Chan, T.W.; Meloche, E.; Kubsh, J.; Rosenblatt, D.; Brezny, R.; Rideout. "Evaluation of a gasoline particulate filter to reduce particle emissions from a gasoline direct injection vehicle". In: *SAE Int. J. Fuels Lubr.* 5 (2012), pp. 1277–1290.
- [22] Climate Change. *Building a low-carbon economy – the UK 's contribution to tackling climate change*. Vol. 8. December. 2008, pp. 201–208. ISBN: 9780117039292. URL: <http://www.theccc.org.uk/reports/building-a-low-carbon-economy>.
- [23] Nalin A. Chaturvedi et al. "Algorithms for advanced battery-management systems - Modeling, estimation, and control challenges for lithium-ion batteries". In: *Proceedings of the 2010 American Control Conference, ACC 2010 June 2010* (2010), pp. 1997–2002. DOI: [10.1109/acc.2010.5531623](https://doi.org/10.1109/acc.2010.5531623).
- [24] Yi Hsien Chiang, Wu Yang Sean, and Jia Cheng Ke. "Online estimation of internal resistance and open-circuit voltage of lithium-ion batteries in electric vehicles". In: *Journal of Power Sources* 196.8 (2011), pp. 3921–3932. ISSN: 03787753. DOI: [10.1016/j.jpowsour.2011.01.005](https://doi.org/10.1016/j.jpowsour.2011.01.005). URL: <http://dx.doi.org/10.1016/j.jpowsour.2011.01.005>.

- [25] Jon P Christopherson. "Battery Test Manual For Electric Vehicles Battery Test Manual For Electric Vehicles". In: June (2015).
- [26] City of Houston. "Recommended Electric Vehicle Charging Infrastructure Deployment Guidelines for the Greater Houston Area". In: (2010), pp. 1–58. URL: <http://www.greenhoustontx.gov/ev/pdf/evdeploymentguidelines.pdf>.
- [27] MTI Corporation. *Aluminum Laminated Film for Pouch Cell Case*. URL: <https://www.mtixtl.com/EQ-alf-700-20M.aspx>.
- [28] P. Novák D. Goers, M.E. Spahr, A. Leone, W. Märkle. "The influence of the local current density on the electrochemical exfoliation of graphite in lithium-ion battery negative electrodes". In: *Electrochimica Acta* 56.11 (2011), pp. 3799–3808.
- [29] J. Xie D. Li, J. Ouyang, H. Li. "Accuracy state of charge estimation used in energy storage system for electric transportation". In: *2014 IEEE Conference and Expo Transportation Electrification Asia-Pacific* (2014), pp. 1–6.
- [30] T. Reddy D. Linden. *Handbook of Batteries*. Ed. by McGraw-Hill. third ed. 2001.
- [31] Wu F. Ding Y, Mu D, Wu B, Wang R, Zhao Z. "Recent progresses on nickel-rich layered oxide positive electrode materials used in lithium-ion batteries for electric vehicles". In: *Appl Energy* 195 (2017), pp. 586–99. DOI: <https://doi.org/10.1016/j.apenergy.2017.03.074>.
- [32] D.W. Dees D.P. Abraham, S.D. Poppen, A.N. Jansen, J. Liu. "Application of a lithium-tin reference electrode to determine electrode contributions to impedance rise in high-power lithium-ion cells". In: *Electrochim. Acta* 49.26 (2004), pp. 4763–4775. DOI: <http://dx.doi.org/10.1016/j.electacta.2004.05.040>.
- [33] Matthieu Dubarry, Arnaud Devie, and Bor Liaw. "The value of battery diagnostics and prognostics". In: *J. Energy Power Sources* 1.5 (2014), pp. 242–249.
- [34] Matthieu Dubarry and Bor Yann Liaw. "Identify capacity fading mechanism in a commercial LiFePO₄ cell". In: *Journal of Power Sources* 194.1 (2009), pp. 541–549. ISSN: 03787753. DOI: [10.1016/j.jpowsour.2009.05.036](https://doi.org/10.1016/j.jpowsour.2009.05.036).
- [35] Matthieu Dubarry, Cyril Truchot, and Bor Yann Liaw. "Synthesize battery degradation modes via a diagnostic and prognostic model". In: *Journal of Power Sources* 219 (2012), pp. 204–216. ISSN: 03787753. DOI: [10.1016/j.jpowsour.2012.07.016](https://doi.org/10.1016/j.jpowsour.2012.07.016). URL: <http://dx.doi.org/10.1016/j.jpowsour.2012.07.016>.
- [36] Matthieu Dubarry et al. "Identifying battery aging mechanisms in large format Li ion cells". In: *Journal of Power Sources* 196.7 (2011), pp. 3420–3425. ISSN: 03787753. DOI: [10.1016/j.jpowsour.2010.07.029](https://doi.org/10.1016/j.jpowsour.2010.07.029). arXiv: [arXiv:1011.1669v3](https://arxiv.org/abs/1011.1669v3). URL: <http://dx.doi.org/10.1016/j.jpowsour.2010.07.029>.

- [37] K.G. Duleep. "The Impact of Gasoline Direct Injection System Design on PM Emissions". In: *SAE Technical Paper: Warrendale, PA, USA* (2019).
- [38] P. Eastwood. *Particulate Emissions from Vehicles*. Ed. by Wiley. Wiley-Prof. Chichester, UK, 2008. ISBN: 978-0-470-72455-2.
- [39] Madeleine Ecker, Pouyan Shafiei Sabet, and Dirk Uwe Sauer. "Influence of operational condition on lithium plating for commercial lithium-ion batteries – Electrochemical experiments and post-mortem-analysis". In: *Applied Energy* 206.November (2017), pp. 934–946. ISSN: 03062619. DOI: [10.1016/j.apenergy.2017.08.034](https://doi.org/10.1016/j.apenergy.2017.08.034).
- [40] Linda Ager Wick Ellingsen. "The size and range effect: Life-cycle greenhouse gas emissions of electric vehicles". In: *Environmental Research Letters* 11.5 (2016), p. 054010. ISSN: 10277358. DOI: [10.1088/1748-9326/11/5/054010](https://doi.org/10.1088/1748-9326/11/5/054010).
- [41] U.S. Department of Energy. "Advanced Research Projects Agency-Energy (ARPA-E), Request for Information DE-FOA-0000673". In: *Advanced Technologies for Robust Control of Energy Storage* (2012).
- [42] EPA. "Advancing Sustainable Materials Management". In: November (2013). ISSN: 1098-6596. DOI: [10.1017/CB09781107415324.004](https://doi.org/10.1017/CB09781107415324.004). arXiv: [arXiv:1011.1669v3](https://arxiv.org/abs/1011.1669v3).
- [43] European Commission. "A Roadmap for moving to a competitive low carbon economy in 2050". In: *European Commission: Brussels, Belgium* (2011).
- [44] European Commission. *Roadmap to a Single European Transport Area–Towards a competitive and resource efficient transport system*. 2011, pp. 1–31. ISBN: 9789279182709. DOI: [10.2832/30955](https://doi.org/10.2832/30955). arXiv: [9809069v1](https://arxiv.org/abs/9809069v1) [arXiv:gr-qc]. URL: [http://scholar.google.com/scholar?hl=en&btnG=Search{\\&}q=intitle:Roadmap+to+a+Single+European+Transport+Area+?+Towards+a+competitive+and+resource+efficient+transport+system{\\#}0](http://scholar.google.com/scholar?hl=en&btnG=Search&q=intitle:Roadmap+to+a+Single+European+Transport+Area+?+Towards+a+competitive+and+resource+efficient+transport+system{\\#}0).
- [45] M.E. Spahr F. Joho, P. Novak. "Safety aspects of graphite negative electrode materials for lithium-ion batteries". In: *Journal of the Electrochemical Society* 149 (2002), A1020–A1024.
- [46] Ricardo Faria et al. "A sustainability assessment of electric vehicles as a personal mobility system". In: *Energy Conversion and Management* 61 (2012), pp. 19–30. ISSN: 01968904. DOI: [10.1016/j.enconman.2012.02.023](https://doi.org/10.1016/j.enconman.2012.02.023).
- [47] FIBERCORE. "Stripping fiber coatings - Technical Notes". In: *FIBERCORE Technical Notes* (2018).

- [48] Christian Fleischer et al. "On-line adaptive battery impedance parameter and state estimation considering physical principles in reduced order equivalent circuit battery models part 2. Parameter and state estimation". In: *Journal of Power Sources* 262 (2014), pp. 457–482. ISSN: 03787753. DOI: [10.1016/j.jpowsour.2014.03.046](https://doi.org/10.1016/j.jpowsour.2014.03.046). arXiv: [arXiv: 1011.1669v3](https://arxiv.org/abs/1011.1669v3). URL: <http://dx.doi.org/10.1016/j.jpowsour.2014.01.129>.
- [49] Seth Fletcher. *Bottled Lightning: Superbatteries, Electric Cars, and the New Lithium Economy*. Ed. by Macmillan. 2011.
- [50] M.-H. Kim G.-C. Chung, H.-J. Kim, S.-I. Yu, S.-H. Jun, J. Wook Choi. "Origin of graphite exfoliation an investigation of the important role of solvent cointercalation". In: *Journal of the Electrochemical Society* 147 (2000), pp. 4391–4398.
- [51] R. Gambhir, A.; Tse, L.K.C.; Tong, D.; Martinez-Botas. "Reducing China's road transport sector CO2 emissions to 2050: Technologies, costs and decomposition analysis". In: *Appl. Energy* 157 (2015), pp. 905–917.
- [52] Elena Giannakopoulou. "The Power Transition – Trends and the Future". In: *3rd HAEE Conference* (2018).
- [53] Barouch Giechaskiel et al. "European regulatory framework and particulate matter emissions of gasoline light-duty vehicles: A review". In: *Catalysts* 9.7 (2019). ISSN: 20734344. DOI: [10.3390/catal9070586](https://doi.org/10.3390/catal9070586).
- [54] Barouch Giechaskiel et al. "Measurement of automotive nonvolatile particle number emissions within the European legislative framework: A review". In: *Aerosol Science and Technology* 46.7 (2012), pp. 719–749. ISSN: 02786826. DOI: [10.1080/02786826.2012.661103](https://doi.org/10.1080/02786826.2012.661103).
- [55] Barouch Giechaskiel et al. "Particle measurement programme (PMP) light-duty inter-laboratory exercise: Comparison of different particle number measurement systems". In: *Measurement Science and Technology* 19.9 (2008). ISSN: 13616501. DOI: [10.1088/0957-0233/19/9/095401](https://doi.org/10.1088/0957-0233/19/9/095401).
- [56] Barouch Giechaskiel et al. "Review of motor vehicle particulate emissions sampling and measurement: From smoke and filter mass to particle number". In: *Journal of Aerosol Science* 67. January (2014), pp. 48–86. ISSN: 18791964. DOI: [10.1016/j.jaerosci.2013.09.003](https://doi.org/10.1016/j.jaerosci.2013.09.003).
- [57] Hongkui Gong et al. "Advances in fibre optic based geotechnical monitoring systems for underground excavations International Journal of Mining Science and Technology Advances in fibre optic based geotechnical monitoring systems for underground excavations". In: *International Journal of Mining Science and Technology* June (2018). ISSN: 2095-2686. DOI: [10.1016/j.ijmst.2018.06.007](https://doi.org/10.1016/j.ijmst.2018.06.007). URL: <https://doi.org/10.1016/j.ijmst.2018.06.007>.

- [58] Christian M. Grams et al. "Balancing Europe's wind-power output through spatial deployment informed by weather regimes". In: *Nature Climate Change* 7.8 (2017), pp. 557–562. ISSN: 17586798. DOI: [10.1038/NCLIMATE3338](https://doi.org/10.1038/NCLIMATE3338).
- [59] Thiringer T. Grunditz E.A. "Performance Analysis of Current BEVs - Based on a Comprehensive Review of Specifications". In: *IEEE Transactions on Transportation Electrification* 2.3 (2016), pp. 270–289.
- [60] P. Novák H. Buqa, A. Würsig, J. Vetter, M. Spahr, F. Krumeich. "SEI film formation on highly crystalline graphitic materials in lithium-ion batteries". In: *Journal of Power Sources* 153.2 (2006), pp. 385–390.
- [61] C. Ziegler H. Jannesari, M. Emami. "Effect of electrolyte transport properties and variations in the morphological parameters on the variation of side reaction rate across the anode electrode and the aging of lithium ion batteries". In: *Journal of Power Sources* 196.22 (2011), pp. 9654–9664.
- [62] M. Hahn et al. "A dilatometric study of lithium intercalation into powder-type graphite electrodes". In: *Electrochemical and Solid-State Letters* 11.9 (2008), pp. 151–154. ISSN: 10990062. DOI: [10.1149/1.2940573](https://doi.org/10.1149/1.2940573).
- [63] R. Hausbrand et al. "Fundamental degradation mechanisms of layered oxide Li-ion battery cathode materials: Methodology, insights and novel approaches". In: *Materials Science and Engineering B: Solid-State Materials for Advanced Technology* 192.C (2015), pp. 3–25. ISSN: 09215107. DOI: [10.1016/j.mseb.2014.11.014](https://doi.org/10.1016/j.mseb.2014.11.014). URL: <http://dx.doi.org/10.1016/j.mseb.2014.11.014>.
- [64] Troy R. Hawkins et al. "Comparative Environmental Life Cycle Assessment of Conventional and Electric Vehicles". In: *Journal of Industrial Ecology* 17.1 (2013), pp. 53–64. ISSN: 15309290. DOI: [10.1111/j.1530-9290.2012.00532.x](https://doi.org/10.1111/j.1530-9290.2012.00532.x).
- [65] Hongwen He, Rui Xiong, and Jinxin Fan. "Evaluation of lithium-ion battery equivalent circuit models for state of charge estimation by an experimental approach". In: *Energies* 4.4 (2011), pp. 582–598. ISSN: 19961073. DOI: [10.3390/en4040582](https://doi.org/10.3390/en4040582).
- [66] ICCT. "European Vehicle Market Statistics Pocketbook 2018/19". In: *International Council of Clean Transportation (ICCT) Report* (2018), p. 63. ISSN: 1600-051X. DOI: [10.1111/j.1600-051X.2009.01495.x](https://doi.org/10.1111/j.1600-051X.2009.01495.x). URL: <http://www.eafo.eu/content/european-vehicle-categories>.
- [67] IPCC. "Foreword, Preface, Dedication and In Memoriam". In: *Climate Change 2014: Mitigation of Climate Change. Contribution of Working Group III to the Fifth Assessment Report of the Intergovernmental Panel on Climate Change* (2014), p. 1454. ISSN: 17583004. DOI: [10.1017/CB09781107415416](https://doi.org/10.1017/CB09781107415416). arXiv: [arXiv:1011.1669v3](https://arxiv.org/abs/1011.1669v3).

- [68] H. Iwamoto, Y.; Noma, K.; Nakayama, O.; Yamauchi, T.; Ando. "Development of gasoline direct injection engine". In: *SAE Trans.* 106 (1997), p. 970541.
- [69] K.E. Thomas-Alyea J. Newman. *Electrochemical Systems*. Ed. by Wiley Interscience. third ed. 2004.
- [70] L. Lu J. Zhu, K. Zeng. "Cycling effects on surface morphology, nanomechanical and interfacial reliability of LiMn₂O₄ cathode in thin film lithium ion batteries". In: *Electrochimica Acta* 68 (2012), pp. 52–59.
- [71] K. Javid, R.; Nejat, A.; Hayhoe. "Selection of CO₂ mitigation strategies for road transportation in the United States using a multi-criteria approach". In: *Renew. Sustain. Energy Rev.* 38 (2014), pp. 960–972.
- [72] Ali Jokar et al. "Review of simplified Pseudo-two-Dimensional models of lithium-ion batteries". In: *Journal of Power Sources* 327. September (2016), pp. 44–55. ISSN: 03787753. DOI: [10.1016/j.jpowsour.2016.07.036](https://doi.org/10.1016/j.jpowsour.2016.07.036). URL: <http://dx.doi.org/10.1016/j.jpowsour.2016.07.036>.
- [73] T Joshi, A.; Johnson. ". Gasoline particulate filters—A review". In: *Emiss. Contr. Sci. Technol.* 4 (2018), pp. 219–239.
- [74] I. Belharouak K. Amine, J. Liu. "High-temperature storage and cycling of C-LiFePO₄/graphite Li-ion cells". In: *Electrochemistry Communications* 7.7 (2005), pp. 669–673.
- [75] J.O. Thomas K. Edstrom, T. Gustafsson. "The cathode–electrolyte interface in the Li-ion battery". In: *Electrochimica Acta* 50.2-3 (2004), pp. 397–403.
- [76] A. von Cresce K. Xu. "Interfacing electrolytes with electrodes in Li ion batteries". In: *Journal of Materials Chemistry* 21 (2011), pp. 9849–9864.
- [77] Nasrullah Khan et al. "Review of energy storage and transportation of energy". In: *Energy Storage* 1.3 (2019), pp. 1–49. ISSN: 2578-4862. DOI: [10.1002/est2.49](https://doi.org/10.1002/est2.49).
- [78] Noble Kiesel, Peter and Schmidt, Oliver and Johnson. "Wavelength monitors for optical sensing applications". In: *Photonics Spectra* 41.3 (2007), pp. 62–64.
- [79] Namdoo Kim et al. "Fuel consumption and cost potential of different plug-in hybrid vehicle architectures". In: *SAE International Journal of Alternative Powertrains* 4.1 (2015), pp. 88–99. ISSN: 21674205. DOI: [10.4271/2015-01-1160](https://doi.org/10.4271/2015-01-1160).
- [80] Karim Zaghib Kim Kinoshita. "Negative electrodes for Li-ion batteries". In: *Journal of Power Sources* 110.2 (2002), pp. 416–423. URL: [https://doi.org/10.1016/S0378-7753\(02\)00206-9](https://doi.org/10.1016/S0378-7753(02)00206-9).
- [81] Bunsen R. Kirchhoff G. R. "XXIV.—On chemical analysis by spectrum-observations". In: *Quarterly Journal of the Chemical Society of London* 13.3 (1861), p. 270. URL: [10.1039/QJ8611300270](https://doi.org/10.1039/QJ8611300270).

- [82] M. Koltypin et al. "More on the performance of LiFePO₄ electrodes-The effect of synthesis route, solution composition, aging, and temperature". In: *Journal of Power Sources* 174.2 (2007), pp. 1241–1250. ISSN: 03787753. DOI: [10.1016/j.jpowsour.2007.06.045](https://doi.org/10.1016/j.jpowsour.2007.06.045).
- [83] Natalia Lebedeva, Franco Di Persio, and Lois Boon-Brett. "Lithium ion battery value chain and related opportunities for Europe". In: *European Commission, Petten* (2016), pp. 1–75. URL: https://ec.europa.eu/jrc/sites/jrcsh/files/jrc105010{_}161214{_}li-ion{_}battery{_}value{_}chain{_}jrc105010.pdf.
- [84] Jae Hyun Lee, Hyang Mok Lee, and Soonho Ahn. "Battery dimensional changes occurring during charge/discharge cycles - Thin rectangular lithium ion and polymer cells". In: *Journal of Power Sources* 119-121 (2003), pp. 833–837. ISSN: 03787753. DOI: [10.1016/S0378-7753\(03\)00281-7](https://doi.org/10.1016/S0378-7753(03)00281-7).
- [85] Jaemoon Lee, Oanyong Nam, and B. H. Cho. "Li-ion battery SOC estimation method based on the reduced order extended Kalman filtering". In: *Journal of Power Sources* 174.1 (2007), pp. 9–15. ISSN: 03787753. DOI: [10.1016/j.jpowsour.2007.03.072](https://doi.org/10.1016/j.jpowsour.2007.03.072).
- [86] Seongjun Lee et al. "State-of-charge and capacity estimation of lithium-ion battery using a new open-circuit voltage versus state-of-charge". In: *Journal of Power Sources* 185.2 (2008), pp. 1367–1373. ISSN: 03787753. DOI: [10.1016/j.jpowsour.2008.08.103](https://doi.org/10.1016/j.jpowsour.2008.08.103).
- [87] Hong Nan Li, Dong Sheng Li, and Gang Bing Song. "Recent applications of fiber optic sensors to health monitoring in civil engineering". In: *Engineering Structures* 26.11 (2004), pp. 1647–1657. ISSN: 01410296. DOI: [10.1016/j.engstruct.2004.05.018](https://doi.org/10.1016/j.engstruct.2004.05.018).
- [88] Huaqiang Liu et al. "Thermal issues about Li-ion batteries and recent progress in battery thermal management systems: A review". In: *Energy Conversion and Management* 150.May (2017), pp. 304–330. ISSN: 01968904. DOI: [10.1016/j.enconman.2017.08.016](https://doi.org/10.1016/j.enconman.2017.08.016). URL: <http://dx.doi.org/10.1016/j.enconman.2017.08.016>.
- [89] Languang Lu et al. "A review on the key issues for lithium-ion battery management in electric vehicles". In: *Journal of Power Sources* 226 (2013), pp. 272–288. ISSN: 03787753. DOI: [10.1016/j.jpowsour.2012.10.060](https://doi.org/10.1016/j.jpowsour.2012.10.060). URL: <http://dx.doi.org/10.1016/j.jpowsour.2012.10.060>.
- [90] Luna Technologies Inc. "User's Guide - ODiSI-B". In: (2017), p. 127.
- [91] I. Villarreal M. Berceibar, M. Garmendia, I. Gandiaga, J. Crego. "State of health estimation algorithm of LiFePO₄ battery packs based on differential voltage curves for battery management system application". In: *Energy* 103 (2016), pp. 784–796. DOI: [http://dx.doi.org/10.1016/j.energy.2016.02.163](https://doi.org/10.1016/j.energy.2016.02.163).

- [92] R.J. Staniewicz M. Broussely, P. Biensan, F. Bonhomme, P. Blanchard, S. Herreyre, K. Nechev. "Main aging mechanisms in Li ion batteries". In: *J. Power Sources* 146.1-2 (2005), pp. 90–96. DOI: <http://dx.doi.org/10.1016/j.jpowsour.2005.03.172>.
- [93] R. Staniewicz M. Broussely, S. Herreyre, P. Biensan, P. Kasztejna, K. Nechev. "Aging mechanism in Li ion cells and calendar life predictions". In: *Journal of Power Sources* 97-98.13-22 (2001).
- [94] R.M. Kostecki M. Kerlau, M. Marcinek, V. Srinivasan. "Studies of local degradation phenomena in composite cathodes for lithium-ion batteries". In: *Electrochimica Acta* 52.17 (2007), pp. 5422–5429.
- [95] J. Garche M. Wohlfahrt-Mehrens, C. Vogler. "Aging mechanisms of lithium cathode materials". In: *Journal of Power Sources* 127.1-2 (2004), pp. 58–64.
- [96] Li W. Manthiram A, Song B. "A perspective on nickel-rich layered oxide cathodes for lithium-ion batteries". In: *Energy Storage Mater* 6 (2017), pp. 125–39. DOI: <https://doi.org/10.1016/j.ensm.2016.10.007>.
- [97] U. Meinig. "One hundred years of gasoline direct injection: Part 1". In: *MTZWorldw.* 77 (2016), pp. 60–66.
- [98] U. Meinig. "One hundred years of gasoline direct injection: Part 2." In: *MTZWorldw.* 77 (2016), pp. 30–37.
- [99] Metrohm. "Electrochemical Impedance Spectroscopy (EIS) Basic Principles". In: (2011), pp. 1–3.
- [100] J. B. Mizushima, K.; Jones, P. C.; Wiseman, P. J.; Goodenough. " Li_xCoO_2 ($0 < x < 1$): A new cathode material for batteries of high energy density". In: *Materials Research Bulletin* 15.6 (1980), pp. 783–789. URL: [10.1016/0025-5408\(80\)90012-4](https://doi.org/10.1016/0025-5408(80)90012-4).
- [101] S. J. Moura, N. A. Chaturvedi, and M. Krstic. "PDE estimation techniques for advanced battery management systems Part I: SOC estimation". In: *Proceedings of the American Control Conference* (2012), pp. 559–565. ISSN: 07431619. DOI: [10.1109/acc.2012.6315019](https://doi.org/10.1109/acc.2012.6315019).
- [102] Seung Taek Myung, Yashiro Hitoshi, and Yang Kook Sun. "Electrochemical behavior and passivation of current collectors in lithium-ion batteries". In: *Journal of Materials Chemistry* 21.27 (2011), pp. 9891–9911. ISSN: 09599428. DOI: [10.1039/c0jm04353b](https://doi.org/10.1039/c0jm04353b).
- [103] Micael Nascimento, Marta S. Ferreira, and João L. Pinto. "Real time thermal monitoring of lithium batteries with fiber sensors and thermocouples: A comparative study". In: *Measurement: Journal of the International Measurement Confederation* 111.March (2017), pp. 260–263. ISSN: 02632241. DOI: [10.1016/j.measurement.2017.07.049](https://doi.org/10.1016/j.measurement.2017.07.049). URL: <http://dx.doi.org/10.1016/j.measurement.2017.07.049>.

- [104] Kong Soon Ng et al. "Enhanced coulomb counting method for estimating state-of-charge and state-of-health of lithium-ion batteries". In: *Applied Energy* 86.9 (2009), pp. 1506–1511. ISSN: 03062619. DOI: [10.1016/j.apenergy.2008.11.021](https://doi.org/10.1016/j.apenergy.2008.11.021). URL: <http://dx.doi.org/10.1016/j.apenergy.2008.11.021>.
- [105] Naoki Nitta et al. "Li-ion battery materials: Present and future". In: *Materials Today* 18.5 (2015), pp. 252–264. ISSN: 18734103. DOI: [10.1016/j.mattod.2014.10.040](https://doi.org/10.1016/j.mattod.2014.10.040). arXiv: [arXiv: 1011.1669v3](https://arxiv.org/abs/1011.1669v3). URL: <http://dx.doi.org/10.1016/j.mattod.2014.10.040>.
- [106] A. Opitz et al. "Can Li-Ion batteries be the panacea for automotive applications?" In: *Renewable and Sustainable Energy Reviews* 68.October 2016 (2017), pp. 685–692. ISSN: 18790690. DOI: [10.1016/j.rser.2016.10.019](https://doi.org/10.1016/j.rser.2016.10.019). URL: <http://dx.doi.org/10.1016/j.rser.2016.10.019>.
- [107] M. Granada P. Antunes, F. Domingues, Elio Occhini, and M. Granada P. Antunes, F. Domingues. "Mechanical Properties of Optical Fibers for Cables." In: *NTG Fachber* 59.June 2014 (1977), pp. 77–82. DOI: [10.5772/26515](https://doi.org/10.5772/26515).
- [108] M. Doyle P. Arora, R.E. White. "Capacity fade mechanisms and side reactions in lithium-ion batteries". In: *Journal of the Electrochemical Society* 145.10 (1998), pp. 3647–3667.
- [109] T.P. Kumar P. Balakrishnan, R. Ramesh. "Safety Mechanisms in Lithium-Ion Batteries". In: *Journal of Power Sources* 155.2 (2006), pp. 401–414.
- [110] P. Finamore P. Liu, J. Wang, J. Hicks-Garner, E. Sherman, S. Soukiazian, M. Verbrugge, H. Tatara, J. Musser. "Ageing mechanism of LiFePO₄ batteries deduced by electrochemical and structural analyses". In: *Journal of the Electrochemical Society* 157.4 (2010), A499–A507.
- [111] Petr Novák Pallavi Verma, Pascal Maire. "A review of the features and analyses of the solid electrolyte interphase in Li-ion batteries". In: *Electrochimica Acta* 55.22 (2010), pp. 6332–6341. URL: <https://doi.org/10.1016/j.electacta.2010.05.072>.
- [112] C. Pastor-Fernández et al. "A Study of Cell-to-Cell Interactions and Degradation in Parallel Strings: Implications for the Battery Management System". In: *Journal of Power Sources* 329 (2016), pp. 574–585. ISSN: 03787753. DOI: [10.1016/j.jpowsour.2016.07.121](https://doi.org/10.1016/j.jpowsour.2016.07.121).
- [113] Carlos Pastor-Fernández et al. "A Comparison between Electrochemical Impedance Spectroscopy and Incremental Capacity-Differential Voltage as Li-ion Diagnostic Techniques to Identify and Quantify the Effects of Degradation Modes within Battery Management Systems". In: *Journal of Power Sources* 360 (2017), pp. 301–318. ISSN: 03787753. DOI: [10.1016/j.jpowsour.2017.03.042](https://doi.org/10.1016/j.jpowsour.2017.03.042).
- [114] Keirstead J. Pfenninger S. "Comparing concentrating solar and nuclear power as baseload providers using the example of South Africa". In: *Energy* 87 (2015), pp. 303–14. DOI: <https://doi.org/10.1016/j.energy.2015.04.077>.

- [115] Sabine Piller, Marion Perrin, and Andreas Jossen. "Methods for state-of-charge determination and their applications". In: *Journal of Power Sources* 96.1 (2001), pp. 113–120. ISSN: 03787753. DOI: [10.1016/S0378-7753\(01\)00560-2](https://doi.org/10.1016/S0378-7753(01)00560-2).
- [116] Walter Piock et al. "Strategies Towards Meeting Future Particulate Matter Emission Requirements in Homogeneous Gasoline Direct Injection Engines". In: *SAE International Journal of Engines* 4.1 (2011), pp. 1455–1468. ISSN: 19463936. DOI: [10.4271/2011-01-1212](https://doi.org/10.4271/2011-01-1212).
- [117] J. Poizot, P.; Laruelle, S.; Grugeon, S.; Tarascon. "Nano-sized transition-metal oxides as negative-electrode materials for lithium-ion batteries". In: *Nature* 407.6803 (2000), pp. 496–499.
- [118] Ajay Raghavan et al. "Embedded fiber-optic sensing for accurate internal monitoring of cell state in advanced battery management systems part 1: Cell embedding method and performance". In: *Journal of Power Sources* 341 (2017), pp. 466–473. ISSN: 03787753. DOI: [10.1016/j.jpowsour.2016.11.104](https://doi.org/10.1016/j.jpowsour.2016.11.104). URL: <http://dx.doi.org/10.1016/j.jpowsour.2016.11.104>.
- [119] Ajay Raghavan et al. "Embedded fiber-optic sensing for accurate internal monitoring of cell state in advanced battery management systems part 2: Internal cell signals and utility for state estimation". In: *Journal of Power Sources* 341 (2017), pp. 466–473. ISSN: 03787753. DOI: [10.1016/j.jpowsour.2016.11.104](https://doi.org/10.1016/j.jpowsour.2016.11.104). URL: <http://dx.doi.org/10.1016/j.jpowsour.2016.11.103>.
- [120] L H J Raijmakers et al. "A review on various temperature-indication methods for Li-ion batteries". In: *Applied Energy* 240.July 2018 (2019), pp. 918–945. ISSN: 0306-2619. DOI: [10.1016/j.apenergy.2019.02.078](https://doi.org/10.1016/j.apenergy.2019.02.078). URL: <https://doi.org/10.1016/j.apenergy.2019.02.078>.
- [121] V. Ramadesigan et al. "Modeling and Simulation of Lithium-Ion Batteries from a Systems Engineering Perspective". In: *Journal of the Electrochemical Society* 159.3 (2012), R31–R45. ISSN: 0013-4651. DOI: [10.1149/2.018203jes](https://doi.org/10.1149/2.018203jes). arXiv: [1602.06747](https://arxiv.org/abs/1602.06747). URL: <http://jes.ecsdl.org/cgi/doi/10.1149/2.018203jes>.
- [122] Yun Jiang Rao. "In-fibre Bragg grating sensors". In: *Measurement Science and Technology* 8.4 (1997), pp. 355–375. ISSN: 09570233. DOI: [10.1088/0957-0233/8/4/002](https://doi.org/10.1088/0957-0233/8/4/002).
- [123] REN21. *Global Status Report, Renewable 2017*. Vol. 72. October 2016. 2017, pp. 1–301. ISBN: 978-3-9818107-0-7. DOI: [10.1016/j.rser.2016.09.082](https://doi.org/10.1016/j.rser.2016.09.082).
- [124] V.R. Subramaniana R.N. Methekar, P.W.C. Northrop, K. Chen, R.D. Braatz. "Kinetic Monte Carlo simulation of surface heterogeneity in graphite anodes for lithium-ion batteries: passive layer formation". In: *Journal of the Electrochemical Society* 158.4 (2011), A363–A370.

- [125] Brett H. Robinson. "E-waste: An assessment of global production and environmental impacts". In: *Science of the Total Environment* 408.2 (2009), pp. 183–191. ISSN: 00489697. DOI: [10.1016/j.scitotenv.2009.09.044](https://doi.org/10.1016/j.scitotenv.2009.09.044). URL: <http://dx.doi.org/10.1016/j.scitotenv.2009.09.044>.
- [126] Luciano Rolando et al. "DSCC2010-". In: (2018), pp. 1–8.
- [127] H.K. Fathy S. Bashash, S.J. Moura, J.C. Forman. "Plug-in hybrid electric vehicle charge pattern optimization for energy cost and battery longevity". In: *Journal of Power Sources* 196.1 (2011), pp. 541–549.
- [128] S. Robert S. Bourlot, P. Blanchard. "Investigation of aging mechanisms of high power Li-ion cells used for hybrid electric vehicles". In: *Journal of Power Sources* 196.16 (2011), pp. 6841–6846.
- [129] O. Gross S. G. Wirasingha, M. Khan. "48-V Electrification: BeltDriven Starter Generator Systems". In: *Advanced Electric Drive Vehicles*, CRC Press (2014).
- [130] T. Jow S. Zhang, K. Xu. "Low-temperature performance of Li-ion cells with a LiBF₄-based electrolyte". In: *Journal of Solid State Electrochemistry* 7 (2003), pp. 147–151.
- [131] T. Jow S. Zhang, K. Xu. "The low temperature performance of Li-ion batteries". In: *Journal of Power Sources* 115.1 (2003), pp. 137–140.
- [132] T.R. Jow S. Zhang, M.S. Ding, K. Xu, J. Allen. "N". In: *Electrochemical and Solid State Letters* 4 (2001), pp. 206–208.
- [133] Shriram Santhanagopalan et al. "Review of models for predicting the cycling performance of lithium ion batteries". In: *Journal of Power Sources* 156.2 (2006), pp. 620–628. ISSN: 03787753. DOI: [10.1016/j.jpowsour.2005.05.070](https://doi.org/10.1016/j.jpowsour.2005.05.070).
- [134] High-speed C F G Sensors et al. "High-Definition Fiber Optic Strain Sensors". In: *LUNA datasheet* (). URL: www.lunainc.com.
- [135] R.W. Shelef, M.; McCabe. "Twenty-five years after introduction of automotive catalysts: What next?" In: *Catal. Today* 62 (2000), pp. 35–50.
- [136] Jason B. Siegel et al. "Neutron Imaging of Lithium Concentration in LFP Pouch Cell Battery". In: *Journal of The Electrochemical Society* 158.5 (2011), A523. ISSN: 00134651. DOI: [10.1149/1.3566341](https://doi.org/10.1149/1.3566341). URL: <http://jes.ecsdl.org/cgi/doi/10.1149/1.3566341>.
- [137] Ivan T. Lucas Simon Franz Lux, Julie Chevalier and Robert Kostecki. "HF Formation in LiPF₆-Based Organic Carbonate Electrolytes". In: *ECS Electrochemistry Letters* 2.12 (2013).
- [138] Graham Sinden. "Characteristics of the UK wind resource: Long-term patterns and relationship to electricity demand". In: *Energy Policy* 35.1 (2007), pp. 112–127. ISSN: 03014215. DOI: [10.1016/j.enpol.2005.10.003](https://doi.org/10.1016/j.enpol.2005.10.003).

- [139] Kandler Smith and Chao Yang Wang. "Power and thermal characterization of a lithium-ion battery pack for hybrid-electric vehicles". In: *Journal of Power Sources* 160.1 (2006), pp. 662–673. ISSN: 03787753. DOI: [10.1016/j.jpowsour.2006.01.038](https://doi.org/10.1016/j.jpowsour.2006.01.038).
- [140] Lars Wilko Sommer et al. "Monitoring of Intercalation Stages in Lithium-Ion Cells over Charge-Discharge Cycles with Fiber Optic Sensors". In: *Journal of The Electrochemical Society* 162.14 (2015), A2664–A2669. ISSN: 0013-4651. DOI: [10.1149/2.0361514jes](https://doi.org/10.1149/2.0361514jes). URL: <http://jes.ecsdl.org/lookup/doi/10.1149/2.0361514jes>.
- [141] Solith Sovema. "CELL MAKING - POUCH LI-ION CELL PILOT ASSEMBLY LINE". In: (). URL: <https://www.sovemagroup.com/wp-content/uploads/2017/10/POUCH-CELL-PILOT-ASSEMBLY-LINE-rev.01.pdf>.
- [142] Iain Staffell and Stefan Pfenninger. "The increasing impact of weather on electricity supply and demand". In: *Energy* 145 (2018), pp. 65–78. ISSN: 03605442. DOI: [10.1016/j.energy.2017.12.051](https://doi.org/10.1016/j.energy.2017.12.051). URL: <https://doi.org/10.1016/j.energy.2017.12.051>.
- [143] Darlene Steward. "Economics and Challenges of Li-Ion Battery Recycling from End-of-Life Vehicles". In: *Procedia Manufacturing* 33 (2019), pp. 272–279. ISSN: 2351-9789. DOI: [10.1016/j.promfg.2019.04.033](https://doi.org/10.1016/j.promfg.2019.04.033). URL: <https://doi.org/10.1016/j.promfg.2019.04.033>.
- [144] H. Sakaebe T. Kodama. "Present status and future prospect for national project on lithium batteries". In: *Journal of Power Sources* 81-82 (1999), pp. 144–149.
- [145] K. Tozawa T. Nagaura. "N". In: *Progress in Batteries and Solar Cells* 209.9 (1990).
- [146] "Technology Roadmap Electric and Plug-in Hybrid Electric Vehicles". In: *IEA Technical Report* ().
- [147] T.J. Truex. "Interaction of Sulfur with Automotive Catalysts and the Impact on Vehicle Emissions—A Review". In: *SAE Technical Paper: Warrendale, PA, USA* (1999).
- [148] Kotub Uddin et al. "Characterising Lithium-Ion Battery Degradation through the Identification and Tracking of Electrochemical Battery Model Parameters". In: (2016). DOI: [10.3390/batteries2020013](https://doi.org/10.3390/batteries2020013).
- [149] *U.S. Geological Survey*.
- [150] Amin Velji et al. "Investigations of the formation and oxidation of soot inside a direct injection spark ignition engine using advanced laser-techniques". In: *SAE Technical Papers* May 2016 (2010). ISSN: 26883627. DOI: [10.4271/2010-01-0352](https://doi.org/10.4271/2010-01-0352).
- [151] Prakash Venugopal and T. Vigneswaran. "State-of-charge estimation methods for Li-ion batteries in electric vehicles". In: *International Journal of Innovative Technology and Exploring Engineering* 8.7 (2019), pp. 37–46. ISSN: 22783075.

- [152] J. Vetter et al. "Ageing mechanisms in lithium-ion batteries". In: *Journal of Power Sources* 147.1-2 (2005), pp. 269–281. ISSN: 03787753. DOI: [10.1016/j.jpowsour.2005.01.006](https://doi.org/10.1016/j.jpowsour.2005.01.006).
- [153] Christian Von Hirschhausen, Johannes Herold, and Pao Yu Oei. "How a 'low carbon' innovation can fail-tales from a 'lost decade' for carbon capture, transport, and sequestration (CCTS)". In: *Economics of Energy and Environmental Policy* 1.2 (2012), pp. 115–123. ISSN: 21605890. DOI: [10.5547/2160-5890.1.2.8](https://doi.org/10.5547/2160-5890.1.2.8).
- [154] Qingsong Wang et al. "Thermal runaway caused fire and explosion of lithium ion battery". In: *Journal of Power Sources* 208 (2012), pp. 210–224. ISSN: 03787753. DOI: [10.1016/j.jpowsour.2012.02.038](https://doi.org/10.1016/j.jpowsour.2012.02.038). URL: <http://dx.doi.org/10.1016/j.jpowsour.2012.02.038>.
- [155] Daniel Werner et al. "Inhomogeneous temperature distribution affecting cyclic aging of Li-ion cells. Part ii: Analysis and correlation". In: *Batteries* 6.1 (2020). ISSN: 23130105. DOI: [10.3390/batteries6010012](https://doi.org/10.3390/batteries6010012).
- [156] Daniel Werner et al. "Inhomogeneous temperature distribution affecting the cyclic aging of Li-Ion cells. Part I: Experimental investigation". In: *Batteries* 6.1 (2020). ISSN: 23130105. DOI: [10.3390/batteries6010013](https://doi.org/10.3390/batteries6010013).
- [157] *What is HD-FOS and How Does it Deliver New Testing Insight?* URL: <https://lunainc.com/hd-fos-deliver-testing-insight/>.
- [158] Müller B. Wild M, Folini D, Henschel F, Fischer N. "Projections of long-term changes in solar radiation based on CMIP5 climate models and their influence on energy yields of photovoltaic systems". In: *Sol Energy* 116 (2015), pp. 12–24. DOI: <https://doi.org/10.1016/j.solener.2015.03.039>.
- [159] Lisa K. Willenberg et al. "High-precision monitoring of volume change of commercial lithium-ion batteries by using strain gauges". In: *Sustainability (Switzerland)* 12.2 (2020). ISSN: 20711050. DOI: [10.3390/su12020557](https://doi.org/10.3390/su12020557).
- [160] James H. Williams et al. "The technology path to deep greenhouse gas emissions cuts by 2050: The pivotal role of electricity". In: *Science* 335.6064 (2012), pp. 53–59. ISSN: 10959203. DOI: [10.1126/science.1208365](https://doi.org/10.1126/science.1208365).
- [161] Daniel Worwood et al. "A new approach to the internal thermal management of cylindrical battery cells for automotive applications". In: *Journal of Power Sources* 346 (2017), pp. 151–166. ISSN: 03787753. DOI: [10.1016/j.jpowsour.2017.02.023](https://doi.org/10.1016/j.jpowsour.2017.02.023). URL: <http://dx.doi.org/10.1016/j.jpowsour.2017.02.023>.
- [162] R. Holze Y. Wu, E. Rahm. "Carbon anode materials for lithium ion batteries". In: *Journal of Power Sources* 114.2 (2003), pp. 228–236.
- [163] Ningxin Zhang and Huaqiong Tang. "Dissecting anode swelling in commercial lithium-ion batteries". In: *Journal of Power Sources* 218 (2012), pp. 52–55. ISSN: 03787753. DOI: [10.1016/j.jpowsour.2012.06.071](https://doi.org/10.1016/j.jpowsour.2012.06.071). URL: <http://dx.doi.org/10.1016/j.jpowsour.2012.06.071>.

-
- [164] Sheng Shui Zhang. "A review on electrolyte additives for lithium-ion batteries". In: *Journal of Power Sources* 162.2 SPEC. ISS. (2006), pp. 1379–1394. ISSN: 03787753. DOI: [10.1016/j.jpowsour.2006.07.074](https://doi.org/10.1016/j.jpowsour.2006.07.074). arXiv: [arXiv:1011.1669v3](https://arxiv.org/abs/1011.1669v3).
- [165] Zhongyue Zou et al. "Evaluation of model based state of charge estimation methods for lithium-ion batteries". In: *Energies* 7.8 (2014), pp. 5065–5082. ISSN: 19961073. DOI: [10.3390/en7085065](https://doi.org/10.3390/en7085065).